

# **High Efficiency and High Sensitivity Wireless Power Transfer and Wireless Power Harvesting Systems**

by

**Xiaoyu Wang**

A dissertation submitted in partial fulfillment of the  
requirements for the degree of  
Doctor of Philosophy  
(Electrical Engineering)  
in The University of Michigan  
2016

Doctoral Committee:

Professor Amir Mortazawi, Chair  
Associate Professor Anthony Grbic  
Associate Professor Heath Hofmann  
Professor Jerome P. Lynch

© Xiaoyu Wang  
2016 All Rights Reserved

To my wife Chuan Li, and my parents

## **ACKNOWLEDGEMENTS**

There are numerous people I would like to acknowledge for their guidance, support and friendship throughout my life as a PhD student. First of all, I would like to express my deepest gratitude to my advisor, Professor Amir Mortazawi, who is not only a great mentor, but also a precious friend. The guidance and encouragement from him have been a great treasure for me, without which the work would not have been finished. I would also like to thank my committee members Professor Anthony Grbic, Professor Heath Hofmann and Professor Jerome Lynch for their time and effort serving on my dissertation committee and providing constructive suggestions and comments.

Next, I would like to thank Omar Abdelatty, with whom I have been working on the same project since summer 2015. I would also like to express my appreciation to our current and previous group members (in seniority order): Danial Ehyaie, Morteza Nick, Seyit Ahmet Sis, Victor Lee, Waleed Alomar, Seungku Lee, Fatemah (Noyan) Akbar, and Milad Zolfagharloo Koohi, for their friendship and support. I would like to thank my Radiation Laboratory friends (in alphabetical order): Seyed Mohammad Amjadi, Iverson Bell, Michael Benson, Hatim Bukhari, Xiuzhang Cai, Nikolaos Chiotellis, Jihun Choi, Sangjo Choi, Amanda Couch, Gurkan Gok, Han Guo, Jason Heebl, Shuo Huang, Huanting Huang, Amr Ibrahim, Armin Jam, Mani Kashanianfard, Omar Leon, Amanda Lietz, Yang Liu, Grant Miars, Seth Norberg, Jungsuek Oh, Amit Patel, Tai Qiao, Morteza Sheikhofta, Weitian Sheng, Shurun Tan, Peng Tian, Wei Tian, Brian Tierney, Ali Uyrus, Ning Wang,

Tianlin Wang, Jiangfeng Wu, Shang-Hua Yang, Behzad Yektakhah, and Yiting Zhang. I would like to thank the EECS staff: Jennifer, Karla, Michelle, Karen, Steven and Beth, for their patient, professional, and warmhearted help.

I would like to thank people I met in and out of classrooms for their friendship and support. There are so many names but I can only list a few: Yangchen Cao, Dongyang Tang, Lanyue Wang, Lai Wei, Nan Zheng, Avish Kosari, Fei Lv, Bianbian He, Shiqing Gao, Yiyang Jiao, Chang Liu, Peng Zhao, Jingcheng Wang, Jingxuan Liu, Xun Liu, Suyang Dong, Chen Feng, Jianfan Chen, Timothy Wong, Yingze Bao, Xiaoran Dong, and Yue Fang.

I would also like to thank the National Institute of Standard and Technology, the Department of Electrical Engineering and Computer Science, and Rackham Graduate School for the research funding and fellowships. The PhD work would not have been finished without their financial support.

Last but definitely not least, my love and gratitude to my wife Chuan Li, my parents Fufen Jin and Zhidong Wang, are beyond words and distance. Their love and support have been my largest source of energy throughout my life.

## Table of Contents

DEDICATION.....	ii
ACKNOWLEDGEMENTS.....	iii
LIST OF TABLES.....	vii
LIST OF FIGURES.....	viii
LIST OF APPENDICES.....	xiv
ABSTRACT.....	xv
Chapter 1.....	1
Introduction.....	1
1.1 An Overview of Wireless Power Transfer Technologies.....	4
1.2 An Overview of Wireless Power Harvesting Technologies.....	12
1.3 Dissertation Objectives and Contributions.....	23
1.4 Dissertation Outline.....	25
Chapter 2.....	27
Duffing Resonator Circuits for Improving the WPT Systems' Tolerance to Coupling Factor Variations.....	27
2.1 Introduction.....	27
2.2 Duffing Equation.....	28
2.3 Electrical Realization of Duffing Resonance Systems.....	31
2.4 Properties of Duffing Resonator Circuit.....	42
2.5 Design of a WPT Circuit Based on Nonlinear Resonator.....	55
2.6 Conclusion.....	61
Chapter 3.....	63
High Sensitivity Wireless Power Harvesters for Wireless Structural Health Monitoring Sensors.....	63
3.1 Introduction.....	63
3.2 System Configuration.....	65
3.3 Optimization of AM Antenna and Rectifier.....	66
3.4 Nonlinear Analysis and Modeling of Rectifier Circuits at Low RF Power Levels .....	69

3.5 Design and Optimization of the Power Management Unit .....	78
3.6 Circuit Implementation and Measurement Results .....	81
3.7 WPH System Design Based on Duffing Resonator for Improving the Tolerance to Frequency Misalignment .....	86
3.8 Conclusion .....	92
Chapter 4 .....	94
A Wide Dynamic Range Rectifier Network with Adaptive Power Distribution Method for WPT and WPH Applications .....	94
4.1 Introduction .....	94
4.2 Operation Theory and Design Methodology for a Wide Dynamic Range Rectifier Network .....	95
4.3 Adaptive Power Distribution Rectifier Network Implementation and Measurement .....	110
4.4 Conclusion .....	117
Chapter 5 .....	119
Conclusions and Future Directions .....	119
5.1 Summary .....	119
5.2 Future Work .....	120
Appendices .....	122
Appendix A .....	123
Matlab Codes For Computing the Amplitude-Frequency Response of the Duffing resonator circuit .....	123
Appendix B .....	129
Matlab Codes for Computing the Rectification Efficiency and Diode Input Impedance based on the Ritz-Galerkin Method .....	129
Bibliography .....	136

## List of Tables

Table 1.1.	Published Work on Wireless Power Harvesters .....	13
Table 1.2.	Commercially Available Wireless Power Harvesting Devices .....	14
Table 1.3.	Comparison of Energy Sources and Their Properties .....	15
Table 2.1.	Component specifications for the WPH system design .....	43
Table 2.2.	Specifications of SMV1249 varactor diode.....	53
Table 2.3.	Component specifications for the WPT system design.....	57
Table 3.1.	Diode Parameters for HSMS2852.....	75
Table 3.2.	Component specifications for the WPH system design .....	87
Table 3.3.	Comparison of RF Energy Harvesters.....	92
Table 4.1.	Specifications for the adaptive power distribution rectifier array.....	110
Table 4.2.	Comparison of Wide Dynamic Range Rectifier Circuits .....	118

## List of Figures

Figure 1.1. Summary of different wireless power transfer technologies .....	6
Figure 1.2. Block diagram of a typical two-coil SCMR WPT system.....	7
Figure 1.3. Equivalent circuit of a WPT system with multiple resonant coils. ....	7
Figure 1.4. Transfer efficiency vs operation frequency and coupling factor; showing the frequency splitting phenomenon. ....	8
Figure 1.5. Typical rectification efficiency vs. input power of a P/N diode .....	10
Figure 1.6. Block diagram of a typical WPH system.....	17
Figure 1.7. An example of voltage multiplier circuit.....	19
Figure 1.8. An example of switched capacitor voltage converter circuit.....	20
Figure 1.9. (a) Buck converter circuit; and (b) boost converter circuit.....	21
Figure 2.1. The amplitude-frequency response of a Duffing resonator circuit. Orange and blue arrows show the hysteresis loop and jump phenomenon. ....	30
Figure 2.2. The amplitude-frequency response of Duffing resonator circuits with different nonlinearity coefficients ( $\epsilon$ ).....	30
Figure 2.3. Basic diagram of a Duffing resonant circuit using a nonlinear capacitor ....	32
Figure 2.4. Symmetric C-V curves for nonlinear capacitors: (a) bell-shaped curve and (b) well-shaped curve. ....	32
Figure 2.5. Negative feedback process in a Duffing resonator circuit, showing the feedback term provided by the nonlinear capacitor. ....	35
Figure 2.6. (a) Anti-series connected varactor diode pair, (b) an example of ferroelectric barium strontium titanate (BST) varactor, and (c) an example of ceramic capacitor: C2225C102KHRAC SMD.....	36
Figure 2.7. An example of BST varactors: measured dielectric tunability curve and loss tangent for BST varactors with different sizes [110] .....	40

Figure 2.8. An example of nonlinear ceramic capacitors: tunability curve of a 3.0 kV, 1.0 nF multilayer ceramic commercial capacitor.....41

Figure 2.9. The frequency response of the Duffing resonator circuit, in comparison with a LC circuit with the same Q. For the Duffing resonator, the solid blue curve shows the high-amplitude equilibrium points at different frequencies, while the solid red curve shows the low-amplitude equilibrium points. The dashed red curve shows the amplitude response of the linear resonator used for comparison.....44

Figure 2.10. The frequency response of the Duffing resonator circuit for different excitation amplitudes (Vs) from 0.3 V to 0.6 V. The solid blue curve shows the high-amplitude equilibrium points at different frequencies, while the solid red curve shows all the low-amplitude equilibrium points.....45

Figure 2.11. The frequency response of the Duffing resonator circuit for different Q values from 125 to 350. The solid blue curve shows the high-amplitude equilibrium points at different frequencies, while the solid red curve shows the low-amplitude equilibrium points. ....47

Figure 2.12. The frequency response of the Duffing resonator circuit for different inductance values ranging from 700  $\mu$ H to 1000  $\mu$ H. The solid blue curve shows the high-amplitude equilibrium points, while the solid red curve shows the low-amplitude equilibrium points.....48

Figure 2.13. The frequency responses of the BST-based Duffing resonator circuits with different  $C_0$  (zero-bias capacitance) values. The solid blue curve shows the high-amplitude equilibrium points, while the solid red curve shows the low-amplitude equilibrium points. ....50

Figure 2.14. The frequency responses of the BST-based Duffing resonator circuits with different  $V_2$  values. The solid blue curve shows the high-amplitude equilibrium points, while the solid red curve shows the low-amplitude equilibrium points. ....51

Figure 2.15. Diagram of the 1 MHz WPH system employing a Duffing resonator .....52

Figure 2.16. Measured voltage amplitude as functions of excitation frequencies at different available power levels from the source. ....	54
Figure 2.17. Measured voltage amplitude as functions of excitation frequencies with different loaded Q values. ....	55
Figure 2.18. Diagram of the two-coil WPT system employing a Duffing resonator .....	57
Figure 2.19. Simulated efficiency versus normalized distance (d/D) for the WPT circuit with nonlinear resonator in the secondary coil, in comparison with the efficiency for a WPT circuit with linear resonator of the same Q value. ....	58
Figure 2.20. Photograph of the two-coil WPT system employing a Duffing resonator ...	60
Figure 2.21. Measured transfer efficiencies (defined as $\eta = P_{out}/P_{av}$ ) of both the nonlinear WPT circuit and the conventional linear WPT circuit as a function of normalized coupling distance to the coil diameter (d/D). ....	60
Figure 3.1. Block diagram of the medium wave wireless power harvester .....	66
Figure 3.2. Measured Q (dots) of ferrite antenna versus the number of windings .....	68
Figure 3.3. Configuration of the antenna and rectifier circuit .....	69
Figure 3.4. (a) Series and (b) shunt connected single diode rectifier .....	71
Figure 3.5. (a) Full nonlinear model and (b) de-embedded model for a PIN junction diode .....	71
Figure 3.6. Shunt-connected diode rectifier with HSMS 2852 Schottky diode for a 900 MHz wireless power harvester .....	75
Figure 3.7. Rectification efficiency versus input power at 900 MHz for $RL = 3 k\Omega$ . Results generated from the proposed analysis, the conventional piecewise linear analysis, ADS Harmonic simulation, and experiment were plotted against various input power. ..	76
Figure 3.8. Optimum impedance matching condition versus input power at 900 MHz for $RL = 2 k\Omega, 10 k\Omega$ and $50 k\Omega$ . Solid curves show the calculated values, and dashed curves show the values optimized with Agilent ADS software. Smith Chart is normalized to $Z_0 = 1 k\Omega$ for the convenience of plotting. ....	77

Figure 3.9. Topology of the power management unit, with dashed box showing the boost converter. ....	79
Figure 3.10. Measured efficiency of the boost converter versus input voltage.....	79
Figure 3.11. Schematic of the Schmitt Trigger Circuit, dashed box shows the voltage detector, the resistors outside the box provide positive feedback. ....	81
Figure 3.12. Photograph of the medium wave energy harvesting circuit. ....	82
Figure 3.13. Waveform of $V_C$ and $V_{out}$ of the boost converter and the control signal given by the Schmitt trigger circuit. The reference voltages of the Schmitt trigger circuit, $V_{high}$ and $V_{low}$ , were set to 0.2 V and 0.08 V respectively. ....	83
Figure 3.14. The overall RF-DC efficiency vs. RF input power levels of the WPH receiver .....	84
Figure 3.15. The harvester being tested on a highway bridge in Detroit, Michigan .....	85
Figure 3.16. Received power versus distance to a local AM broadcasting station (WXYZT) .....	85
Figure 3.17. Circuit of the 1 MHz WPH receiver employing a Duffing resonator .....	87
Figure 3.18. Photograph of the 1 MHz WPH circuit (excluding boost converter and control circuit) employing a Duffing resonator .....	87
Figure 3.19. Measurement Setup .....	88
Figure 3.20. Comparison between the voltage amplitude response of a Duffing resonator based EM harvester and a linear resonator based EM harvester. (a) The simulation and measurement results for the Duffing resonator in comparison with the linear resonator without a load, and (b) the simulation and measurement results for the Duffing resonator in comparison with the linear resonator, when both circuits are connected to matched loads ( $R_L = R_S = 33 \Omega$ ).....	89
Figure 3.21. Measured output power of a Duffing resonator in comparison with a linear LC resonator. Both circuits are optimally loaded (equivalent load resistance matches to $R_S$ ). Power available from the source is 0.7 $\mu$ W for both cases. ....	91

Figure 4.1. Typical rectification efficiency vs. input power of a P/N diode .....	96
Figure 4.2. Conduction angle of diode and conductance vs. input power level (parasitic reactive components are cancelled with impedance transformation network) .....	97
Figure 4.3. A basic block diagram intended to describe the operating principles of the adaptive power distribution rectifier array. The block diagram uses two individual rectifiers. ....	98
Figure 4.4. The ideal conductance variation curves of Rectifier 1, Rectifier 2, and their combination.....	99
Figure 4.5. Ideal input power to Rectifier 1, Rectifier 2, and their combination, as functions of available power level.....	100
Figure 4.6. The comparison of rectification efficiencies: one single rectifiers; simple shunt of two rectifiers; and adaptive power distribution rectifier array circuit described in this dissertation.....	102
Figure 4.7. An example realization of the proposed adaptive power distribution rectifier circuit scheme: (a) lumped-element based design; (b) the rearranged form of the circuit and the input conductance versus power for each branch.....	104
Figure 4.8. An example realization of the multi-way power distribution rectifier circuit scheme (based on lumped-elements).....	105
Figure 4.9. Multi-device (shown with the example of three-way rectifier array) power split efficiency, in comparison with a two-device rectifier array.....	105
Figure 4.10. Equivalent circuits for explanation of the impedance modulation theory.....	106
Figure 4.11. Operation principle of the adaptive power distribution rectifier array: source impedance modulation perspective. ....	107
Figure 4.12. Adaptive power distribution rectifier array operation principles: (a) device voltages; and (b) device currents at different available power levels. Pictures show the case of even power splitting with ideal devices.....	109

Figure 4.13. Adaptive power distribution rectifier array operation principles: output power at different available power levels. Pictures show the case of even power splitting with ideal devices. ....	109
Figure 4.14. Circuit diagram of the adaptive power distribution rectifier array. ....	110
Figure 4.15. Simulated RF power distributed to each rectifier device as functions of available power level from the source. Red solid curve shows the RF power distributed to Rectifier 1, while the blue dashed curve shows the RF power distributed to Rectifier 2. ....	112
Figure 4.16. Simulated return loss for the adaptive power distribution circuit, in comparison with the return loss for a single diode rectifier circuit designed with the same device and optimized at the same frequency. Black solid curve shows the return loss of the adaptive power distribution circuit, while the red dashed curve shows the return loss of the single diode rectifier circuit. ....	113
Figure 4.17. Simulated overall efficiency for the adaptive power distribution circuit, in comparison with the return loss for a single diode rectifier circuit designed with the same device and optimized at the same frequency. Black solid curve shows the overall efficiency of the adaptive power distribution circuit, while the red dashed curve shows the overall efficiency of the single diode rectifier circuit. ....	114
Figure 4.18. A photograph of the two-way wide dynamic range rectifier array. ....	115
Figure 4.19. Measurement setup. ....	115
Figure 4.20. The measured reflection coefficient for the wide dynamic range rectifier array, in comparison to a single diode rectifier circuit optimized at the same frequency. ....	116
Figure 4.21. The measured overall efficiency (considering both the rectification loss and impedance mismatch reflection) for the wide dynamic range rectifier array, in comparison to a single diode rectifier circuit optimized for the highest efficiency. ....	117

## List of Appendices

Appendix A.....	123
Matlab Codes For Computing the Amplitude-Frequency Response of the Duffing resonator circuit .....	123
Appendix B .....	129
Matlab Codes for Computing the Rectification Efficiency and Diode Input Impedance based on the Ritz-Galerkin Method.....	129

## **Abstract**

In this dissertation, several approaches to improve the efficiency and sensitivity of wireless power transfer and wireless power harvesting systems, and to enhance their performance in fluctuant and unpredictable circumstances are described.

Firstly, a nonlinear resonance circuit described by second-order differential equation with cubic-order nonlinearities (the Duffing equation) is developed. The Duffing nonlinear resonance circuit has significantly wider bandwidth as compared to conventional linear resonators, while achieving a similar level of amplitude. The Duffing resonator is successfully applied to the design of WPT systems to improve their tolerance to coupling factor variations stemming from changes of transmission distance and alignment of coupled coils.

Subsequently, a high sensitivity wireless power harvester which collects RF energy from AM broadcast stations for powering the wireless sensors in structural health monitoring systems is introduced. The harvester demonstrates the capability of providing net RF power within 6 miles away from a local 50 kW AM station. The aforementioned Duffing resonator is also used in the design of WPH systems to improve their tolerance to frequency misalignment resulting from component aging, coupling to surrounding objects or variations of environmental conditions (temperature, humidity, etc.).

At last, a rectifier array circuit with an adaptive power distribution method for wide dynamic range operation is developed. Adaptive power distribution is achieved through impedance transformation of the rectifiers' nonlinear impedance with a passive network. The rectifier array achieves high RF-to-DC efficiency within a wide range of input power levels, and is useful in both WPT and WPH applications where levels of the RF power collected by the receiver are subject to unpredictable fluctuations.

# Chapter 1

## Introduction

Wireless power transfer (WPT) and wireless power harvesting (WPH) technologies are two closely related fields that have recently experienced a rapid growth [1]-[3]. WPT technology achieves wireless transfer of the electrical power through time-varying electromagnetic (EM) fields [1]. It is a very promising solution to power various electrical devices in applications where power delivery through wires or batteries is inconvenient, hazardous, expensive, or impractical [1].

WPT technologies have a wide range of commercial and defense related applications. In the commercial market, they receive wide interest since they can simplify people's daily life by eliminating the need for power cables and chargers. WPT technologies are designed for transmitting different power levels ranging from  $\mu$ Ws to MWs. Some common applications include RFID tags ( $\mu$ W to mW), bio-implants (mW to W), wirelessly charging systems for consumer electronic devices (Watts) and electrical vehicles (kW or MWs) [4]-[10]. WPT technology is expected to become the mainstream method for powering consumer electronics [11] [12]. Within the last few years, standard-setting organizations such as Wireless Power Consortium (WPC) [13] and Alliance for Wireless Power (A4WP) [14] were formed, introducing various standards, such as Qi published in 2010 [15]. Under

these standards, many commercial products have been developed for charging consumer electronics, for instance, the wireless charging pads for cellphones [16]. WPT technologies for wirelessly powering the home electrical equipment such as lights and TVs are also under development [17]. Moreover, high power wireless charging systems for electric vehicles (EVs) using the WPT technology are being developed by major automobile manufacturers (such as Nissan, Toyota, BMW and Mercedes) and independent companies (such as Qualcomm and WiTricity) [18]. There are also other systems under development that aim at powering electric vehicles on the road by using WPT coils embedded along the roads or railway tracks [19]. Overall speaking, the market for WPT is vast and rapidly growing. The WPT market is expected to reach a total of \$15.2 billion in 2020 [20].

WPT technology can also benefit a wide range of defense related applications. A promising application of WPT technology is to reduce the weight that soldiers need to carry [21]. Soldiers nowadays rely on more and more electronics devices powered through bulky cables. For instance, there are usually cables connecting the soldier's helmet (where most sense and assist devices might reside) and vest (where centralized power sources might reside). WPT technology can eliminate the need for power cables. Also, WPT technology allows the soldier's rechargeable batteries in his vest pack to be charged whenever the soldier enters a "recharging zone", such as a vehicle, certain areas within a base, etc. [22]. Another promising application of WPT technology lies in the operation and maintenance of equipment. For example, military robots or unmanned ground/aerial vehicles equipped with WPT technology could be charged during ground transportation or storage [23]. Furthermore, the batteries in missiles can be trickle charged by WPT technology to ensure

that the missiles are in good operational conditions over tens of years' of unattended storage.

WPH, on the other hand, is the process by which the radiated electromagnetic (EM) energy is harnessed from ambient EM sources for powering small electronic devices [24]. Several examples of the ambient EM energy sources include radio stations (535 to 1700 kHz for AM, and 87.5 to 108 MHz for FM), TV broadcast stations (174-216 MHz VHF, and 470-806 MHz UHF), Wi-Fi networks (2.4/5 GHz), cellphone towers (850/900/1700/1900/2100 MHz), etc. WPH technology has a wide range of applications in many scientific and engineering related fields, such as structural health monitoring (SHM) systems [25], in-field environment data collection [26], battlefield information gathering [26], and Internet of Things (IoT) [27]. These applications typically include powering of autonomous devices which have a long expected service life, and cannot be powered by batteries or cables due to one or more of the following reasons:

- Inaccessibility (e.g. under concrete or building materials, or in hostile surroundings);
- Sheer numbers (e.g. millions of wireless tags in an IoT system);
- Dispersed spatial distribution (e.g. sensors for collecting environmental information).

WPH technology enables battery-less operation of autonomous devices and extends their operating lifetime dramatically, and therefore reduces the system's deployment cost [28]. As an example, a SHM system typically involves thousands of sensors which are expected to operate for decades. The sensors in a SHM system are sometimes located in hard-to-reach positions (such as underneath concrete). If batteries were to be used to power these sensors, the periodic battery replacement would lead to millions of dollars of maintenance cost (mostly due to labor), which accounts for as high as 80% of the total

deployment costs [29]. The maintenance cost can be effectively reduced with WPH technology which eliminates the need for battery replacements. As another example, about 600,000 artificial cardiac pacemakers are implanted in the U.S. each year. Currently most of them are powered by batteries with lifetime expectations of approximately 10 years [30], significantly shorter than their service time (usually decades). Thus, costly and risky surgeries are needed periodically. The need for battery replacement surgeries can be potentially eliminated by WPH-based pacemakers, which are powered by the EM energy penetrating into the human body.

## **1.1 An Overview of Wireless Power Transfer Technologies**

### **1.1.1 History and Existing work**

The early work in wireless power transfer dates back to the 1890s and 1990s, when Nikola Tesla conducted pioneering WPT experiments based on microwave technology [31]-[33]. He first realized long distance wireless power transfer over 48 kilometers in 1896, and then powered up a bank of 200 light bulbs as well as an electric motor with wireless power at a distance of 26 miles in 1899. He also invented the “Tesla coil”, which produces high-frequency, high-voltage alternating currents, and constructed the Wardencllyffe Tower (“Tesla Tower”) as an early wireless transmission station through the ionosphere.

After Tesla’s work, the area of WPT technologies was not very active until William C. Brown’s work during the 1960s-1980s [34]. Brown successfully converted microwave energy to DC energy with a rectenna (antenna and rectifier), and demonstrated a helicopter completely powered wirelessly through a 2.45 GHz microwave beam in 1964 [35]. He

continued to work on directional long distance WPT through microwave beams. In 1975, he beamed 34 kW microwave power to a rectenna located one mile away, achieving a transmission efficiency of 82.5% [36].

The technology for near-field wireless power transfer starts to emerge in the 1990s along with the fast spread of personal electronic devices [37]. In 2007, the strongly coupled magnetic resonance (SCMR) method was devised and achieved over 40% transmission efficiency in transferring 60 Watts power to 2-meter distance [38]. Intel helped to improve the design, boosting the efficiency to above 75% in 2008 [39]. The competition for better efficiency, longer transfer distance and higher power capacity has since continued. Efficiencies higher than 95% have been reported at power levels of hundreds of Watts [40]. WPT systems capable of transferring power levels as high as 200 kW for charging electric buses have been demonstrated [41]. Wireless power transfer to multiple receivers from a single transmitter was successfully demonstrated recently [42]. Furthermore, wireless power transfer using multiple intermediate resonant coil repeaters has also been developed [43].

Today's wireless power transfer technology can be categorized as radiative RF-based WPT and non-radiative coupling-based WPT [44]. The radiative RF-based WPT technology relies on high directivity microwave beams to transfer electric power, typically employing high gain antennas. This technology can achieve high efficiencies, long transmission distances and high power levels. One of its typical applications is the solar power satellite (SPS), which aims at collecting solar energy in geo-stationary earth orbit and transferring the power to earth through a microwave beam [45].

Non-radiative coupling-based WPT technology, on the other hand, relies on either electric field coupling or magnetic field coupling to achieve wireless power transfer. Magnetic field coupled WPT systems can be further classified into inductive power transfer (IPT) and strongly coupled magnetic resonance (SCMR), where the latter has become the mainstream wireless charging method for the consumer electronics market due to its mid-range, non-radiative and high-efficiency characteristics. The categories of wireless power transfer technologies are summarized in Figure 1.1.

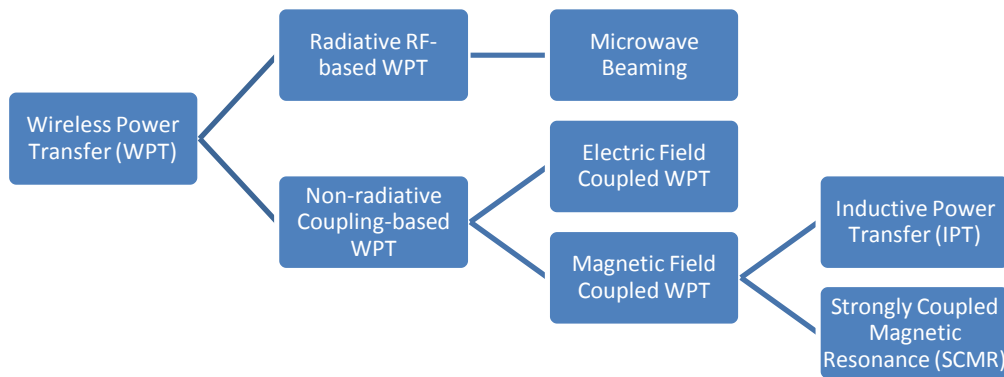


Figure 1.1. Summary of different wireless power transfer technologies

### 1.1.2 Architecture and Operation of SCMR WPT Systems

The typical block diagram for a basic two-coil SCMR WPT system is shown in Figure 1.2 [44]. In such a system, the power source drives a primary coil. A secondary coil, which is magnetically coupled to the primary coil, captures the RF power transmitted through time-varying magnetic field. The RF power is then converted to DC with a rectifier. Impedance transformation networks in both the transmitter and the receiver provide impedance matching condition to minimize power reflection. In the receiver, a power

management unit regulates the output DC power and provides the required voltage level depending on the need of specific applications.

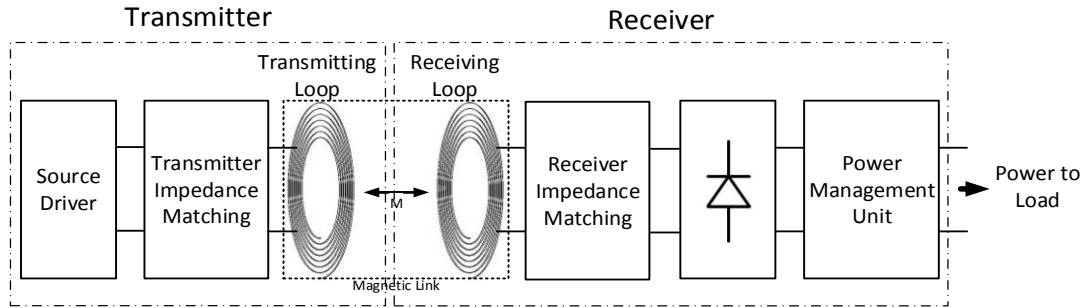


Figure 1.2. Block diagram of a typical two-coil SCMR WPT system

In order to achieve a long transfer range and high transfer efficiency, high-Q resonant coils are usually used in both the transmitter and the receiver. Multiple ( $>2$ ) resonant coils, as shown in Figure 1.3, can be also utilized to optimize the transfer characteristics of the system.

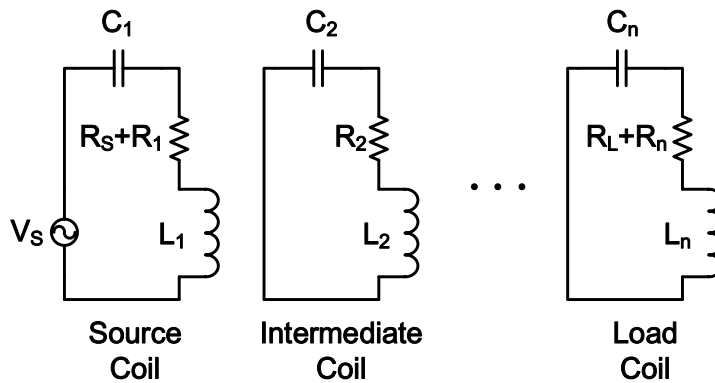


Figure 1.3. Equivalent circuit of a WPT system with multiple resonant coils.

In a SCMR system, the transferred power is a function of frequency and coupling factor between the transmitter and receiver coils, as shown in Figure 1.4 [46], [47]. Here the

transfer efficiency is defined as the ratio between the output power and the available power from the source. The highest performance is achieved when the resonant coils are critically coupled to each other, corresponding to a specific coupling factor and operation frequency. At couplings factors below the critical coupling factor (i.e. under-coupled regions, for example when the distance between the two coils is too far), the optimum frequency of operation remains the same, yet the transfer efficiency decays exponentially. At coupling factors above the critical coupling factor (i.e. over-coupled regions, e.g. at very close transfer distance), a well-known phenomenon named frequency splitting occurs ([44], [47]). The maximum power transfer efficiency is achieved at two different frequencies other than the original operation frequency. In practice, a WPT system is usually designed to operate at the critical-coupled condition to achieve the highest power transfer efficiency.

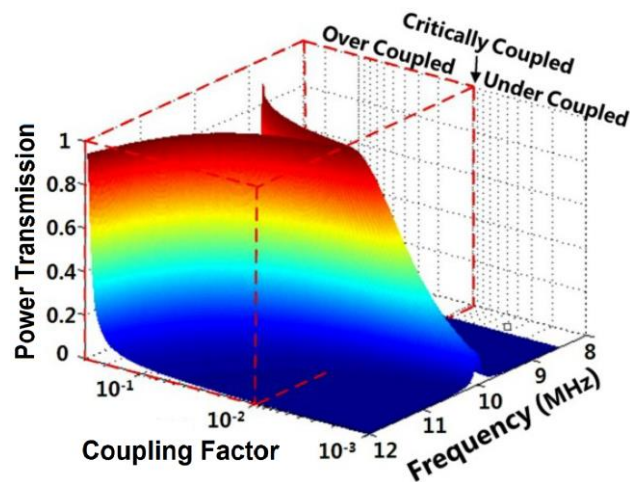


Figure 1.4. Transfer efficiency vs operation frequency and coupling factor; showing the frequency splitting phenomenon.

### 1.1.3 Challenges in the Design of SCMR WPT systems

Although SCMR has become the mainstream method for wireless power transfer due to its high efficiency, SCMR-based systems are prone to efficiency degradation as the operating condition changes (for example, when the coupling factor between the two coils varies or when the component values drift). This phenomenon can be attributed to the high quality factor (Q) resonant coils that are used in both the transmitter and receiver in such systems [48]. In conventional resonators, the bandwidth is inversely proportional to Q ( $Bandwidth = f/Q$ , where  $f$  is the natural resonant frequency); and therefore, the high Q resonant coils have very narrow bandwidths. As a result, WPT systems require meticulous tuning to align the resonant frequency of the coupled coils to the natural resonant frequency, which is usually difficult because the resonant frequency of the coupled coils is influenced by temperature, humidity, coupling to nearby objects, tolerance of component values, etc. [49], [50]. Another issue with the design of WPT systems is the difficulty in maintaining a constant coupling factor between the two coils, since the position of the transmitter and the receiver are not usually able to be controlled accurately. For example, in wireless charging systems for electric vehicles, the coupling factor is influenced by the parking position, vehicle type, vehicle size, etc. Furthermore, in cases where electric vehicles are expected to be charged while driving, the coupling factor is constantly changing as a function of the vehicle's position.

Limited dynamic range of rectifiers is another major concern in designing WPT systems. Rectifiers are an essential block in WPT systems to convert the input RF energy to DC efficiently for powering various electrical devices [51]-[52]. A major performance measure for rectifiers is the RF-DC efficiency, calculated as the output DC power over the available

RF power, which is influenced by both the device rectification efficiency ( $\eta_{rect}$ ), and the rectifier impedance matching, as (1.1):

$$\eta_{RF-DC} \triangleq \frac{P_{dc}}{P_{av}} = (1 - |\Gamma|^2)\eta_{rect} \quad (1.1)$$

where  $\Gamma$  is the reflection coefficient.

Since the induced RF power is subject to fluctuation in practical applications, it is important for the rectifiers to maintain high efficiency over a wide variation of input power level, such that the near-optimum  $\eta_{RF-DC}$  can be achieved as the power level fluctuates [53]-[56]. However, since the rectification efficiency and input impedance of RF rectifiers vary with input power, both  $\eta_{rect}$  and  $\Gamma$  in (1.1) are functions of the input power level. For example, Figure 1.5 shows the typical rectification efficiency of a diode rectifier versus input power [57]. The rectification efficiency increases with the input power level until the saturation point where the diode breakdown effects start to degrade the performance. Therefore, in conventional rectifier designs,  $\eta_{RF-DC}$  is usually optimized at a specific power level, and would experience significant degradation as the power level changes [57].

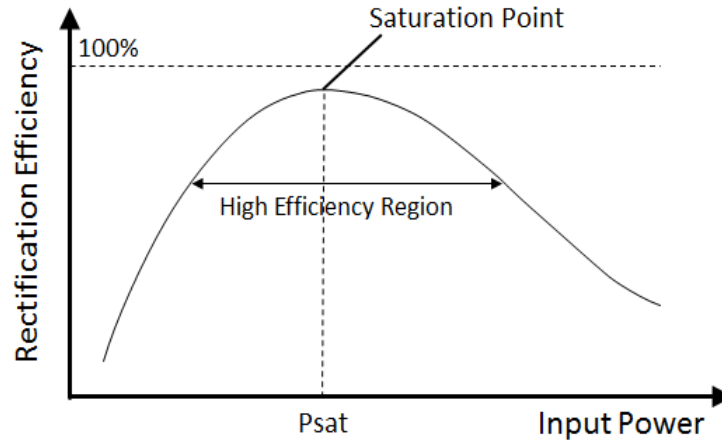


Figure 1.5. Typical rectification efficiency vs. input power of a P/N diode

While several methods have been proposed to address the above challenges in designing WPT systems, all of the proposed approaches have certain shortcomings. For example, to compensate for the impact of the coupling factor variation in WPT systems, tunable impedance matching circuits are used to track the WPT systems' optimum operation frequency in the over-coupled region (impedance-tuning method [58]). Circuits that vary the transmit frequency to track the optimum operating point in WPT systems have also been investigated (frequency-tuning method) [59]-[61]. However, these approaches generally employ complex active control circuits, increasing the systems' cost and size and thereby impeding their commercialization. Furthermore, varying the transmit frequency for WPT systems is often impractical because of frequency allocation regulated by FCC [62]. At the same time, different approaches are studied in order to maintain the rectifiers' conversion efficiency over a wide range of input power levels. For example, the Maximum Power Point Tracking (MPPT) method [63]-[66] adjusts the circuit parameters through an active sensing-and-decision-making circuitry to maintain the optimum operation condition of the rectifiers. However, the control circuitry adds to the complexity and cost, and requires power for its operation. Alternatively, circuits utilizing multiple rectifying devices connected either in series or in parallel [67]-[69] have been investigated to extend the dynamic range of rectifiers. With such an approach, RF switches are used to alter the RF path according to the input power level. However, the performance is usually degraded by the non-idealities of the switching devices, such as their conduction losses and threshold voltages. Furthermore, such an approach is effective in improving the rectification efficiency  $\eta_{rect}$ , but is not so effective in minimizing the reflection coefficient  $\Gamma$  over different power levels. Another approach, proposed in [53] and [54], utilizes a resistive

compression network which reduces RF power reflection as the rectifiers' input impedance changes; however, such an approach does not address the rectification efficiency  $\eta_{rect}$ , and is based on a symmetric circuit topology including an even number of branches where identical rectifying devices and loads have to be used for each branch within the network.

## **1.2 An Overview of Wireless Power Harvesting Technologies**

### **1.2.1 History and Existing Work**

Wireless power harvesting systems have gained increased attention since the late 1990s, due to the increased number of RF transmitting devices and the ubiquitousness of electromagnetic energy sources. Hagerty *et al.* [70] developed a broadband rectenna array that harvested energy over a wide frequency band of 2-18 GHz. Intel Research Seattle demonstrated an RF energy scavenger which works from 4.1 km away of a 960 kW TV station [71]. Dolgov *et al.* proposed a microcontroller-based system that can operate with input power ranging from 10  $\mu$ W to 1 mW for scavenging energy from ambient cellular towers [72]. Parks *et al.* designed a sensor node that can operate at a distance of 10.4 km from a 1 MW digital TV transmitting tower working at 500 MHz [73]. Vyas *et al.* succeeded in collecting RF power at a distance of 6.3 km away from a 48 kW TV tower in Tokyo [74]. Some of the published work in the area of wireless power harvesting is listed in Table 1.1.

Table 1.1. Published Work on Wireless Power Harvesters

<b>Project &amp; Year of Publication</b>	<b>Energy Source</b>	<b>Sensitivity and Scavenging Distance</b>	<b>Load</b>	<b>Process</b>
Hargerty [70], 2004	2-18 GHz; single-tone and multi-tone	N/A; 50 m	N/A	PCB
Intel Research Seattle [71], 2009	960 kW TV station @ 674-680 MHz	N/A; 4.1 km	Temp Sensor	PCB
Dolgov [72], 2010	Cellular tower; 1.96 GHz	-15.2 dBm; 50 m	Battery	PCB
Parkers [73], 2013	1 MW TV station @ 539 MHz; Cellular tower @ 738 MHz	-18 dBm; 10.4 km from the TV station or 200 m from the cellular tower	Capacitor	PCB
Vyas [74], 2013	48 kW Digital TV station @ 512-566 MHz	-14.6 dBm single tone or -37 dBm multi-tone over 2 TV channels; 6.3 km	16-bit PIC MCU	PCB

Commercial products for wireless power harvesting applications have also entered the market, including power management ICs, voltage converters, low leakage energy storage devices, etc. They generally utilize integrated circuit (IC) technology for ultra-low power consumption and leakage, and are optimized for low-power operation. Energy harvesting solution kits that can capture energy from various types of sources have also been developed. Table 1.2 shows several examples of commercially available WPH devices.

Table 1.2. Commercially Available Wireless Power Harvesting Devices

Name	Manufacturer	Type	Key Specifications
BQ25504 [75]	Texas Instrument	Ultra-low power boost converter with battery management	$V_{in} \geq 80 \text{ mV}$ Quiescent current $I_Q \leq 330 \text{ nA}$ Programmable MPPT
MAX17710 [76]	Maxim	Energy harvesting charger and protector	Quiescent current $I_Q \leq 625 \text{ nA}$ $P_{out}$ ranging from $1 \mu\text{W}$ to $100 \text{ mW}$
PCC110/PCC210 [77]	Powercast	RF-to-DC converter and boost converter	Up to 75% peak efficiency; Operating range $-17 \text{ dBm} \sim 20 \text{ dBm}$
EFM32GG Starter Kit [78]	Silicon Laboratories	Energy harvesting solution kit	Captures four different energy sources: solar, electromagnetic, piezo-electric, and thermal.

### 1.2.2 Comparison of Existing Energy Harvesting Technologies

There are many types of energy sources in the environment that can be used for energy harvesting. Some typical examples include solar energy, thermal energy, vibration/kinetic energy, RF energy, etc. Energy harvesting technologies from the commonly used energy sources are compared in Table 1.3 [79] [80].

Table 1.3. Comparison of Energy Sources and Their Properties

<b>Energy Source</b>	<b>Power Density</b>	<b>Output</b>	<b>Availability</b>	<b>Pros</b>	<b>Cons</b>
<b>Ambient Light</b>					
<i>Indoor</i>	0.1 mW/cm <sup>2</sup>	10 μW/cm <sup>2</sup>	Daytime (4-8 hours)	High power density; Well developed technology	Non-continuous; Weather limited; Orientation issue
<i>Outdoor</i>	100 mW/cm <sup>2</sup>	10 mW/cm <sup>2</sup>			
<b>Vibration /Kinetic</b>					
<i>Human</i>	0.5 m/s <sup>2</sup> @ 1 Hz 1 m/s <sup>2</sup> @ 50 Hz	4 μW/cm <sup>2</sup>	Activity dependent	Light weight; Small volume	Highly variable output; Discontinuous availability
<i>Industrial</i>	1 m/s <sup>2</sup> @ 5 Hz 10 m/s <sup>2</sup> @ 1 kHz	100 μW/cm <sup>2</sup>			
<b>Thermal</b>					
<i>Human</i>	20 mW/cm <sup>2</sup>	30 μW/cm <sup>2</sup>	Continuous	Always available	Need large area; Low power; Rigid & brittle
<i>Industrial</i>	100 mW/cm <sup>2</sup>	1~10 mW/cm <sup>2</sup>			
<b>Ambient RF Energy</b>	0.0002 ~ 1μW/cm <sup>2</sup>	0.0001~0.5 μW/cm <sup>2</sup>	Continuous	Always available	Distance dependent; Large antenna size

As summarized in Table 1.3, all the existing technologies have advantages and limitations. The photovoltaic technology has been well developed over the last 60 years [81]. The power density provided by solar panels is very high. However, the availability of solar energy is dependent on both time of day and weather conditions [79]. Solar panels also require correct orientations to collect sufficient amount of power. Vibration/kinetic energy harvesters typically rely on the piezoelectric effect to convert kinetic energy to electrical energy. Piezoelectric generators are usually compact and low-weight as

compared to generators of other energy harvesting technologies [79]. However, the level of output power is highly dependent on the activities in the surrounding area, which is often unstable and unreliable. Thermal energy can be collected by taking advantage of the thermoelectric effect. Thermoelectric devices can provide energy continuously as long as there is a temperature gradient, but the power density in terms of volume is generally low [79].

Compared to other energy harvesting methods, WPH is advantageous in several respects, for example, its continuous availability regardless of day/night, and its independence to surrounding conditions such as temperature and weather. Furthermore, RF energy can penetrate into building materials, not requiring line-of-sight transmission. On the other hand, typical drawbacks of RF energy harvesting include comparatively large antenna size, and dependence on the RF power density in the surrounding area and the orientation of the antenna.

WPH receivers typically operates in the far-field of the electromagnetic energy source. The amount of power that can be received by the WPH receiver can be estimated using the Friis Equation [83]:

$$P_R = P_T \cdot G_T \cdot G_R \cdot \left( \frac{\lambda}{4 \cdot \pi \cdot R} \right)^2 \quad (1.2)$$

Despite of the ubiquitousness of RF energy, several important considerations must be made when choosing the frequency of the WPH receiver, including antenna dimension, availability of local signal sources, propagation loss over distance, and attenuation in building materials, sometimes requiring tradeoffs. For example, antenna dimension should be proportional to the wavelength of the EM wave. Therefore, higher frequency is often desirable for better antenna efficiency. However, the transmission range and penetration

depth decreases as frequency increases [83] [84]. The WPH receivers' operation frequency should be carefully selected based on the requirement of specific applications.

### 1.2.3 Architecture and Operation of WPH Systems

The block diagram of a typical WPH receiver is shown in Figure 1.6 [85]. RF energy is radiated from the ambient RF sources. The WPH receiver typically consists of an antenna to capture the RF energy. The antenna is impedance matched to a rectifier to convert the RF energy to DC. Subsequently, a voltage conversion unit converts the energy to a proper DC voltage level. Finally, the DC energy is supplied to a load or energy storage element (i.e. rechargeable battery / supercapacitor).

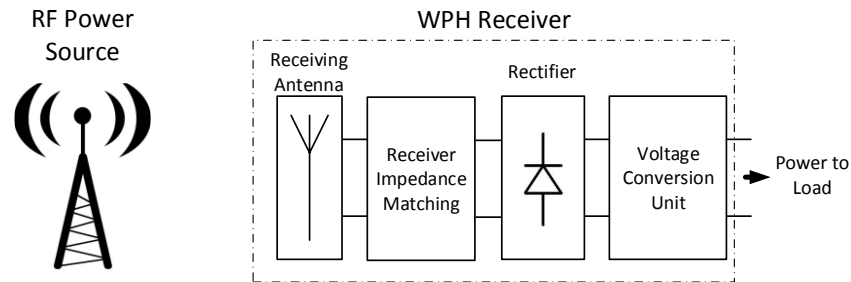


Figure 1.6. Block diagram of a typical WPH system

#### 1.2.3.1 Design of Antenna, Matching Network and Rectifier

In WPH receivers, the antenna, rectifier and the impedance matching network are usually co-designed. Because the RF voltage available at the antenna port is usually too small to overcome the threshold voltage of the rectifying devices, the impedance matching network is often designed with a high quality factor ( $Q$ ) to increase the RF voltage through  $Q$  multiplication. As the RF voltage can be boosted, the rectification efficiency is improved.

The available power from the antenna ( $P_{av}$ ) is given as (1.2) [86]:

$$P_{av} = \frac{\lambda^2}{4\pi} \cdot S_{RF} \cdot G \quad (1.2)$$

where  $G$  is the gain of the antenna,  $\lambda$  is the wavelength, and  $S_{RF}$  is the RF power density at the antenna position.

Since the RF power density in the ambient environment is usually small (0.0002 ~ 1  $\mu\text{W}/\text{cm}^2$  [79]), high-gain antennas or antenna arrays are often necessary to capture a sufficient amount of power. However, the sizes of high-gain antennas are usually large and sometimes even impractical. The issue is more severe at the low-end of the RF spectrum (MHz level or below) due to the long wavelengths at such frequencies.

The reflection coefficient  $\Gamma$  due to the impedance mismatch between the antenna and rectifier will affect the RF power delivered to the rectifier ( $P_{RF}$ ).  $P_{RF}$  can be written as (1.3):

$$P_{RF} = (1 - |\Gamma|^2) \cdot P_{av} \quad (1.3)$$

The DC power generated from the harvester's rectifier can be expressed as (1.4):

$$P_{dc} = \eta_{rect} \cdot P_{RF} \quad (1.4)$$

where  $\eta_{rect}$  is the rectification efficiency. Similar to the definition in WPT systems, the RF-DC efficiency is calculated as the output DC power over the available input power and is a function of reflection coefficient and rectification efficiency (1.5):

$$\eta_{RF-DC} \triangleq \frac{P_{dc}}{P_{av}} = (1 - |\Gamma|^2)\eta_{rect} \quad (1.5)$$

A well-designed impedance matching network should minimize the reflection coefficient ( $\Gamma$ ) by matching the impedance of the rectifier to the antenna, and thereby improving  $\eta_{RF-DC}$ .

### 1.2.3.2 Voltage Conversion Circuit

Since the DC output voltage from the rectifier usually doesn't satisfy the required voltage level of the load circuitry, a voltage conversion circuit is often needed for voltage conversion and regulation. Various circuits have been proposed for this purpose. A few examples include voltage multipliers, switched capacitor voltage converters, and switch mode voltage converters (buck/boost converters).

Voltage multipliers [87] (Figure 1.7) use a network of capacitors and diodes (or transistors) to achieve voltage conversion. It can be implemented as a completely passive network consuming no power for operation. However, voltage multipliers typically requires a relatively high RF input voltage to overcome the threshold voltages ( $V_{th}$ ) of the rectifying devices. Because of the poor conduction close to  $V_{th}$ , voltage multipliers tend to have a lower rectification efficiency compared to other voltage conversion circuits when the input power level is low.

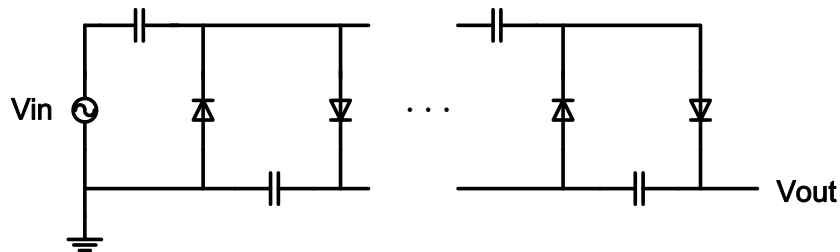


Figure 1.7. An example of voltage multiplier circuit.

Switched capacitor (SC) voltage converters [88] (Figure 1.8) use switching devices to alter the connection paths among an array of capacitors in order to achieve voltage conversion. This method can potentially achieve a high conversion efficiency ( $> 90\%$ ) when operating at a power level of mW or above. Also, realization of such a method doesn't

require inductors (compared to the buck/boost converters where inductors are essential), and therefore is favorable for on-chip designs (on-chip inductors usually occupy large chip area and are lossy) [89]. However, an external circuit is needed to generate the clock signal for driving the switches, which consumes considerable amount of extra power. At low power levels ( $\mu\text{W}$  levels), the power consumption of the clock generation circuit will significantly degrade the SC converter's efficiency. In addition, the requirements on the switch specifications are relatively stringent (such as short switching time, low ON resistance and high OFF resistance).

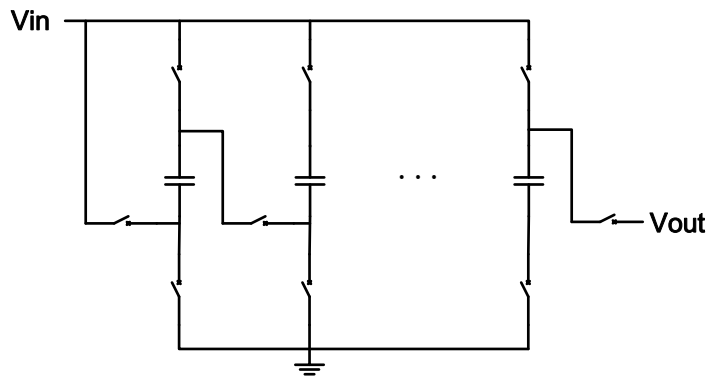


Figure 1.8. An example of switched capacitor voltage converter circuit.

Switch-mode voltage converters, such as buck converters (Figure 1.9 a) and boost converters (Figure 1.9 b) [90], are capable of achieving a high efficiency (higher than 90% in applications at mW or above, and as high as 60%~70% at  $\mu\text{W}$  range) while requiring a low input voltage. However, similar to SC converters, the buck/boost converters need to employ an active circuit for clock signal generation, which consumes power and constrains the overall efficiency especially at low input power levels.

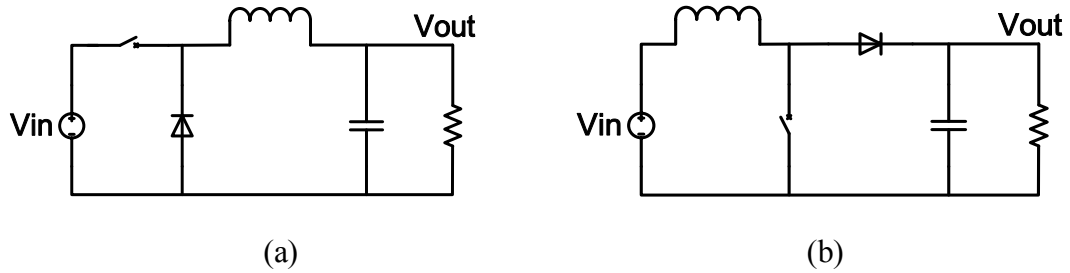


Figure 1.9. (a) Buck converter circuit; and (b) boost converter circuit.

Other types of conversion circuits have also been proposed, such as the self-starting converters [91] which have the advantage of extremely low start-up voltages at the sacrifice of efficiency.

#### 1.2.4 Challenges in the Design of WPH Systems

WPH receivers typically operate in the far field of the RF energy source. The wave propagation is influenced by the receivers' positions, presence of obstructions, coupling to surrounding objects, etc. Therefore, the ambient RF power density is small and unpredictable. In order to provide a sufficient amount of power, the following aspects have to be considered in a WPH system design:

- **Sensitivity:** a measure of the lowest RF power level that the WPH receiver can operate at.
- **Efficiency:** the ratio of the total DC output power over the total available RF input power.
- **Dynamic Range:** the range of RF input power levels where the efficiency of the WPH receiver can be maintained above a required level.

As mentioned before, it is usually necessary to boost the RF input voltage in order to overcome the threshold voltage of semiconductor rectifiers, therefore enhancing the harvester's sensitivity. High Q resonators are commonly used in WPH systems for boosting the RF voltage level (RF voltage can be amplified by Q multiplication). However, the narrow bandwidth of high Q resonators leads to several drawbacks. Narrow-band harvesters require careful tuning during installation, and are more vulnerable to frequency misalignment caused by the factors such as temperature, humidity, coupling to surrounding objects and component aging. This is unacceptable in situations where the harvester is expected to provide maintenance-free operation over a long period of time. Moreover, narrowband harvesters can only capture energy within a very narrow range of the RF spectrum. By designing wideband harvesters, EM energy from several RF sources within a wide frequency range can potentially be captured, thereby providing higher output power levels.

Another important challenge is to maintain high RF- DC efficiency within a wide range of input power levels. The conversion efficiency, which has significant influence on the system's performance, is dependent on both the reflection coefficient ( $\Gamma$ ) and the rectification efficiency ( $\eta_{rect}$ ), as described by equation (1.5). Similar to WPT systems, the design of wide dynamic WPH rectifiers is challenging since both  $\Gamma$  and  $\eta_{rect}$  are functions of the input power level due to the nonlinear behavior of RF rectifier devices [54] [57].

Active converters such as SC voltage converters and switch mode voltage regulators are commonly used in WPH receivers. These active converters face two common issues. Firstly, their operation requires a switch signal which has to be generated with an active circuit. The power consumption for the generation of the switch signal degrades the overall

efficiency of voltage converters, especially at low input power levels [89]. Secondly, since the switch signal generation requires a DC supply, a separate start-up circuit may be necessary for providing the initial DC power for the circuit to start its operation [92].

Intensive research has been conducted to address the aforementioned challenges. For example, several active frequency-tracking mechanisms have been proposed in order to address the narrow bandwidth of high-Q-resonator-based WPH systems [93]. In order to improve rectifiers' dynamic range, Maximum Power Point Tracking (MPPT) technology has been developed which alters the period and duty cycle of the switch signal to track the optimum operation point. To reduce the power consumed by the active converters, control circuits based on either low frequency oscillators [94] or voltage detectors [85] have been developed to switch the voltage converter between sleep and wake-up states. However, the existing solutions are far from being mature. For instance, the active frequency tracking or MPPT circuits not only require power for its operation (and therefore reduces system efficiency), but also add to the complexity and cost of the systems.

### **1.3 Dissertation Objectives and Contributions**

The objective of this research is to address the aforementioned design challenges in practical WPH and WPT systems. Firstly, nonlinear resonance circuits described by a group of second-order differential equations with cubic-order nonlinearities (known as the Duffing equations) will be introduced. The Duffing resonator circuits are capable of achieving a much wider bandwidth as compared to linear resonators. The Duffing resonators are used in SCMR WPT systems for automatic compensation for the variations

of coupling factor. Subsequently, a high sensitivity wireless power harvester which collects RF energy from AM broadcast stations is described for powering autonomous sensors in structural health monitoring (SHM) systems. The harvester successfully provides net DC energy within 6 miles away from a 50 kW AM broadcast station. The Duffing resonator approach is also applied to the WPH design to improve its tolerance to frequency misalignment. Moreover, the design of an adaptive power distribution rectifier array for enhancing the dynamic range of RF rectifiers is discussed. The rectifier array, which consists of merely passive components, has the advantages of low cost and low complexity. Such a rectifier array can be used in WPT and WPH circuits to improve their performance as power level changes.

The design methods of Duffing resonators and adaptive power distribution rectifier networks are not limited to a particular frequency range or power level. Therefore, this research is expected to have an impact on the broad area of WPT and WPH technologies. Furthermore, the wideband nonlinear resonators can enhance the gain-bandwidth product of resonant circuits. Since resonant circuits are widely used in many RF applications, the Duffing resonator circuits described in this dissertation can also impact many different aspects of RF electronics, for example, in the design of wideband impedance matching circuits. The wide dynamic range rectifier network developed in this research is also valuable in other applications where wide dynamic range rectifiers are needed, for example, in detectors for RF power measurements.

## 1.4 Dissertation Outline

This dissertation is organized as follows:

Chapter 2 discusses the Duffing resonator circuit and its properties, as well as their application in WPT systems. Such resonators can achieve a much wider bandwidth as compared to linear resonators. The design method of Duffing resonator circuit is applied to the design of a SCMR WPT system, and significantly improves its tolerance to the variations of coupling factor corresponding to different coupling distances.

Chapter 3 introduces the design of a high sensitivity AM frequency wireless power harvester for structural health monitoring (SHM) sensors. Benefiting from the long wavelengths and low propagation losses at such frequencies, the AM frequency harvesters do not rely on line-of-sight transmission. High sensitivity is achieved through optimizing the WPH receiver's antenna and rectifier, and by designing a power management circuit with very small power consumption. Details of the design, as well as simulation and measurement results, are provided. The method of Duffing resonator circuits is also applied to the design of WPH receivers, demonstrating significant advantages in improving the WPH system's tolerance to frequency misalignment and frequency drift.

Chapter 4 presents a low-cost and low-complexity wide dynamic range rectifier circuit for WPH and WPT applications. The rectifier circuit consists of several rectifier cells in conjunction with a passive power distribution network. The power distribution network is designed to adaptively divide the input RF power among these rectifier cells according to the input power level. The design methodology along with simulation and experimental results are provided. It will be shown that both the rectification efficiency and the impedance matching condition can be improved in a wide range of input power levels with

such a rectifier network, resulting in a much wider dynamic range as compared to single-diode rectifier circuits designed with the same type of diode.

Chapter 5 summarizes the contributions of this dissertation and discusses future directions for research in the area of WPH and WPT technologies.

# Chapter 2

## Duffing Resonator Circuits for Improving the WPT Systems' Tolerance to Coupling Factor Variations

### 2.1 Introduction

Wireless power transfer technology can reduce the need for power cord connections and usage of batteries, and therefore can benefit a wide range of commercial and defense applications. However, as mentioned in Chapter 1.1.3, one of the design challenges in the design of SCMR WPT systems is their low tolerance to the variations of coupling factor because of the frequency split phenomenon. The issue is more severe as the quality factors of the resonators increase, which is often necessary for achieving high transfer efficiency over long distances. However, it is often difficult to maintain a constant coupling factor in practical applications. In this chapter, a nonlinear resonance circuit is introduced to improve the SCMR WPT systems' tolerance to coupling factor variations. The nonlinear resonance circuit is characterized by a second-order differential equation with cubic nonlinearities, known as the Duffing equation. Therefore, the nonlinear resonance circuit is hereby referred to as the Duffing resonator.

Duffing resonators can achieve similar amplitudes as linear resonators with the same quality factor; however, they can achieve much wider bandwidth than linear resonators, therefore allowing for higher tolerance to coupling factor variations. It will be shown that high transfer efficiency can be maintained over a wide range of coupling distances by using such resonators in SCMR WPT systems.

## 2.2 Duffing Equation

The Duffing equation was proposed by Georg Duffing in 1918 [95] with the initial purpose of characterizing mechanical resonators/oscillators with a nonlinear restoring force. The basic form of the Duffing equation is usually written as (2.1) [96] [97]:

$$\ddot{x} + 2\gamma\dot{x} + \omega_0^2x + \epsilon x^3 = F\cos(\omega t) \quad (2.1)$$

where  $x$  is displacement,  $\gamma$  is the damping coefficient,  $\omega_0$  is the natural resonant/oscillate frequency,  $\epsilon$  is the third order nonlinearity coefficient, and  $F\cos(\omega t)$  is the excitation with the amplitude  $F$  and angular frequency  $\omega$ .

The steady state solution of (1) can be approximated as  $x(\omega, t) = A(\omega)\cos(\omega t - \theta)$ , where “ $A$ ” represents the frequency-dependent amplitude, and  $\theta$  represents the phase difference in reference to the excitation signal [96]. The amplitude “ $A$ ” as a function of excitation frequency can be determined from (2.2):

$$A^2 \left[ (\omega_0^2 - \omega^2) + \frac{3}{4}\epsilon A^2 \right]^2 + (2\gamma A\omega)^2 = F^2 \quad (2.2)$$

The typical amplitude response of a Duffing resonator is shown in Figure 2.1 [93]. As can be seen from Figure 2.1, unlike the frequency response of a linear resonator, the frequency response curve of a Duffing resonator is “tilted” to one side, resulting in a region

with three distinct real roots (referred to as the three-root region in this paper). The middle solution point in the three-root region is unstable, while the upper and lower points are stable (called equilibrium points) [96]. As a result, the steady state solution of such a system converges to one of the two equilibrium solutions depending on the initial conditions. If the circuit is excited to converge to the high-amplitude solution point, the amplitude will follow the upper curve when frequency changes in either direction, as long as the excitation frequency is lower than the right boundary of the three-root region, shown by the orange arrow in Figure 2.1. Once the right boundary of the three-root region is crossed, the amplitude drops, known as the jump down phenomenon. Therefore, the right boundary of the three-root region is referred to as the jump down point. However, if the circuit is excited to converge to the low-amplitude solution point, the amplitude will remain the small unless the three-root region's left boundary (the jump up point) is crossed. Therefore a properly designed nonlinear resonator can achieve a much wider bandwidth as compared to a linear resonator with the same Q value. The tilt direction of the amplitude-frequency curve is dependent on  $\epsilon$  (coefficient of the nonlinear term), as shown in Figure 2.2 [97]. Positive  $\epsilon$  causes the curve to tilt to the right (called hardening systems), while negative  $\epsilon$  causes the curve to tilt to the left (called softening systems) [97]-[99]. Either tilt direction can be used for bandwidth enhancement of resonators, while stronger nonlinearity is desirable to achieve a wider bandwidth.

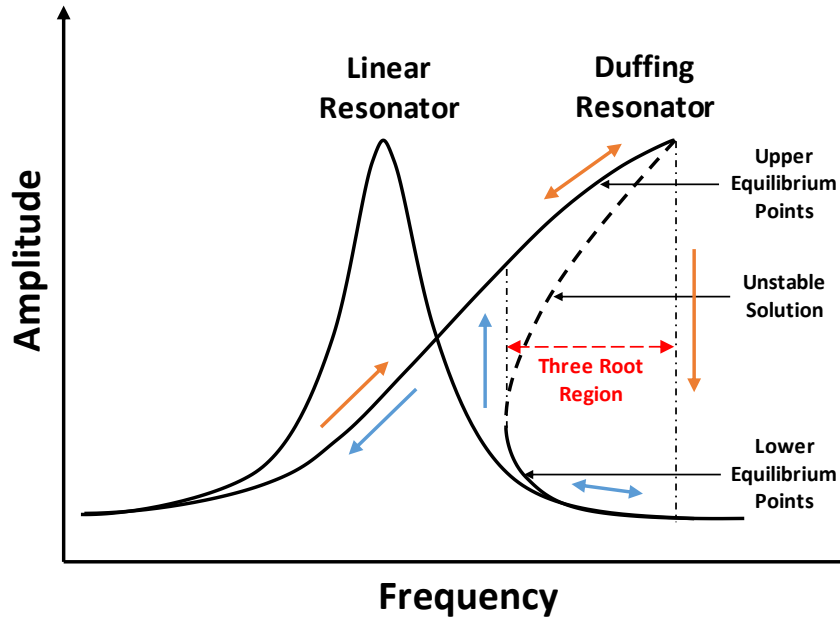


Figure 2.1. The amplitude-frequency response of a Duffing resonator circuit. Orange and blue arrows show the hysteresis loop and jump phenomenon.

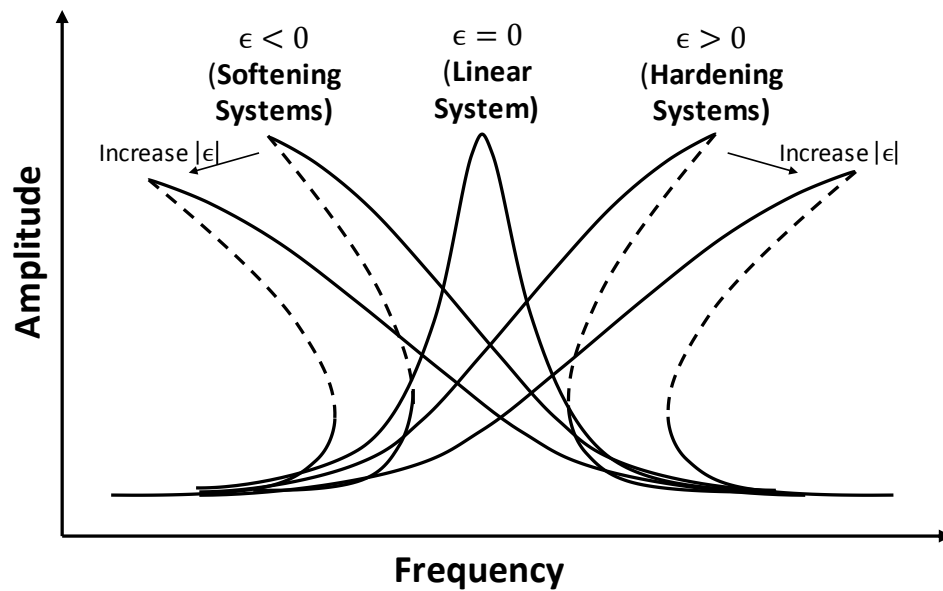


Figure 2.2. The amplitude-frequency response of Duffing resonator circuits with different nonlinearity coefficients ( $\epsilon$ ).

The properties of the Duffing equation have been investigated in a number of fields, including mathematics, physics, and engineering. Most engineering applications focus on its bifurcation and chaotic behavior for applications such as random number generation, signal processing, data storage, etc. [100]-[103]. It was not until recently that the hysteretic behavior was exploited to address the amplitude-bandwidth limitation of mechanical resonators. In [104] and [105], a Duffing-type mechanical resonance structure (machined with the MEMS technology) was developed for vibrational energy scavenging. The stretching force of the material was used to provide the 3<sup>rd</sup>-order nonlinearity. In this dissertation, the Duffing nonlinear resonance is exploited with an electrical circuit for bandwidth enhancement of the high Q resonator circuits, and used for improving the tolerance to coupling factor variations of SCMR WPT systems.

## **2.3 Electrical Realization of Duffing Resonance Systems**

### **2.3.1 Duffing Resonator Circuit Analysis**

The basic circuit configuration of a Duffing nonlinear resonance circuit is shown in Figure 2.3. The circuit consists of a sinusoidal excitation voltage  $e(t) = V_s \cdot \cos(\omega t)$ , an inductor L, a resistor R (which represents both the intrinsic loss of the resonator and the loss due to the load) and a nonlinear capacitor C. The nonlinear capacitor has a symmetric C-V relationship, i.e.  $C(v_C) = C(-v_C)$ , which can be either bell-shaped (Figure 2.4 (a)), or well-shaped (Figure 2.4 (b)).

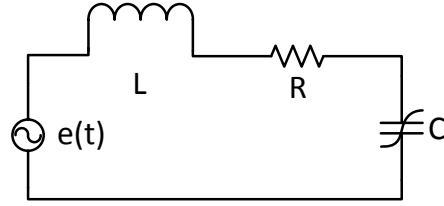


Figure 2.3. Basic diagram of a Duffing resonant circuit using a nonlinear capacitor

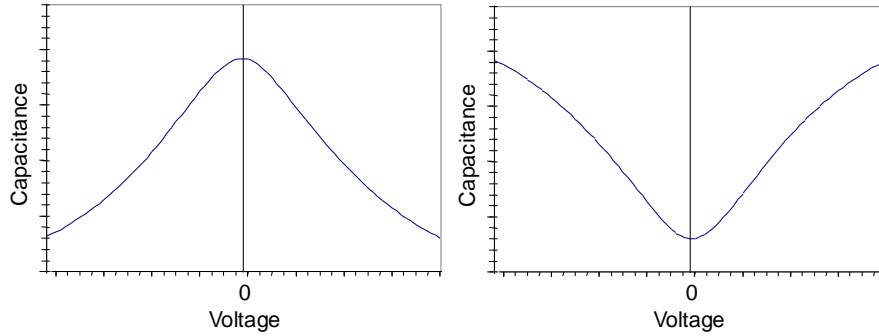


Figure 2.4. Symmetric C-V curves for nonlinear capacitors: (a) bell-shaped curve and (b) well-shaped curve.

The dynamic equation that describes the circuit's time domain behavior is given by (2.3):

$$v_C(t) + R \frac{dq_C}{dt} + L \frac{d^2q_C}{dt^2} = e(t) \quad (2.3)$$

where  $e(t) = V_s \cdot \cos(\omega t)$  is the excitation voltage,  $v_C(t)$  is the voltage across the nonlinear capacitor, and  $q_C$  is the amount of charge stored in the capacitor. For any voltage  $v_C$  across the capacitor, the charge amount can be expressed as  $q_C = f(v_C) = \int_0^{v_C} C(v_C) \cdot dv_C$ , which can then be written as (2.4):

$$v_C = f^{-1}(q_C) \quad (2.4)$$

Since the nonlinear capacitor has a symmetric C-V relationship, the even order terms in the Taylor expansion of (2.4) vanish. Neglecting the higher than third-order terms for simplicity, the Taylor series expansion of (2.4) is given by (2.5):

$$v_C = \frac{1}{a_1} q_C + \frac{1}{a_3} q_C^3 \quad (2.5)$$

Substituting (2.5) into (2.3) results in (2.6):

$$\frac{d^2 q_C}{dt^2} + \frac{R}{L} \cdot \frac{dq_C}{dt} + \frac{1}{La_1} \cdot q_C + \frac{1}{La_3} \cdot q_C^3 = \frac{V_s}{L} \cdot \cos(\omega t) \quad (2.6)$$

It worth mentioning that (2.6) has the same form as the Duffing equation described in (2.1). The solution of (2.6) can also be written as a sinusoidal function  $q_C = A \cos(\omega t - \theta)$ , where  $A$  is the amplitude of time-dependent charge amount; i.e., the maximum amount of charge stored in the capacitor during one period, and  $\theta$  represents the phase difference with respect to the excitation signal. In the nonlinear resonator, the restoring effect is contributed by both the linear term ( $\frac{1}{La_1} \cdot q_C$ ) and the nonlinear term ( $\frac{1}{La_3} \cdot q_C^3$ ). An equivalent linear capacitance  $C_{eff}$  is defined to quantify the restoring effect contributed by the third-order nonlinear term,

$$\int_0^{\frac{T}{2}} \left( \frac{1}{La_3} \cdot (A \cdot \cos(\omega t))^3 \right) \cdot d(A \cdot \cos(\omega t)) = \int_0^{\frac{T}{2}} \left( \frac{1}{LC_{eff}} \cdot (A \cdot \cos(\omega t)) \right) \cdot d(A \cdot \cos(\omega t)) \quad (2.7)$$

From equation (2.7),  $C_{eff}$  can be calculated as (2.8):

$$C_{eff} = \frac{a_3}{\frac{3}{4} A^2} \quad (2.8)$$

The natural frequency of the resonator  $\omega_0$  in the presence of the nonlinear restoring term can thus be calculated as (2.9):

$$\omega_0 = \sqrt{\frac{1}{L} \left( \frac{1}{a_1} + \frac{1}{C_{eff}} \right)} = \sqrt{\frac{1}{L} \left( \frac{1}{a_1} + \frac{\frac{3}{4}A^2}{a_3} \right)} \quad (2.9)$$

The circuit's amplitude-frequency relationship can be determined from the phasor form of equation (2.6), given by (2.10):

$$(j\omega)^2 Z + \frac{R}{L} (j\omega)Z + \left( \frac{1}{La_1} + \frac{1}{LC_{eff}} \right) Z = \frac{V_S}{L} \quad (2.10)$$

Substituting (2.8) in (2.10) results in (2.11):

$$A^2 \left( \frac{1}{La_1} + \frac{3}{4} \cdot \frac{1}{La_3} A^2 - \omega^2 \right)^2 + \left( \frac{R}{L} \cdot A\omega \right)^2 = \left( \frac{V_S}{L} \right)^2 \quad (2.11)$$

The charge amount “A” can be determined from (2.11) as a function of  $\omega$ . Subsequently, the resonant voltage  $v_C$  can be calculated from (2.4) using  $q_C = A \cos(\omega t)$ .

Equation (2.9) implies that the resonant frequency  $\omega_0$  is dependent on the charge amount “A”. The amplitude-dependent resonant frequency of the circuit can be exploited to track the excitation frequency. For example, a nonlinear capacitor with a bell-shaped C-V curve shown in Figure 2.4 (a) has  $a_3 > 0$ . Resonators containing such varactors will have a frequency response tilted to the right (a hardening system as shown in Figure 2.2). Assuming that the circuit initially converges to its upper equilibrium solution, when the excitation frequency  $\omega$  decreases, the charge amount “A” decreases (as can be seen in Figure 2.1). According to (2.9), the decrease in A will lead to decrease in  $\omega_0$ . Conversely, as  $\omega$  increases, “A” will increase, causing  $\omega_0$  to increase. Therefore, the circuit's natural resonance frequency  $\omega_0$  automatically tracks the variation of excitation frequency  $\omega$  in both directions (either increasing or decreasing). Hence, the voltage amplitude drop caused by resonator's frequency detuning is significantly reduced.

From another point of view, this process can be understood as a negative feedback process, as shown in Figure 2.5. Because of the bell-shaped C-V characteristic of the nonlinear capacitor, the average capacitance during one resonance cycle is dependent on “A”: as the amplitude value increases, the average capacitance decreases, and vice versa. Since the inductance value is fixed, the circuit’s natural resonance frequency is determined by the average capacitance over one period. Therefore, the amplitude-dependent nonlinear capacitance provides a negative feedback response, which reduces the difference between the excitation frequency and the natural resonance frequency of the circuit. At the same time, being able to track the excitation frequency allows for automatic compensation for the circuit’s parameters variations due to component aging or changes in surrounding condition.

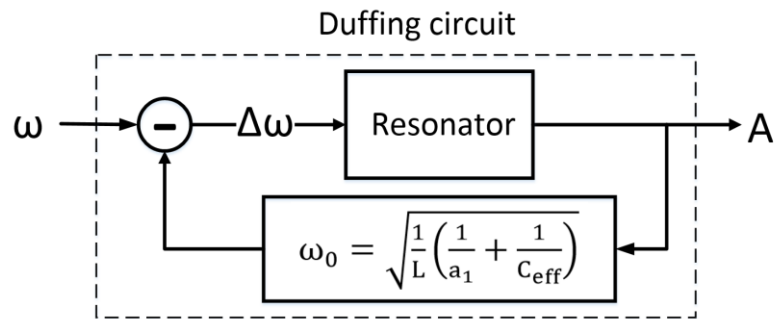


Figure 2.5. Negative feedback process in a Duffing resonator circuit, showing the feedback term provided by the nonlinear capacitor.

### 2.3.2 Choice of Devices for Providing the Required Nonlinearity in Duffing Resonator Circuits

The symmetric C-V curve for a nonlinear capacitor can be provided by anti-series connected varactor diodes [106] (Figure 2.6 (a)), ferroelectric varactor devices [107] (Figure 2.6 (b)), or ceramic capacitors under high driven voltages [108] (Figure 2.6 (c)), depending on the power level and voltage swing. It worth mentioning that the required nonlinearity to achieve the Duffing resonance behavior can also be provided by a nonlinear inductor whose inductance is an even function of the conduction current  $i$ . Nonlinear capacitors are used in this research since they are widely available on the market with well described properties.

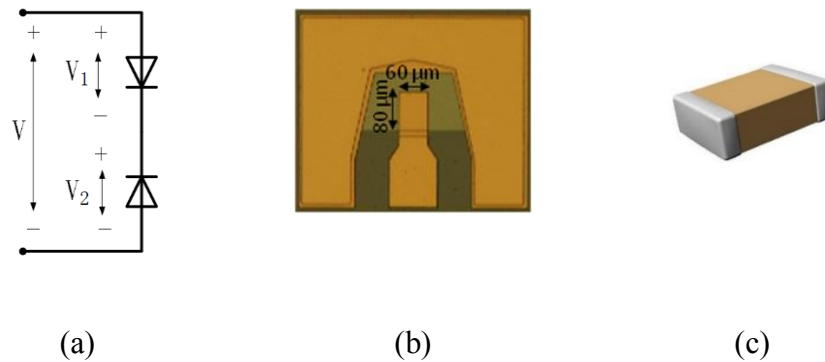


Figure 2.6. (a) Anti-series connected varactor diode pair, (b) an example of ferroelectric barium strontium titanate (BST) varactor, and (c) an example of ceramic capacitor: C2225C102KHRAC SMD

### 2.3.2.1 Duffing resonator circuits based on anti-series connected varactors for low power level applications

Anti-series connected varactor diode pairs are useful for the design of low power WPT applications. The devices usually exhibit strong nonlinearity with a voltage amplitude of several volts [109].

Capacitance-voltage relationship for a single varactor diode is given by (2.12):

$$C = \frac{C_{jo}}{\left(1 + \frac{V_R}{V_J}\right)^m} + C_p \quad (2.12)$$

where  $C_{jo}$  is the junction capacitance,  $V_R$  is the reverse bias voltage,  $V_J$  is the built-in junction voltage (around 0.7 V for silicon and 1.3 V for gallium arsenide), and  $m$  is the grading coefficient. The parametric capacitance  $C_p$  is usually small and can be neglected.

Thus, (2.12) can be translated into a Maclaurin series expression as (2.13):

$$C = \sum_{n=0}^{\infty} \frac{C_V^{(n)}(0)}{n!} V_R^n \quad (2.13)$$

where the first three terms of the series are given in (2.14):

$$\left\{ \begin{array}{l} k_0 = C_V(0) = C_{jo} \\ k_1 = \frac{C_V'(0)}{1!} = -C_{jo} \frac{m}{V_J} \\ k_2 = \frac{C_V''(0)}{2!} = C_{jo} \frac{m(m+1)}{2 \cdot V_J^2} \end{array} \right. \quad (2.14)$$

where  $K_n$  are the coefficients of the Maclaurin series.

Neglecting higher than third-order terms results in (2.15):

$$C_V(V_C) \approx k_0 + k_1 V_C + k_2 V_C^2 \quad (2.15)$$

By connecting two varactors in anti-series configuration, and assuming that the two diodes are exactly the same, the following equation can be derived:

$$\begin{cases} C_V(V_1) = k_0 - k_1V_1 + k_2V_1^2 \\ C_V(V_2) = k_0 + k_1V_2 + k_2V_2^2 \end{cases} \quad (2.16)$$

The charge amount on each varactor can be calculated from  $Q_C = \int_0^V f(v) \cdot dv$  as (2.16):

$$\begin{cases} Q_1(V_1) = k_0V_1 - \frac{k_1}{2}V_1^2 + \frac{k_2}{3}V_1^3 - \frac{k_3}{4}V_1^4 \\ Q_2(V_2) = k_0V_2 + \frac{k_1}{2}V_2^2 + \frac{k_2}{3}V_2^3 + \frac{k_3}{4}V_2^4 \end{cases} \quad (2.17)$$

Assuming the two diodes are exactly the same, equation (2.17) can be rewritten in the form of (2.18) by applying the series reversion technique [106]:

$$\begin{cases} V_1 = \frac{Q_C}{k_0} + \frac{k_1}{2k_0^3}Q_C^2 + \frac{1}{k_0^5}\left(\frac{k_1^2}{2} - \frac{k_0k_2}{3}\right)Q_C^3 \\ V_2 = \frac{Q_C}{k_0} - \frac{k_1}{2k_0^3}Q_C^2 + \frac{1}{k_0^5}\left(\frac{k_1^2}{2} - \frac{k_0k_2}{3}\right)Q_C^3 \end{cases} \quad (2.18)$$

or

$$V = V_1 + V_2 = \frac{2Q_C}{k_0} + \frac{2}{k_0^5}\left(\frac{k_1^2}{2} - \frac{k_0k_2}{3}\right)Q_C^3 \quad (2.19)$$

Comparing (2.19) with (2.5), coefficients  $a_1$  and  $a_3$  in the Duffing equation (2.6) can be derived as in (2.20):

$$\begin{cases} a_1 = \left(\frac{2}{k_0}\right)^{-1} = \frac{C_{j0}}{2} \\ a_3 = \left(\frac{2}{k_0^5}\left(\frac{k_1^2}{2} - \frac{k_0k_2}{3}\right)\right)^{-1} = \frac{3V_j^2}{m(2m-1)}C_{j0}^3 \end{cases} \quad (2.20)$$

Equation (2.20) allows for determination of the nonlinear coefficients for the Duffing equation (Eq. (2.6)) based on the specs of the varactor diodes.

### 2.3.2.2 Duffing resonator circuits based on ferroelectric varactor devices for medium-to-high power level applications

High-permittivity ferroelectric materials exhibit a strong electric-field-dependent dielectric permittivity that can be used to design varactors up to GHz frequencies. These devices are suitable for Duffing resonator circuits used in medium-to-high power WPT systems, and demonstrates strong nonlinearity with voltage amplitudes of tens to hundreds of volts [107]. One example of such a device is ferroelectric barium strontium titanate (BST) based varactors. BST-based varactors exhibit very small losses, with loss tangents as small as 0.005 at high frequencies. As an example, measured tunability curve of a typical BST-based varactors, as well as its loss tangent, is shown in Figure 2.7 [110]. The peak capacitance at zero applied bias voltage is  $C_0$ . As the applied DC bias increases, the capacitance decreases.

The BST varactors' C-V response is given by (2.21) [111] where  $V_2$  is the bias voltage when  $C = \frac{1}{2} C_0$ .

$$C(V) = \frac{C_0}{1 + \left(\frac{4V_C}{3V_2}\right)^2} \quad (2.21)$$

Based on (2.21),  $V_C$  can be derived as (2.22):

$$V_C = \frac{1}{C_0} \cdot Q_C + \frac{16}{9V_2^2 C_0^3} \cdot Q_C^3 + \dots \quad (2.22)$$

Comparing (2.22) with (2.5), coefficients  $a_1$  and  $a_3$  in the Duffing equation (2.6) can be derived as (2.23):

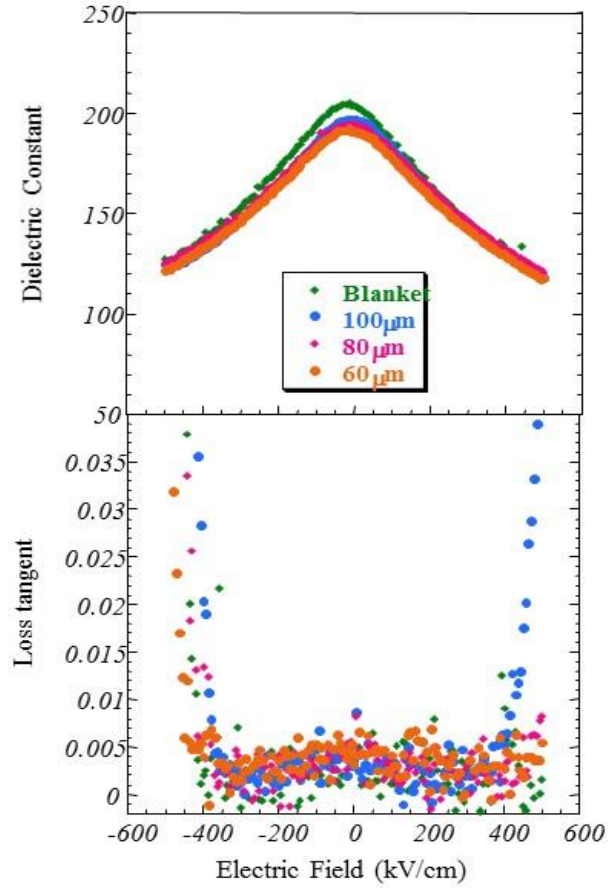


Figure 2.7. An example of BST varactors: measured dielectric tunability curve and loss tangent for BST varactors with different sizes [110]

$$\begin{cases} a_1 = C_0 \\ a_3 = \frac{9V_2^2 C_0^3}{16} \end{cases} \quad (2.23)$$

Equation (2.23) allows for determination of the nonlinear coefficients for the Duffing equation (Eq. (2.6)) based on the specs of the BST varactor.

### 2.3.2.3 Duffing resonator circuits based on nonlinear ceramic capacitors for high-power applications

Ceramic capacitors with high dielectric constants ( $\epsilon$ ) exhibit strong voltage dependent capacitance behavior under high voltage amplitude excitation, which can also be exploited to design Duffing resonator circuits. The nonlinearity characteristic of ceramic capacitors has been studied in [112]-[113]. Such devices are suitable for high power WPT applications because of their capability of withstanding high voltage amplitude swings. For instance, Figure 2.8 shows the nonlinear characteristic of a 3.0 kV, 1.0 nF multilayer ceramic commercial capacitor (MLCC).

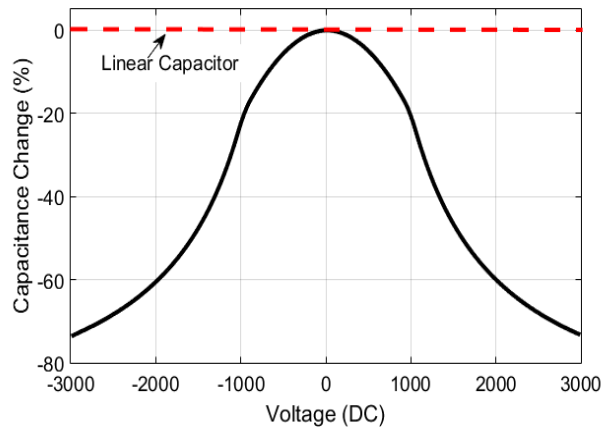


Figure 2.8. An example of nonlinear ceramic capacitors: tunability curve of a 3.0 kV, 1.0 nF multilayer ceramic commercial capacitor

In circuit modeling, the non-linearity of a capacitor could be represented by high-order polynomial functions such as (2.24):

$$Q = k_1V + k_2V^2 + k_3V^3 + k_4V^4 \quad (2.24)$$

The even order coefficients are usually negligible since the device is bilateral symmetric. For example, Q-V polynomial coefficients of 1  $\mu$ F MLCC as reported in [114] are:  $k_1 = 1 \times 10^{-6} F$ ,  $k_2 = 5 \times 10^{-16} F$ ,  $k_3 = -5 \times 10^{-10} F$ , and  $k_4 = -3 \times 10^{-18} F$ . Equation (2.24) can be inversely written in the following form:

$$V = k_1^{-1}Q - k_1^{-4}k_3Q^3 + \dots \quad (2.25)$$

Comparing (2.25) with (2.5), the coefficients in the Duffing equation  $a_1$  and  $a_3$  can be derived as (2.26):

$$\begin{cases} a_1 = k_1^{-1} \\ a_3 = k_1^{-4}k_3 \end{cases} \quad (2.26)$$

Equation (2.26) allows one to determine the nonlinear coefficients for the Duffing equation (Eq. (2.6)) based on the specs of the ceramic capacitor.

Therefore, at least three different nonlinear capacitors can be identified to design Duffing resonator circuits for WPT and WPH systems, covering a wide range of operating power levels.

## 2.4 Properties of Duffing Resonator Circuit

The properties of Duffing resonator circuit can be studied by mathematically solving equation (2.11). Matlab scripts to predict the behavior of Duffing resonators from (2.11) for different types of nonlinear devices (anti-series varactor diodes, BST-varactors, etc.) are included in Appendix A. To analyze the properties of Duffing resonator circuits, the Duffing resonator circuit shown in Figure 2.3 is used for evaluation. BST varactors are

used as the nonlinear capacitor in the Duffing resonator. The circuit parameters as listed in Table 2.1 are used in the calculation.

Table 2.1. Component specifications for the WPH system design

<b>Component</b>	<b>Specification</b>
<b>Frequency Band</b>	Approximately 1 MHz
<b>Vs (excitation voltage)</b>	0.5 V
<b>L (inductance)</b>	900 $\mu$ H
<b>R (resistance)</b>	50 $\Omega$
<b>Varactor Type</b>	BST varactor
$C_0$ (zero bias capacitance)	100 pF
$V_2$ (bias voltage at half capacitance)	5 V

### 2.4.1 Deflection and Bandwidth Enhancement

The frequency response of the Duffing resonator circuit is computed and compared with a conventional LC resonator with the same Q, with results shown in Figure 2.9. The high-amplitude equilibrium points within the three root region of the Duffing resonator are plotted as the blue curve. Frequency response of the Duffing resonator circuit deflects to the right (high frequency) side, which results in a much wider bandwidth than the linear LC resonator used for comparison. Duffing resonator has a lower peak value of amplitude than the linear resonator circuit, but the difference is small. The small difference is likely

due to the fact that only the first-order and third-order terms were taken into calculation when computing the response of the Duffing circuit. Considering the energy converted to the higher order harmonics will slightly raise the amplitude of the Duffing circuit.

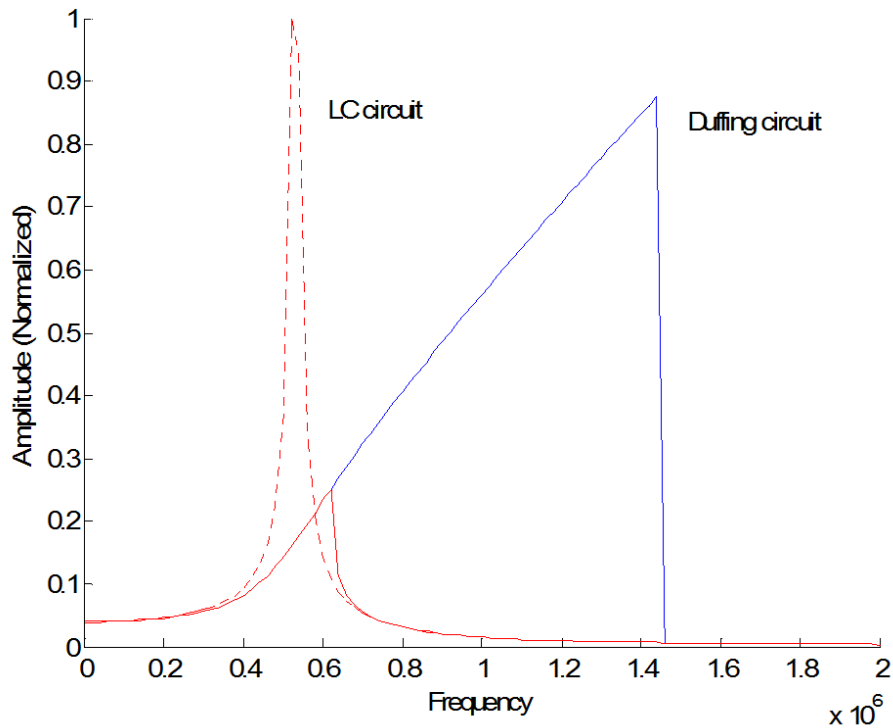


Figure 2.9. The frequency response of the Duffing resonator circuit, in comparison with a LC circuit with the same Q. For the Duffing resonator, the solid blue curve shows the high-amplitude equilibrium points at different frequencies, while the solid red curve shows the low-amplitude equilibrium points. The dashed red curve shows the amplitude response of the linear resonator used for comparison.

## 2.4.2 The Influence of Power Level on the Circuit Operation

Figure 2.10 shows the circuit's amplitude-frequency relationship at different excitation voltage levels ranging from  $V_s=0.3$  V to  $V_s=0.6$  V. The slope of the amplitude-frequency

curves is largely independent on the available power levels, which indicates that the nonlinear resonance circuit behaves as an ideal source (constant output voltage) at any given frequency regardless of the power level from the source. Moreover, as the available power level increases, the peak amplitude increases, and the jump-down point is shifted to higher frequencies. The underlying reason is that the average capacitance of the varactor decreases as the voltage swing across it increases.

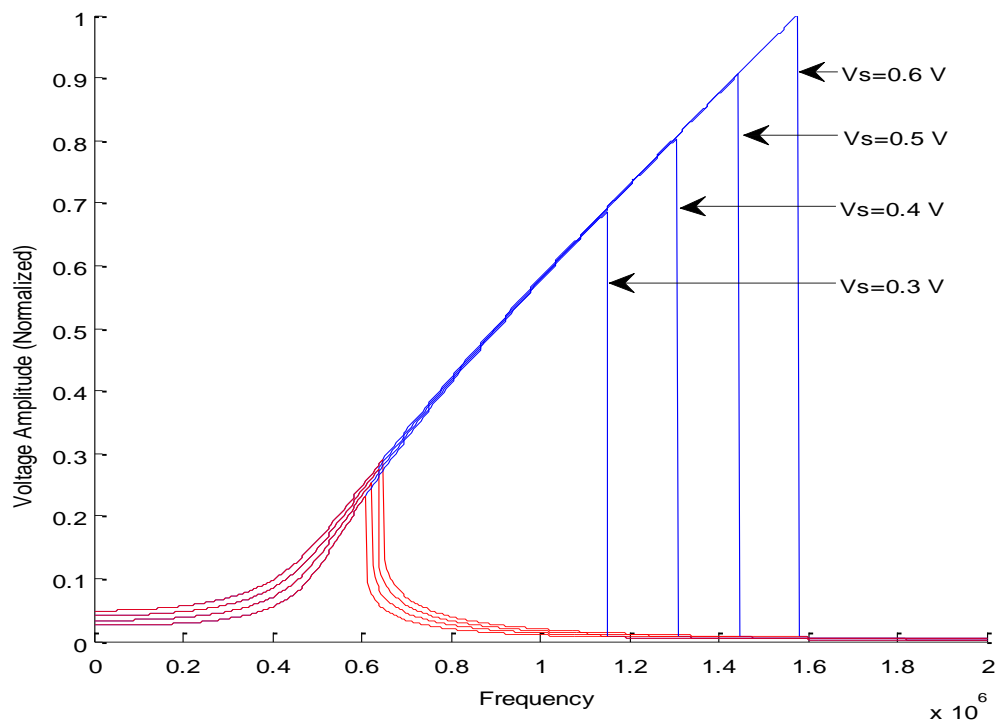


Figure 2.10. The frequency response of the Duffing resonator circuit for different excitation amplitudes ( $V_s$ ) from 0.3 V to 0.6 V. The solid blue curve shows the high-amplitude equilibrium points at different frequencies, while the solid red curve shows all the low-amplitude equilibrium points.

### 2.4.3 The Influence of Quality Factor on the Circuit Operation

The circuit's frequency response as a function of different Q values is calculated and shown in Figure 2.11. The series resistance (R) is varied to change Q values of the circuit. The jump-down point occurs at higher frequencies, and the peak amplitude reaches higher values as the circuit's Q increases. Similar to the influence of power level on the circuit operation, the amplitude-frequency plots for different Q values have similar slopes, which indicates that the nonlinear resonance circuit behaves as an ideal source regardless of Q values which can be influenced by the load resistance that the resonator is connected to. At the same time, the bandwidth of the resonator, which is defined as the frequency band where the amplitude is greater than  $1/\sqrt{2}$  of peak amplitude, are almost constant as Q varies. Therefore, the bandwidth for the nonlinear resonator does not rely on Q. This behavior is different from a linear resonator's response whose bandwidth is inversely proportional to Q.

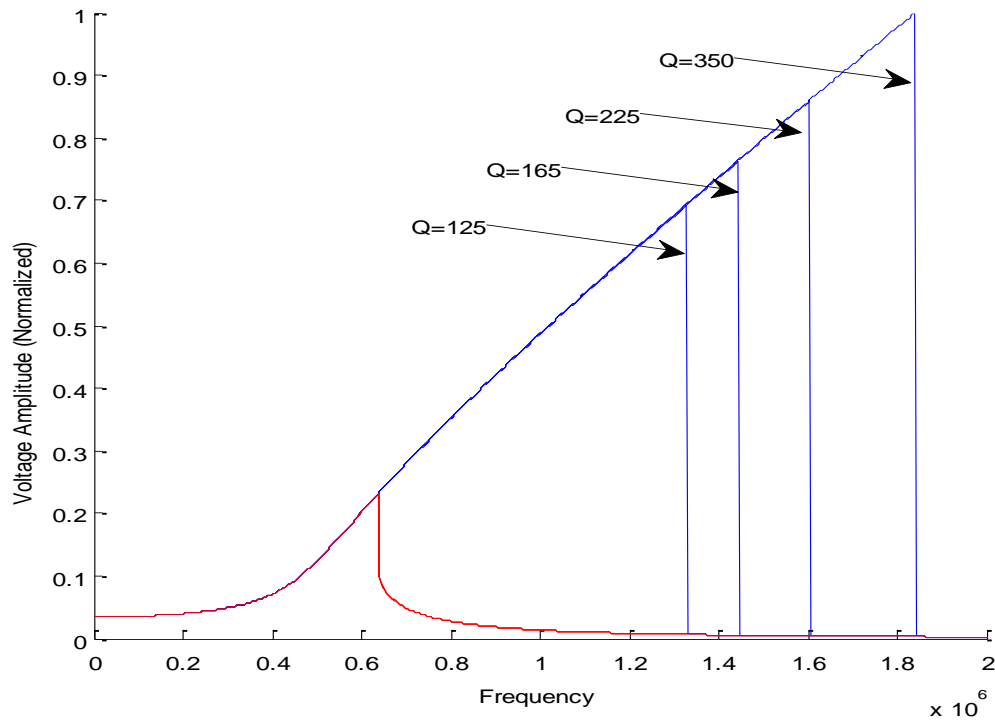


Figure 2.11. The frequency response of the Duffing resonator circuit for different  $Q$  values from 125 to 350. The solid blue curve shows the high-amplitude equilibrium points at different frequencies, while the solid red curve shows the low-amplitude equilibrium points.

#### 2.4.4 The Influence of Component Parameters

In the time domain differential equation of the circuit (2.6), coefficient of the linear term is given by  $1/(La_1)$ , while the coefficient of the third-order nonlinear term is given by  $1/(La_3)$ . The influence of  $L$ ,  $a_1$  and  $a_3$  on the frequency response of the Duffing resonator circuit are studied in this section.

### 2.4.4.1 The influence of linear inductance (L) on circuit operation

The simulated voltage amplitudes versus the excitation frequency for a nonlinear resonance circuit using different inductance values are shown in Figure 2.12. Inductance values ranging from  $700 \mu\text{H}$  to  $1000 \mu\text{H}$  are used for calculation, while other parameters are set as values in Table 2.1.

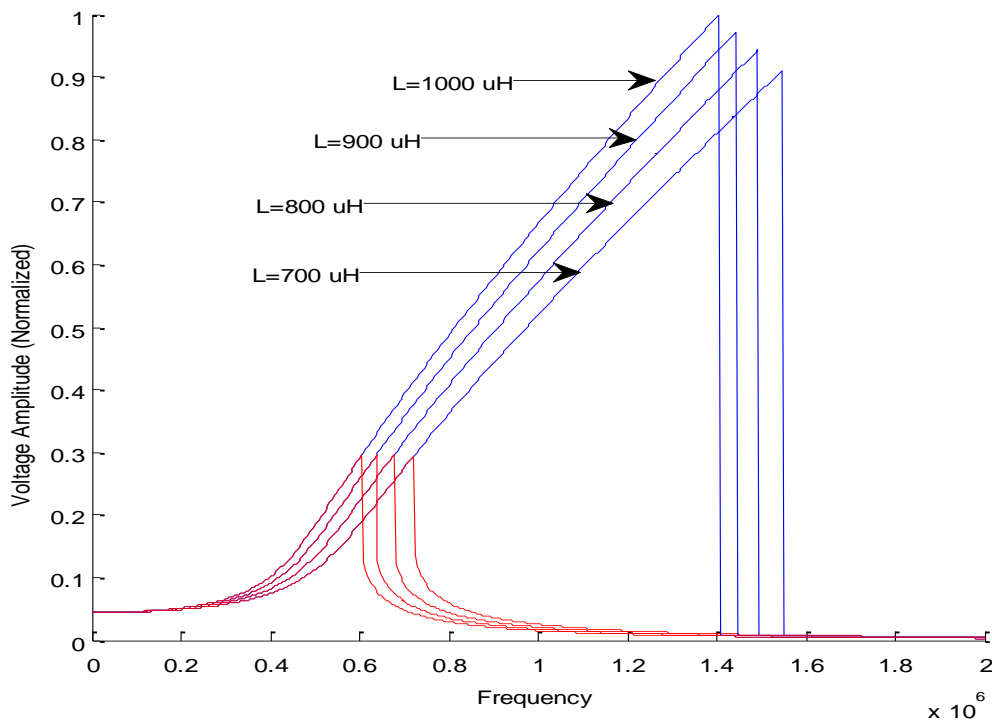


Figure 2.12. The frequency response of the Duffing resonator circuit for different inductance values ranging from  $700 \mu\text{H}$  to  $1000 \mu\text{H}$ . The solid blue curve shows the high-amplitude equilibrium points, while the solid red curve shows the low-amplitude equilibrium points.

In Figure 2.12, the voltage level reaches the peak amplitude at lower frequencies as the inductance value increases, because the natural resonance frequency of the circuit ( $\omega =$

$1/\sqrt{LC}$ ) decreases. At the same time, the peak voltage amplitude value increases with inductance, because the circuit Q increases with  $L$  ( $Q = \omega L/R$ ). Consequently, higher peak voltage amplitudes at resonance frequency are achieved, as illustrated in Section 2.4.3. It's also worth mentioning that when operating at a given frequency (away from the jump-down point), the voltage amplitude changes only slightly when inductance varies (no catastrophic failure until the jump-down point).

#### 2.4.4.2 The Influence of Nonlinear Capacitor (C) on Circuit Operation

As mentioned before, the coefficients  $a_1$  and  $a_3$  in the Duffing equation (2.6) is determined by the parameters of the nonlinear capacitor in the circuit. The influence of the nonlinear capacitor's parameters on circuit operation are studied through simulation. The BST-based varactor is used in the Duffing resonator as the nonlinear capacitor. In such resonators, the coefficients  $a_1$  and  $a_3$  can be determined by equation (2.19) from the BST varactor parameters  $C_0$  (zero-bias capacitance) and  $V_2$  (the voltage at which the capacitance drops to  $C_0/2$ ).

The frequency response of the Duffing resonator circuits containing BST-varactors with different  $C_0$  values are shown in Figure 2.13. All the other parameters of the circuit remain the same as Table 2.1. It can be seen that the circuit reaches the peak amplitude at lower frequencies as  $C_0$  increases due to the decreasing natural frequency of the circuit ( $\omega = 1/\sqrt{LC}$  and average capacitance  $C$  increases as  $C_0$  increases). At the same time, the deflection of the amplitude-frequency curves is less obvious with greater  $C_0$ . This is because the nonlinearity coefficient  $\epsilon = 1/(La_3)$  in the circuit equation (2.6) is inversely

proportional to  $C_0^3$  (illustrated in equation (2.19)). Therefore,  $\epsilon$  decreases as  $C_0$  increases.

A Duffing resonator with smaller  $\epsilon$  will have less deflection, which agrees with Figure 2.2.

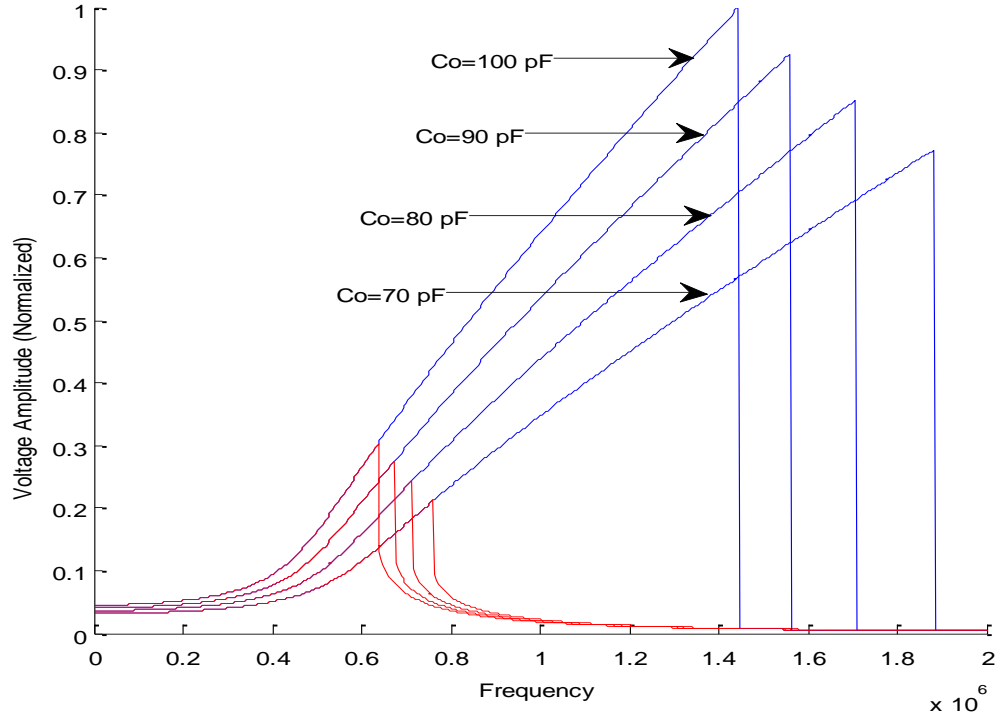


Figure 2.13. The frequency responses of the BST-based Duffing resonator circuits with different  $C_0$  (zero-bias capacitance) values. The solid blue curve shows the high-amplitude equilibrium points, while the solid red curve shows the low-amplitude equilibrium points.

The frequency response of the Duffing resonator circuits containing BST-varactors with different  $V_2$  values are shown in Figure 2.14. The slope of the amplitude-frequency curves is steeper with greater  $V_2$ . This observation can also be attributed to the fact that the nonlinear coefficient  $\epsilon$  is inversely proportional to  $V_2^2$  (according to equation (2.19)), and greater  $V_2$  leads to smaller  $\epsilon$  and less deflection. Also, when operating at a given frequency

away from the jump-down point, the voltage amplitude changes only slightly with  $V_2$  (no catastrophic failure until the jump-down point).

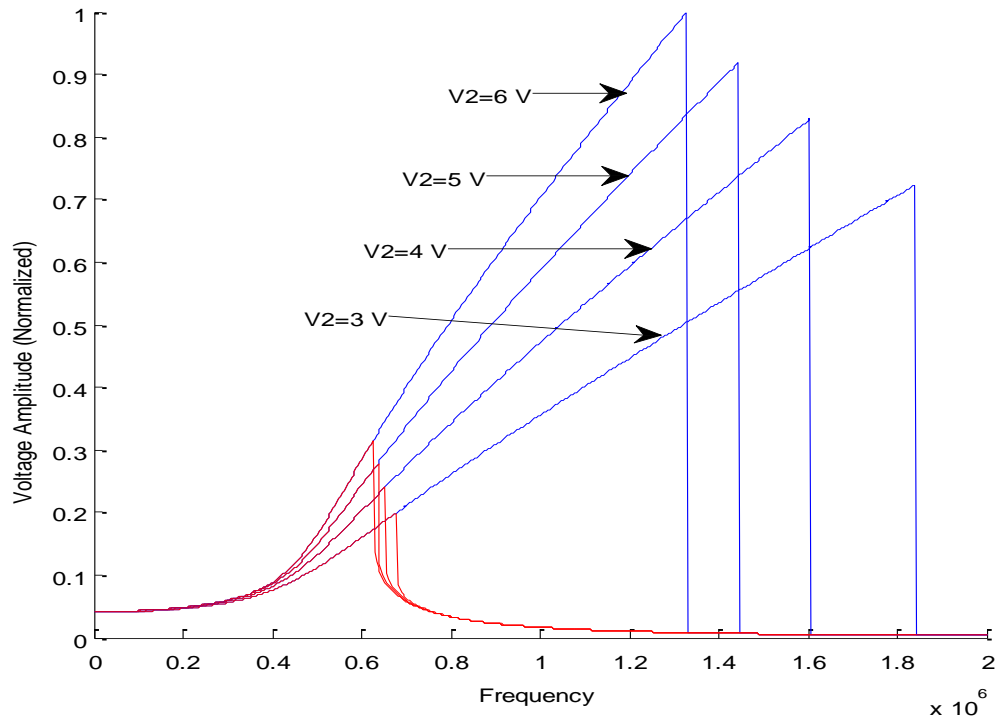


Figure 2.14. The frequency responses of the BST-based Duffing resonator circuits with different  $V_2$  values. The solid blue curve shows the high-amplitude equilibrium points, while the solid red curve shows the low-amplitude equilibrium points.

## 2.4.5 Experimental Verifications of the Properties of Duffing Resonator Circuits

### 2.4.5.1 Circuit Design

A Duffing resonator circuit was designed and tested at approximately 1 MHz frequency. The circuit schematic for the Duffing resonator is shown in Figure 2.15.  $V_S$  and  $R_S$  represent the excitation voltage and source resistance, respectively.  $L$  is a linear inductor with an inductance of  $900 \mu\text{H}$  and a  $Q$  value of 160. Four pairs of anti-series connected varactor diodes (SMV1249 from Skyworks) are used to provide the bell-shaped C-V curve required for the nonlinear resonance circuit. The  $Q$  of the resonator circuit is controlled by changing the resistance  $R_{series}$  of a resistor connected in series.

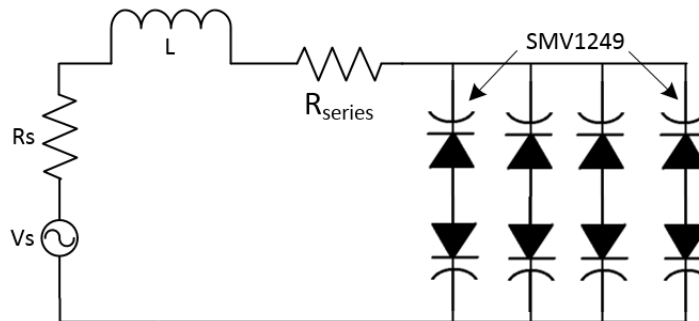


Figure 2.15. Diagram of the 1 MHz WPH system employing a Duffing resonator

The SMV1249 varactor diode used for this design is a silicon hyperabrupt junction varactor. It shows strong nonlinearity within the tuning range of  $0 \sim 5 \text{ V}$ . The specifications of the SMV1249 varactor (given by Equation 2.12) are provided as Table 2.2 according to the manufacturer.

Table 2.2. Specifications of SMV1249 varactor diode

$C_{j0}$ (junction capacitance)	36.4 pF
$V_j$ (built-in junction voltage)	80 V
$m$ (grading coefficient)	70
$C_p$ (parasitic shunt capacitance)	1.68 pF
$R_s$ (parasitic series resistance)	1.7 $\Omega$

#### 2.4.5.2 Experimental Results of the Nonlinear Resonance Circuit

The Duffing nonlinear resonator was fabricated and tested. The RF power is provided by a signal generator (Anritsu MG3681A), and the voltage across the varactor is monitored with a digital oscilloscope (Tektronix TDS3052B).

The influence of the available power level on the Duffing resonator's operation was also studied. The available power is varied from 0.2  $\mu$ W to 5  $\mu$ W. Figure 2.16 shows the circuit's amplitude-frequency relationship at different available power levels. The slope of the amplitude-frequency response is not obviously influenced by power level variations. Moreover, as the available power level increases, the peak of the amplitude response increases, and the jump-down point moves to higher frequencies. The observation agrees well with Figure 2.10.

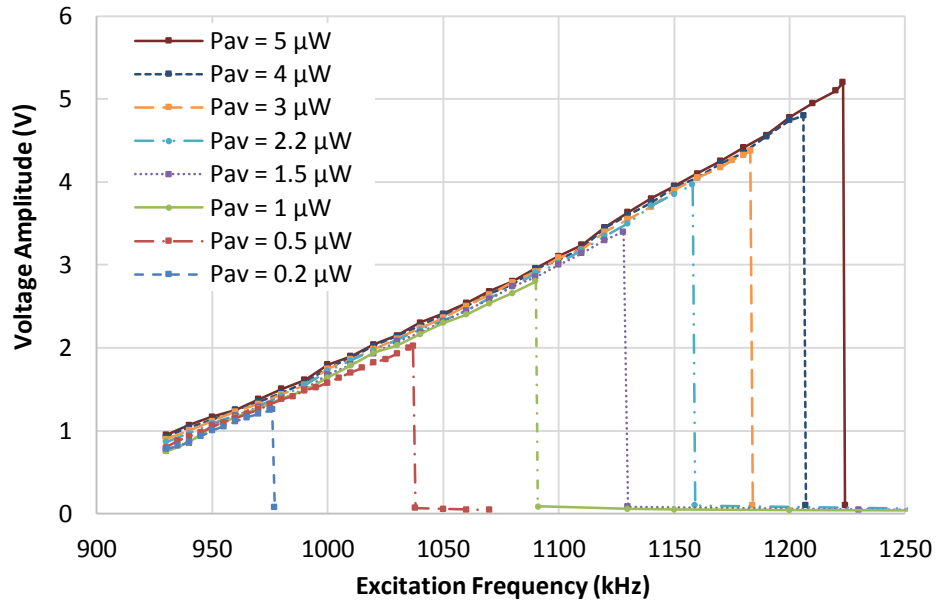


Figure 2.16. Measured voltage amplitude as functions of excitation frequencies at different available power levels from the source.

The circuit's frequency response as a function of the nonlinear resonator's loaded  $Q$  values was experimentally investigated. In this experiment, the available RF power level is  $P_{av} = 0.7 \mu W = -31.5 \text{ dBm}$ . The load resistance is varied such that the loaded  $Q$  of the resonator changes from 72 to 160. Figure 2.17 shows the circuit's amplitude-frequency relationship at different  $Q$  values. The jump-down point occurs at relatively high frequencies, and peak amplitude increases with the circuit's  $Q$ . Slopes of the curves do not exhibit obvious dependence on  $Q$ . The observation agrees with Figure 2.11. Therefore, the nonlinear resonator circuit behaves as an ideal voltage source whose output voltage is constant regardless of the load resistance.

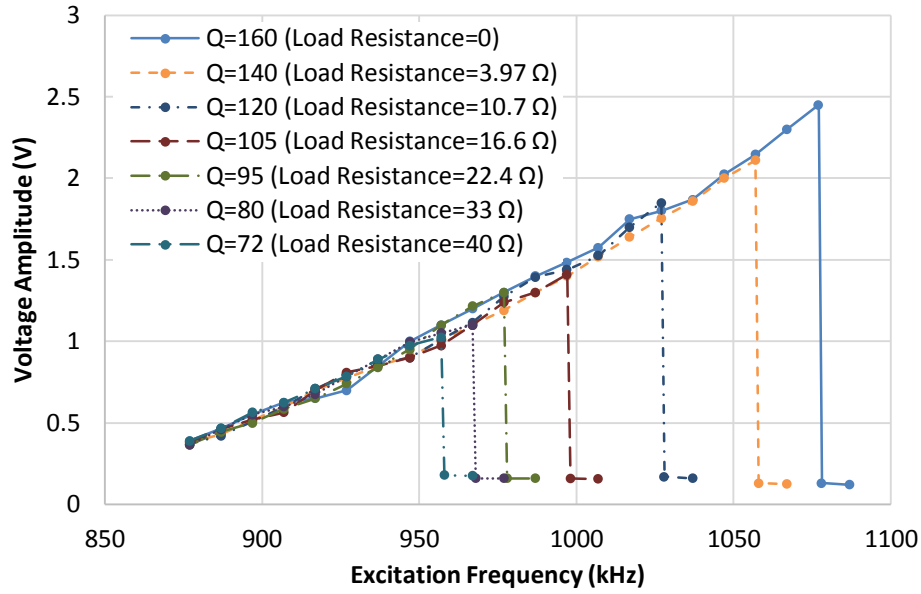


Figure 2.17. Measured voltage amplitude as functions of excitation frequencies with different loaded Q values.

## 2.5 Design of a WPT Circuit Based on Nonlinear Resonator

The Duffing resonator is used in the design of a WPT receiver to reduce the efficiency degradation due to changes in coupling factor between the primary and secondary coils.

As mentioned earlier, a SCMR WPT system reaches its peak efficiency when the primary and secondary coils are critically coupled. If the coupling factor is slightly higher (in the over-coupled region), near-maximum efficiency can still be achieved, but at two separate frequencies apart from the original operation frequency. Therefore, the point can be tracked if the natural frequency of the resonators adaptively changes with the coupling factor.

The automatic tracking of optimum operation point is achieved by Duffing resonators. Duffing resonator provides negative feedback to the WPT circuit's operation, which enhances its tolerance to coupling factor variations. Assuming that the circuit is initially tuned to be critically coupled, when the coupling factor between the two coils is increased (moving into the over-coupled region), the amplitude "A" decreases since the optimum frequency drifts away from the original operation frequency. According to (2.9), as  $A$  decreases,  $\omega_0$  is decreased. This is equivalent to maintaining a fixed natural frequency but increasing the source frequency. Therefore, the circuit effectively "tracks" the even mode frequency which increases with the coupling factor [115]. Hence, the efficiency decrease in WPT caused by the frequency split phenomenon is significantly reduced.

From another point of view, this process is in principle similar to an impedance-tuner which adaptively adjusts the circuit parameters according to the power level [116]. However, rather than tuning the component values with a complex control circuitry, the adaptive matching here is achieved through the varactor's voltage-dependent average capacitance. As the amplitude decreases in the over-coupled region, the average capacitance increases, providing effective adaptive tuning which compensates for the efficiency variations due to distance changes and misalignment.

### **2.5.1 Circuit Design and Simulation**

A two-coil WPT system based on the Duffing resonator circuit was designed at 4.5 MHz. The basic diagram is shown in Figure 2.18. Both the primary and the secondary coils implement series resonance structures. The secondary coil here utilizes a nonlinear

capacitor. The nonlinear capacitor consists of four pairs of anti-series connected varactor diodes (BBY-65 from Infineon Technologies) to provide the bell-shaped capacitance-voltage curve in Figure 2.4 (a). Both the primary and secondary coils are made of 18-gauge copper wire. The coils have 12 windings with a diameter of 10 cm, and have an inductance of 18.12  $\mu\text{H}$ . The specifications of the circuit are summarized in Table 2.3.

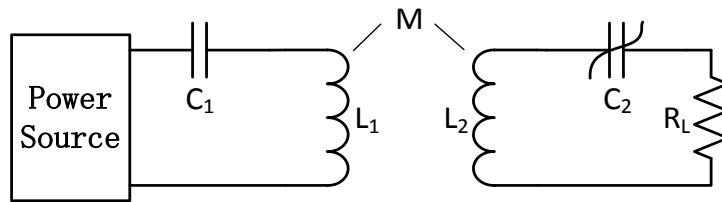


Figure 2.18. Diagram of the two-coil WPT system employing a Duffing resonator

Table 2.3. Component specifications for the WPT system design

Component	Specification
<b>Coils (<math>L_1</math> and <math>L_2</math>)</b>	
Diameter (D)	10 cm diameter
Number of Windings	12 turns
Wire Diameter	1 mm
Inductance	18.12 $\mu\text{H}$
<b>Nonlinear capacitor (<math>C_2</math>)</b>	4 pairs of anti-series varactor diodes (BBY-65)
<b>Load Resistance (<math>R_L</math>)</b>	47 $\Omega$

The circuit shown in Figure 2.18 is simulated with Agilent ADS. Figure 2.19 shows the simulated efficiency (calculated as the ratio between the power delivered to the load and the available power from the source, i.e.  $\eta = P_{out}/P_{av}$ ) as a function of normalized coupling distance (calculated as the ratio between the transfer distance and the diameter of the coils, i.e.  $d/D$ ). For comparison, a WPT circuit with conventional linear resonators with the same Q values are also simulated.

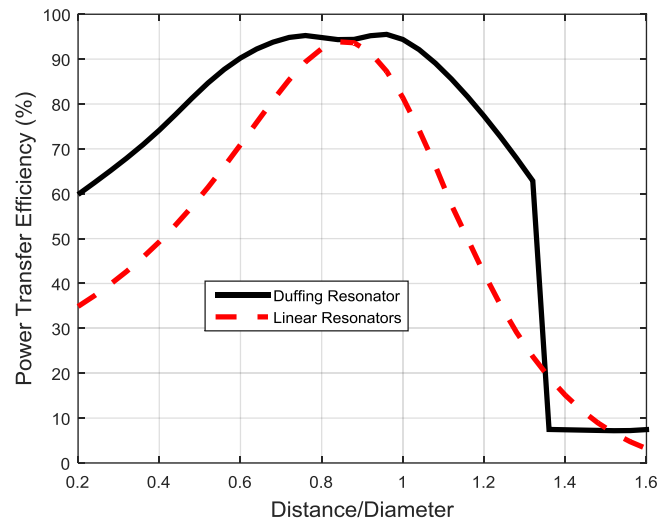


Figure 2.19. Simulated efficiency versus normalized distance ( $d/D$ ) for the WPT circuit with nonlinear resonator in the secondary coil, in comparison with the efficiency for a WPT circuit with linear resonator of the same Q value.

As shown in Figure 2.19, the maximum attainable efficiency are similar for both circuits. However, as the coupling distance moves away from the best coupling distance, the power transfer efficiency of the Duffing resonator-based WPT circuit does not decrease as rapidly as the linear resonator-based WPT system over a wide range of distances. The Duffing resonator-based WPT system can achieve efficiencies of higher than 80% when  $0.47 <$

$d/D < 1.17$ ; while the linear resonator-based WPT system achieves greater than 80% efficiency only when  $0.68 < d/D < 1$ . Therefore, the Duffing resonator significantly improves the WPT circuit's tolerance to coupling factor deviations.

## 2.5.2 Circuit Fabrication and Experimental Results

The circuit shown in Figure 2.18 was fabricated and tested. A photograph of the system is shown in Figure 2.20. In lab experiment, the source power is provided from a signal generator (Anritsu MG3681A) connected to an RF power amplifier (Cougar Components AR2569B). The available power level from the source is 16 dBm. The excitation voltage across the primary coil and the output voltage across the load are monitored with a digital oscilloscope (Tektronix TDS3052B). The output current is also monitored with a current probe (Tektronix 011-0106-00). The RF power delivered to the load ( $R_L$ ) is calculated based on its resistance and the voltage across it. The overall efficiency is measured as the ratio of output power over the available RF power from the source (defined as  $\eta = P_{out}/P_{av}$ ). For comparison, a conventional WPT link was also implemented with the same coils and was tested under the same conditions.

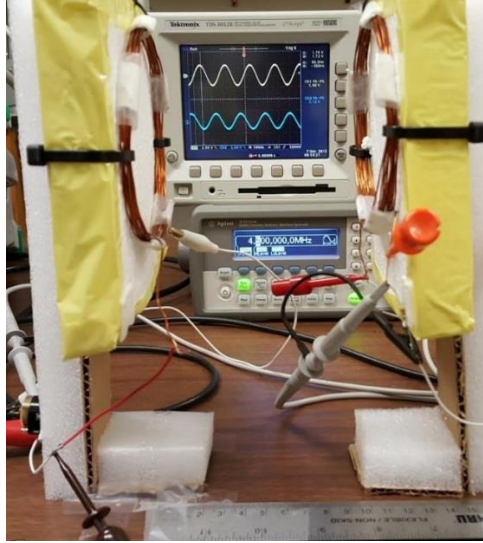


Figure 2.20. Photograph of the two-coil WPT system employing a Duffing resonator

The measured power transfer efficiencies of both the nonlinear WPT circuit and the conventional linear WPT circuit are shown in Figure 2.21 as a function of normalized coupling distance ( $d/D$ ).

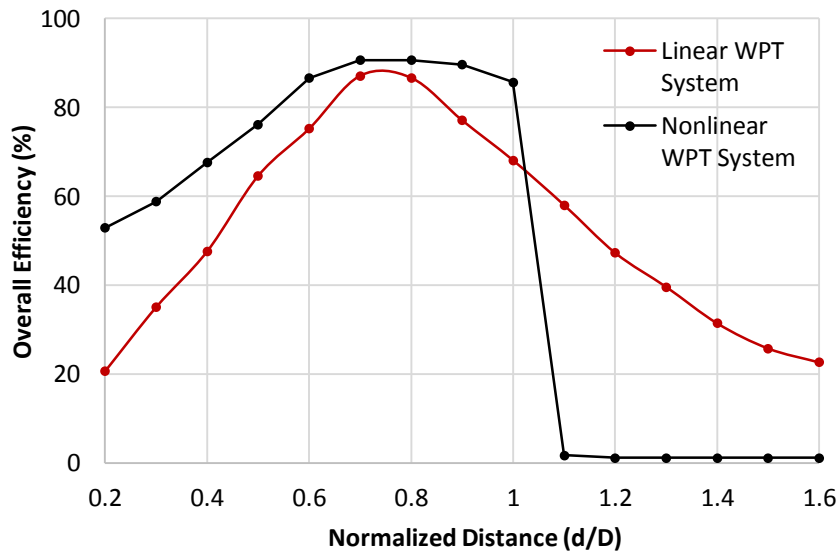


Figure 2.21. Measured transfer efficiencies (defined as  $\eta = P_{out}/P_{av}$ ) of both the nonlinear WPT circuit and the conventional linear WPT circuit as a function of normalized coupling distance to the coil diameter ( $d/D$ ).

A near-constant efficiency of higher than 80% is achieved over a wide range of coupling distances for the nonlinear circuit ( $d/D$  from 0.55 to 1), which shows significant improvement over the conventional WPT circuit ( $d/D$  from 0.65 to 0.88). In the over-coupled region, the efficiency decays at a lower rate than the linear resonator. Both circuits achieve similar peak efficiencies (90.6% for nonlinear WPT system and 87.2% for linear WPT system). The measurement results are in good agreement with simulation.

## 2.6 Conclusion

In this chapter, the development of a nonlinear resonance circuit and its application in wireless power transfer is introduced. The nonlinear resonance circuit is described by the Duffing equation, and can achieve a high resonance voltage amplitude within a wide bandwidth. Within this chapter, mathematical analysis of the Duffing resonator is also provided. The properties of such a Duffing resonator are studied through both simulation and experiment.

The Duffing resonator exhibits a significant advantage in improving the WPT system's tolerance to coupling factor variations without degrading the system's efficiency or sensitivity. Existing methods to enhance the WPT circuit's performance as coupling factor changes can be roughly categorized as either based on adaptive frequency tracking (e.g. [59]-[61]) which changes the source frequency, or adaptive impedance matching (e.g. [58], [116]) which changes the circuit parameters. Both methods have their own drawbacks. The use of adaptive frequency tuning method is usually restricted in real applications since

WPT systems can only operate within a few narrow frequency bands regulated by FCC. The adaptive impedance matching method typically relies on sensing-and-decision-making circuitries that are inevitably complex and expensive. Compared to these methods, the Duffing resonator-based WPT system realizes high efficiency within the over-coupled region with a simple passive impedance matching circuitry, and doesn't require source frequency to be altered. Therefore, it is a very promising solution in designing WPT systems that requires insensitivity to coupling factor variations.

# Chapter 3

## High Sensitivity Wireless Power Harvesters for Wireless Structural Health Monitoring Sensors

### 3.1 Introduction

Recently, the need for health condition monitoring systems for civilian infrastructures such as aging highway bridges and overpasses has been rising [117], [118]. As indicated by the Federal Highway Administration (FHWA) in 2011 [119], among the 605,086 bridges in the United States, 23.8% were listed as deficient. To maintain the functionality and safety of the existing civilian infrastructures, reliable methods for monitoring their deterioration are needed.

Among various methods for providing early warnings of structural failures, permanently installed structural health monitoring (SHM) sensors have the advantage of long-term operation and can be incorporated into a data acquisition/analysis system [117], and therefore, they have attracted much interest. Since such sensors must operate autonomously over a long period of time, how to deliver power to these sensors is a key design issue that has to be addressed. Wiring electrical power to these sensors is not practical for applications where hundreds of distributed sensors are needed [120]. If

batteries were used to provide energy for the sensors, costly periodic battery replacements would be necessary since their lifetime is much shorter than the service period of the sensors. Furthermore, the position of some sensors are not accessible for battery replacement, for example, sensors placed inside the concrete structure. Therefore, alternative approaches for powering wireless autonomous sensor networks are needed.

As mentioned in Chapter 1, wireless power harvesting technologies provides a promising solution for powering these sensors since they can capture energy from the environment and enable battery-less operation. In this chapter, a WPH receiver that captures ambient AM broadcasting signals for powering the SHM autonomous sensors is described. AM was selected as the target frequency band due to its large coverage area and low penetration loss within building materials. Such a system does not rely on line-of-sight transmission for operation.

Despite the obvious advantages of AM frequency signals, there are also certain challenges that have to be addressed. Firstly, the permitted effective radiated power (ERP) of AM stations are lower than FM or TV stations. For example, at AM bands, the broadcasting stations are restricted to operate under 50 kW in the United States. As a comparison, digital TV stations are permitted to broadcast at power levels as high as 1 MW. Secondly, due to the long wavelengths at lower frequencies, small-size AM antennas are usually inefficient. Such factors calls for the design of a high-sensitivity circuitry capable of operating under extremely low RF input power levels.

The WPH receiver described in this chapter can operate at a distance of 10 km away from a typical 50 kW AM broadcasting station. High sensitivity is achieved by optimizing the WPH receiver's antenna and rectifier, and by designing a power management unit with

very small power consumption to dictate the harvester circuit to alternate between sleep and wake-up modes. In order to provide insight into the harvester design, an analysis method that characterizes the nonlinear properties of the rectifier is also introduced. Moreover, the method of Duffing resonator circuit introduced in Chapter 2 is applied to the design of WPH receivers to improve their tolerance to frequency misalignment.

## **3.2 System Configuration**

The block diagram of the proposed WPH receiver is shown in Figure 3.1. It consists of an antenna matched to a rectifier, a boost converter, and a control circuit. The RF voltage at the antenna port is boosted by a series resonant circuit. Subsequently, the RF energy is converted to DC by the rectifier. Because of the low RF power levels in ambient environment, the rectified DC voltage is usually hundreds of millivolts, which is not sufficiently large to directly power the SHM sensors. Therefore, a boost converter is employed for voltage up-conversion. The output energy from the boost converter is stored in an energy storage element, which could be either a capacitor or a rechargeable battery. A control circuit with very low power consumption is designed to switch the boost converter between sleep and wake-up modes in order to improve the sensitivity and efficiency of the WPH receiver.

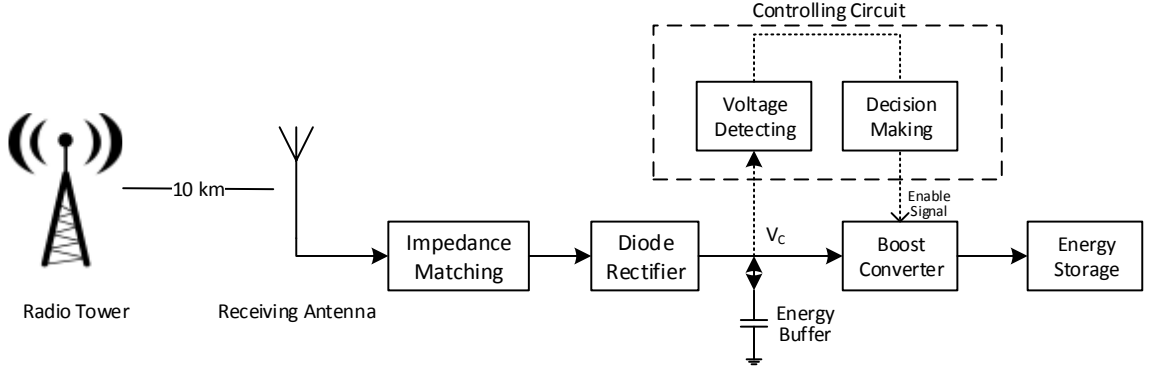


Figure 3.1. Block diagram of the medium wave wireless power harvester

### 3.3 Optimization of AM Antenna and Rectifier

Due to the long electrical wavelengths at the AM frequency band, commonly used antennas such as dipoles or monopoles are inevitably large. Ferrite coil antennas are commonly used as receiving antennas at such frequencies due to their small profile. On the other hand, the efficiency of such antennas are generally not very high. For this type of antenna, the radiation resistance  $R_r$  is expressed as (3.1):

$$R_r = 31200\mu_{rod}^2 \cdot \left(\frac{NA}{\lambda}\right)^2 \quad (3.1)$$

where  $\mu_{rod}$  is the relative permeability of the rod,  $A$  is the cross section area,  $N$  is the winding number, and  $\lambda$  is the wavelength.

The antenna loss can be calculated by summing over various loss mechanisms:

$$R_{loss} = R_{DC} + R_{AC} + R_f = (\tan \delta_{dc} + \tan \delta_{ac} + \tan \delta_f) \cdot \omega L \quad (3.2)$$

where  $R_{DC}$ ,  $R_{AC}$ ,  $R_f$  are resistances due to DC wiring, AC proximity effect, and losses in the ferrite core, respectively, while  $\tan \delta_{dc}$ ,  $\tan \delta_{ac}$  and  $\tan \delta_f$  are the corresponding loss tangents, given by (3.3) - (3.5):

$$\tan \delta_{ac} = \frac{4\rho_c l_w 10^9}{\omega A_L N n \pi d^2} \quad (3.3)$$

$$\tan \delta_{ac} = \frac{k_E f N n d^4}{A_L} \quad (3.4)$$

$$\tan \delta_f = C \quad (3.5)$$

where  $A_L$  ( $nH/turn^2$ ) is the geometry coefficient determined by measurement,  $\rho_c$  is the resistivity of the winding material,  $l_w$  is the circumference of each winding,  $n$  and  $d$  are the numbers of strands and diameter of each strand of the Litz-wire,  $k_E$  is the geometry dependent proximity effect coefficient determined by measurements, and  $C$  is a factor that is mainly dependent on the properties of the ferrite rod and is independent of  $N$ .

The antenna quality factor (Q) can therefore be determined as (3.6):

$$Q = \frac{1}{\tan \delta_{ac} + \tan \delta_{ac} + \tan \delta_f} = \frac{1}{\frac{4\rho_c l_w 10^9}{\omega A_L N n \pi d^2} + \frac{k_E f N n d^4}{A_L} + C} \quad (3.6)$$

The relationship between the antenna Q of ferrite coil antenna and its efficiency is given by (3.7) [121]:

$$\eta_{antenna} = \frac{1}{1 + \frac{2\pi v_c \cdot \mu_0 \lambda^3}{31200 \cdot Q \mu_r l_c A}} \quad (3.7)$$

Therefore, the antenna Q needs to be maximized in order to improve antenna efficiency. In this design, M400HH ferrite rods with a cross sectional area of 2.7 cm<sup>2</sup> and a length of 15 cm are used for the fabrication of antenna. The antenna Q was experimentally optimized by changing the number of windings. A plot of measured ferrite antenna Q versus the number of windings is provided in Figure 3.2. The antenna Q achieved a maximum value of approximately 108 at N=60.

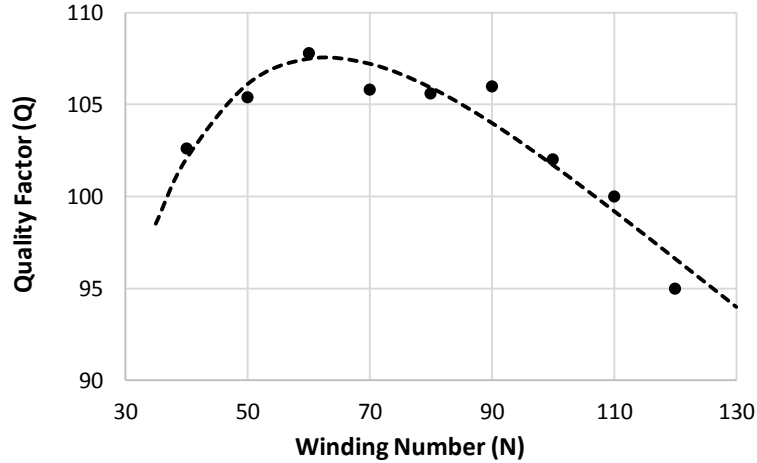


Figure 3.2. Measured Q (dots) of ferrite antenna versus the number of windings

To minimize power reflection and to improve the rectification efficiency, the antenna must be impedance matched to the rectifier. As shown in Figure 3.3, a tunable capacitor,  $C_{VAR}$ , is connected to the antenna to form a resonator. The reactance of the antenna and rectifier is cancelled out by tuning  $C_{VAR}$ , thus only the real parts of the diode and antennas impedances need to be matched. This is accomplished by using a center tapped autotransformer with a transformation ratio of  $1:n$  as shown in Figure 3.3. The Thevenin equivalent circuit for the source and transformer is expressed by a voltage source,  $nV_s$ , with a series resistance of  $n^2R_s$ , and can be matched to the rectifier by setting  $n = \sqrt{\frac{R_{rect}}{R_s}}$ , where  $R_{rect}$  is the input resistance of the rectifier. In practice,  $n$  is experimentally optimized as  $2/3$ .

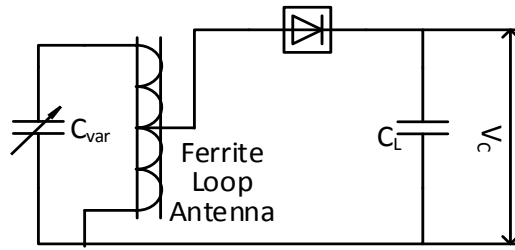


Figure 3.3. Configuration of the antenna and rectifier circuit

### 3.4 Nonlinear Analysis and Modeling of Rectifier Circuits at Low RF Power Levels

The rectifier is an important component that impacts the harvester's efficiency, especially when the input power level is low. Since the rectifier's conduction resistance and junction capacitance demonstrate strong nonlinearities under low power levels, these nonlinear properties must be carefully studied.

Previously, piecewise linear models have been widely adopted in the analysis of rectifiers in WPH receivers. Such models assume the conduction resistance to be zero (or a small fixed value) above a certain forward-bias voltage and infinite otherwise. For example, shunt-connected diode rectifiers are studied using such a model in [122], where the rectification efficiency and input impedance are calculated from the input/output voltages and diode parameters. Rectifiers with harmonic terminations are also studied with a similar approach, such as in [123]. In these studies, the piecewise approximation provides great convenience and comparatively good accuracy when the input power level is high (usually tens of  $\mu\text{W}$  or above, such that the RF voltage is significantly greater than the threshold voltage). However, such an analysis method can lead to a large inaccuracy when

the RF power level is low ( $\mu\text{W}$  level or below), since the nonlinear properties around the device's threshold voltage are not well characterized. In order to address this issue, the rectification process is studied in the time-domain by integrating the conducting current as a function of excitation voltage. For example, in [124], a numeric model is presented based on experimentally extracted I-V and C-V curves. The model shows good agreement with experimental results. However, the solution is expressed with sophisticated integral equations which can only be solved numerically by computers. Cardoso *et al.* proposed an analysis method based on the assumption that the RF signal is in a form of square wave [125]. However, the actual input signal captured by the antennas in WPH receivers is usually close to a sinusoidal wave. Considering the abovementioned issues, an accurate but mathematically simple method for analyzing the rectifier circuits operating at low RF input power levels is useful in device selection and rectifier design.

Within this section, an analysis method to derive a steady-state solution for the rectifier circuit by applying the Ritz-Galerkin (RG) method [126] is described. The RG method can derive a closed-form solution without truncating the power series expansion of the diode's nonlinear I-V equations, and therefore provides good accuracy over a wide range of input power levels.

It has been shown that a single diode (either shunt or series connected, as depicted in Figure 3.4 (a) and (b)) is most suitable for low-power rectification at microwave frequency [127]. In a WPH receiver, the antenna can be represented by its Thevenin equivalent circuit, which has a source voltage  $V_{antenna}$  and a port impedance  $Z_{antenna}$ . The general model of rectifier diodes is shown in Figure 3.5 (a), and a simplified model neglecting the parametric components is shown in Figure 3.5 (b).  $G_j$  and  $C_j$  are the voltage-dependent junction

conductance and capacitance, respectively. The voltage across the junction is denoted as  $v_j$ . In this paper, the model in Figure 3.5 (b) is used for analysis.

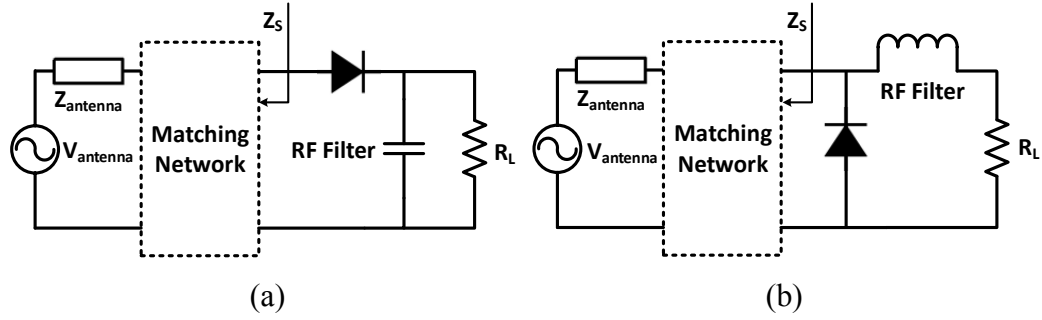


Figure 3.4. (a) Series and (b) shunt connected single diode rectifier

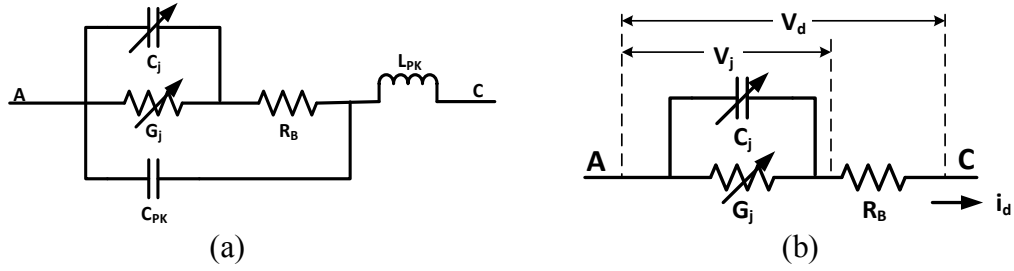


Figure 3.5. (a) Full nonlinear model and (b) de-embedded model for a PIN junction diode

For a given device, the I-V and C-V relationships are either provided by the manufacturer or measured in the lab, represented by nonlinear equations (3.8):

$$\begin{cases} i_j(v_j) = f(v_j) \\ C_j(v_j) = g(v_j) \end{cases} \quad (3.8)$$

The Shockley equation, shown in (3.9), is widely used to describe P/N diodes, Schottky diodes, and diode-connected MOSFETs in weak inversion:

$$i_j(v_j) = I_S \cdot \left( e^{\frac{v_j}{n \cdot V_T}} - 1 \right) \quad (3.9)$$

where  $I_S$  is the junction saturation current,  $n$  is the emission coefficient,  $V_T$  is the thermal voltage.

The most commonly cited expression of the junction capacitance is (3.10):

$$C_j(v_j) = \frac{C_{j0}}{\left(1 - \frac{V_j}{V_{bi}}\right)^m} \quad (3.10)$$

where  $C_{j0}$ ,  $V_{bi}$  and  $m$  are the zero-bias capacitance, built-in potential and grading coefficient, respectively.

For the diode model shown in Figure 3.5 (b), the relation between current and voltage can be written in the form of a differential equation (3.11):

$$i_d = I_S \left[ \exp\left(\frac{v_j}{n \cdot V_T}\right) - 1 \right] + \frac{d}{dt} [v_j \cdot C_j(v_j)] \quad (3.11)$$

Equation (3.11) is rearranged into the form of (3.12) to apply the RG method:

$$\xi \left[ \frac{d}{dt}, i_d, v_j \right] = I_S \left[ \exp\left(\frac{v_j}{n \cdot V_T}\right) - 1 \right] + \frac{d}{dt} [v_j \cdot C_j(v_j)] - i_d \quad (3.12)$$

where  $\xi$  is a nonlinear operator. RG method approximates the solution of (3.12) with the following series:

$$\tilde{i}_d(t) = \sum_{k=1}^N a_k \psi_k(t) \quad (3.13)$$

where  $\psi_k(t)$  are linear independent eigenfunctions and  $a_k$  are the coefficients to be determined. The residue

$$\epsilon(t) = \xi \left[ \frac{d}{dt}, \tilde{i}_d, v_j \right] \quad (3.14)$$

is minimized when the  $N$  Ritz conditions are satisfied:

$$\int_{t_1}^{t_2} \xi \left[ \frac{d}{dt}, \tilde{i}_d, v_j \right] \psi_k(t) dt = 0 \quad k = 1, \dots, N \quad (3.15)$$

resulting in  $N$  equations and  $N$  unknowns ( $a_k$ ).

In this analysis, the RF filter (shown in Figure 3.4) is assumed to be ideal, such that the output voltage has no RF component. Therefore,  $v_j$  can be written as

$$v_j = -V_{j0} + V_{j1} \cos(\omega t) \quad (3.16)$$

where  $V_{j1}$  is the amplitude of RF voltage applied to the rectifier and  $V_{j0}$  is the DC output voltage. Trigonometric functions can be used as eigenfunctions in  $\tilde{v}_d$ . The most important terms in the analysis are the DC component and the fundamental terms. Therefore, only the terms shown in (3.17) are taken in to account in the approximate solution:

$$\tilde{v}_d = I_{dc} + I_{1r} \cos \omega t + I_{1i} \sin \omega t \quad (3.17)$$

Using (3.16)-(3.17) in (3.15),  $I_{dc}$ ,  $I_{1r}$  and  $I_{1i}$  can be represented as:

$$\begin{cases} I_{dc} = I_S \cdot \left( e^{-\frac{V_{j0}}{n \cdot V_T}} \cdot I_0 \left( \frac{V_{j1}}{n \cdot V_T} \right) - 1 \right) \\ I_{1r} = 2 \cdot I_S \cdot e^{-\frac{V_{j0}}{n \cdot V_T}} \cdot I_1 \left( \frac{V_{j1}}{n \cdot V_T} \right) \\ I_{1i} = \frac{\omega}{\pi} \int_0^{2\pi} \frac{d(C_j V_j)}{dx} \cdot \sin x \cdot dx \end{cases} \quad (3.18)$$

where  $I_0$  and  $I_1$  are the modified Bessel function of the first kind [128]. Therefore, (3.18) describes the output current assuming the input and output voltages are known.

It worth mentioning that the junction capacitance doesn't contribute to the rectification process. The only influence of the capacitance is that it causes a bypass AC current ( $I_{1i}$ ) which flows through  $R_B$  and causes loss.

Equation (3.18) allows the optimum impedance matching network and the attainable output power to be predicted with good accuracy. Since the reflected power at fundamental frequency is zero when the rectifier is perfectly matched to the antenna, the following equations can be written:

$$\begin{cases} \left( \frac{V_{j0}}{I_S(R_B + R_L)} + 1 \right) e^{\frac{V_{j0}}{n \cdot V_T}} = I_0 \left( \frac{V_{j1}}{n \cdot V_T} \right) \\ P_{av} = V_{j1} \cdot I_S \cdot e^{-\frac{V_{j0}}{n \cdot V_T}} \cdot I_1 \left( \frac{V_{j1}}{n \cdot V_T} \right) \end{cases} \quad (3.19)$$

$V_{j0}$  and  $V_{j1}$  can be conveniently solved from (3.19), and then the input impedance, output power and rectification efficiency of the rectifier can be expressed as

$$Z_{in} = \frac{V_{j1}}{I_{1r} + j \cdot I_{1i}} + R_B \quad (3.20)$$

$$P_{dc} = (V_{j0} - I_{dc}R_B) \cdot I_{dc} \quad (3.21)$$

$$\eta_{rect} = \frac{(V_{j0} - I_{dc}R_B) \cdot I_{dc}}{0.5 (V_{j1} \cdot I_{1r} + (I_{1r}^2 + I_{1i}^2)R_B)} \quad (3.22)$$

One corollary of the nonlinear resistive maximum power theorem proposed by J. Wyatt *et al.* [129] in 1983 indicates that impedance matching condition for achieving maximum power transmission for linear networks,  $Z_S = Z_{in}^*$ , can be also applied to nonlinear conditions involving a fixed load and a strictly increasing source I-V character. Therefore, the optimum impedance matching network would transform the antenna impedance to a port impedance of  $Z_{in}^*$ .

The analysis method is verified with simulation and experiment. A shunt-connected single diode rectifier for a 900 MHz wireless power harvester was designed, fabricated and measured. A low-threshold Schottky diode (HSMS-2852 from Avago Technologies, with parameters listed in Table 3.1) was used as the rectifying device. The circuit is fabricated with RO5880 low-loss substrate from Rogers Corporation. The circuit is shown in Figure 3.6.

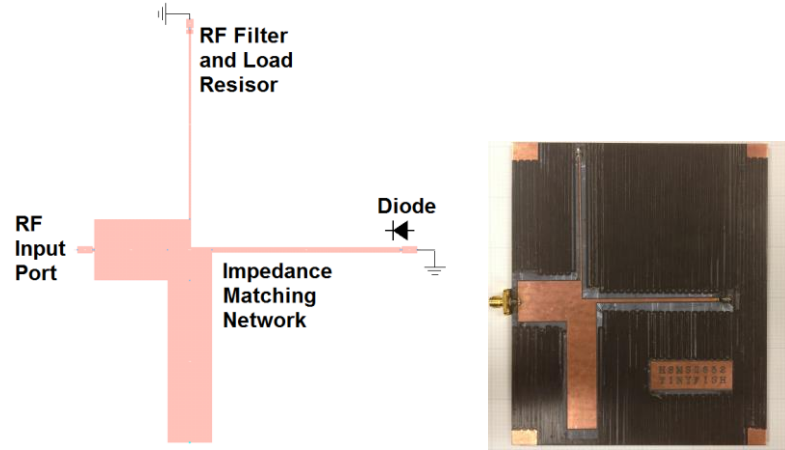


Figure 3.6. Shunt-connected diode rectifier with HSMS 2852 Schottky diode for a 900 MHz wireless power harvester

Table 3.1. Diode Parameters for HSMS2852

Symbol	Name	Value
$R_B$	Series Ohmic Resistance	25 $\Omega$
$I_S$	Saturation Current	$3 \times 10^{-6}$ A
$n$	Emission Coefficient	1.06
$C_{j0}$	Zero-bias Junction Capacitance	0.18 pF
$V_{bi}$	Built-in Junction Potential	0.35 V
$m$	Grading Coefficient	0.5

The circuit was connected to a HP-778D dual directional coupler allowing incident and reflected power to be monitored simultaneously. A HP-83640B signal generator was used for generating the RF signal, and two HP-70820A microwave transition analyzers were used for monitoring the incident and reflected power. The circuit was examined for rectification efficiency under different input power levels with a fixed load resistance  $R_L =$

3 kΩ. The comparison between theoretical and experimental results is shown in Figure 3.7. The presented analysis is also compared against the result derived from a typical piecewise-linear diode model [121] as depicted in Figure 3.7. The presented analysis exhibits good agreement with measurement results within a power range of 30 dB (from -40 to -10 dBm); on the contrary, the piecewise linear model shows good accuracy only when the diode is operating close to its peak efficiency point. The presented analysis is superior to the piecewise linear model when the input power level is low (below -10 dBm), which is the most common operating region for harvesters.

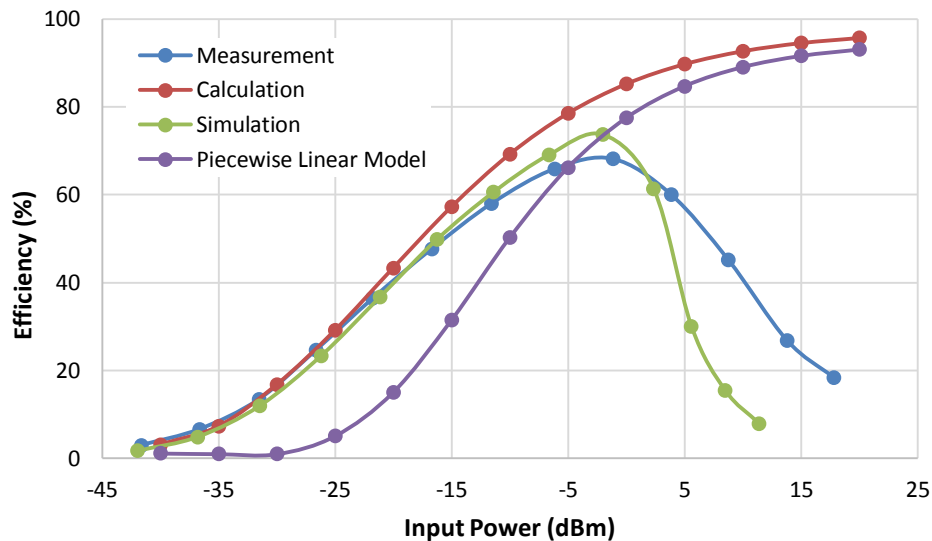


Figure 3.7. Rectification efficiency versus input power at 900 MHz for  $R_L = 3 k\Omega$ . Results generated from the proposed analysis, the conventional piecewise linear analysis, ADS Harmonic simulation, and experiment were plotted against various input power.

The discrepancy between the described analysis method and measurement results increases with the input power level, because substrate loss and leakage current are not taken into account in the described analysis method. For example, the analysis doesn't

reflect the efficiency drop when  $P_{in} > -3 \text{ dBm}$ , which is caused by the quick increase of leakage current when the reverse voltage across the diode is close to its break-down voltage. The issue can be resolved by adopting a more sophisticated diode model and taking the substrate loss into account at the cost of higher complexity.

Figure 3.8 compares the optimum impedance predicted by the model against the values optimized by a source pull method in various  $P_{in}$  and  $R_L$  cases for a shunt-connected rectifying circuit built with HSMS2852 Schottky diode. The optimum input impedance varies with both input power and load resistance, and the theoretical analysis shows good agreement with simulation in these cases.

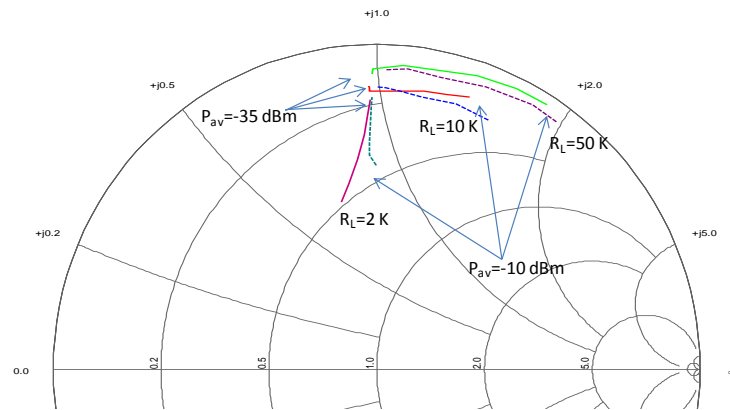


Figure 3.8. Optimum impedance matching condition versus input power at 900 MHz for  $R_L = 2 \text{ k}\Omega$ ,  $10 \text{ k}\Omega$  and  $50 \text{ k}\Omega$ . Solid curves show the calculated values, and dashed curves show the values optimized with Agilent ADS software. Smith Chart is normalized to  $Z_0 = 1 \text{ k}\Omega$  for the convenience of plotting.

## 3.5 Design and Optimization of the Power Management Unit

### 3.5.1 DC-DC Voltage Converter

Typically, the DC output voltage of the rectifier in the WPH receiver is less than a few hundred millivolts. Compared to other methods of up-conversion such as charge pumps and voltage multipliers, boost converters have the advantage of providing high energy conversion efficiency while requiring a relatively low input voltage. In this application, a boost converter with approximately 60% conversion efficiency is developed.

Figure 3.9 shows the power management unit design which includes a boost converter controlled by a Schmitt-trigger-based control circuit. The boost converter is shown with the dashed box in Figure 3.9. In the boost converter, a MOSFET (Si1563EDH from Vishay Siliconix) acts as a switch (shown as “S” in Figure 3.9) driven by a switch signal. A high frequency oscillator (LTC6906 low power oscillator from Linear Technology) is used for driving the MOSFET to switch between on and off states. During the on-state,  $V_C$  drives the inductor  $L$  and causes an increase in current  $I_L$ . During the off-state, since the inductor can prevent  $I_L$  from changing instantly,  $I_L$  will flow through the load, and the energy accumulated during the on-state will be transferred into the capacitor. The measured conversion efficiency versus input voltage is shown in Figure 3.10. The boost converter in this work provides a measured conversion efficiency of 50%~60% with input voltages ranging from 0.08 V to 0.2 V. The conversion efficiency measured here considers the power consumption of the HF oscillator for switch signal generation.

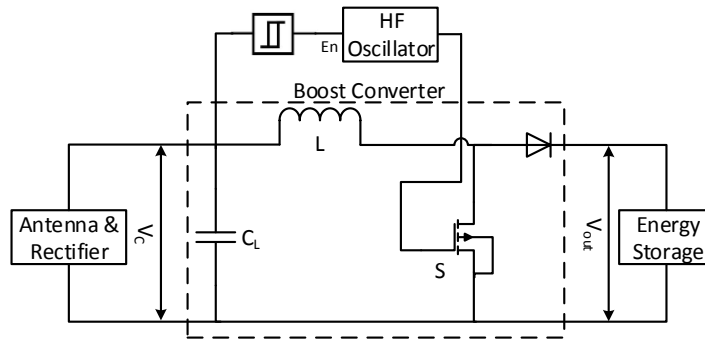


Figure 3.9. Topology of the power management unit, with dashed box showing the boost converter.

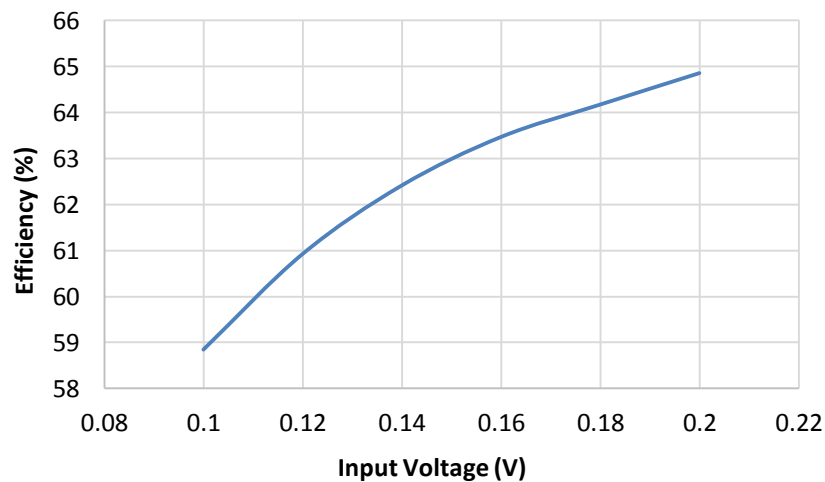


Figure 3.10. Measured efficiency of the boost converter versus input voltage

### 3.5.2 Schmitt-Trigger-Based Control Circuit

To enhance the sensitivity and overall efficiency of the WPH receiver, a control circuit is employed to dictate the boost converter to alternate between sleep and wakeup status. The boost converter sleeps for most of the time, and wakes up for short periods of time to convert energy from  $C_L$  to the output energy storage element (shown in Figure 3.9). There

are two main purposes for utilizing the control circuit. Firstly, the HF oscillator that drives the boost converter consumes a considerable amount of power. By activating the boost converter for only short periods of time, the energy consumption of the boost converter can be reduced significantly, thus improving the overall efficiency. Secondly, conversion efficiency of the boost converter increases with the input power level. By accumulating energy in  $C_L$  over a long period of time, and then releasing it over a short period, the transient power at the input port of the boost converter can be increased significantly, therefore improving the up-conversion efficiency.

To achieve discontinuous operation of the boost converter, Paing *et al.* [91] proposed the approach of operating the boost converter as an open-loop resistor emulator, where an HF oscillator driving the converter is powered by a LF oscillator. However, the LF oscillator consumes  $\mu\text{W}$ -level power to operate. Since the control unit is the only part which consumes power continuously, reducing its power consumption is critical for improving the sensitivity of the WPH receiver. In this work, a Schmitt-trigger-based circuit is employed as the sensing and decision making controller.

The schematic of the Schmitt-trigger-based control circuit is shown in Figure 3.11. During the sleep period, RF energy captured by the antenna is converted to DC, charging the capacitor  $C_L$  and generates a DC voltage  $V_C$  across  $C_L$ . As  $V_C$  rises above a pre-set value (denoted as  $V_{high}$ ), the control circuit activates the boost converter. Upon activation,  $V_C$  drops until it reaches a lower pre-set reference voltage (denoted as  $V_{low}$ ), when the reset circuit deactivates the boost converter. The dashed box in Figure 3.11 marks the voltage detector formed by multiple stages of MOSFETs. The resistors outside the dashed box form a positive feedback network. The voltage detector has a triggering voltage of 0.2 V, which

is determined by the conducting current under MOSFET sub-threshold condition and the drain resistors. The two pre-set reference voltages,  $V_{high}$  and  $V_{low}$ , can be tuned by changing the relative values of feedback resistances. The Schmitt-trigger-based controller can achieve extremely low power consumption. In laboratory measurement, the power consumption of the control circuit is estimated to be approximately 40 nW.

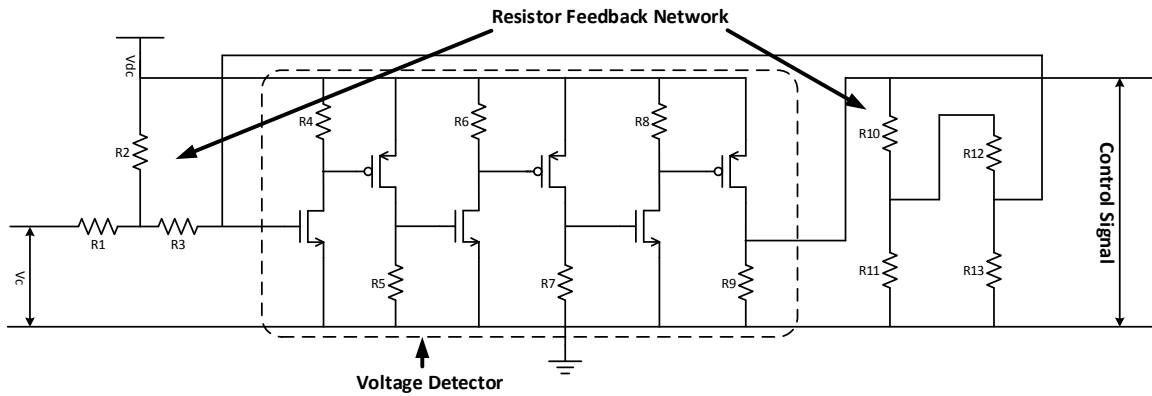


Figure 3.11. Schematic of the Schmitt Trigger Circuit, dashed box shows the voltage detector, the resistors outside the box provide positive feedback.

### 3.6 Circuit Implementation and Measurement Results

The WPH receiver circuit has been fabricated as shown in Figure 3.12. The antenna is made with M400HH ferrite rod and 15-strand Litz wire. The circuit is fabricated and sealed with a packing box.

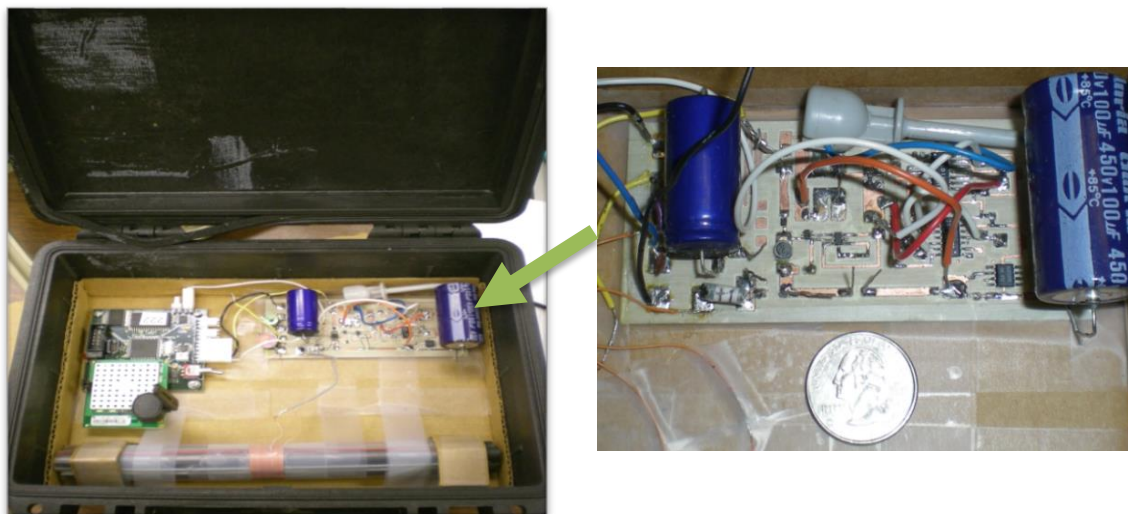


Figure 3.12. Photograph of the medium wave energy harvesting circuit.

The circuit is tested in both laboratory and field environments. A high-speed oscilloscope (Agilent MSO9404A) was used for monitoring the input and output voltages and current waveforms. A plot of voltage  $V_C$ , the control signal and the voltage  $V_{out}$  as a function of time is shown in Figure 3.13. The values of  $V_{high}$  and  $V_{low}$  are set to 0.2 V and 0.08 V, respectively. The voltage  $V_C$  keeps rising until it reaches 0.2 V when the control signal turns from low to high, activating the boost converter. Subsequently, voltage  $V_C$  drops quickly. When  $V_C$  reaches 0.08 V, the boost converter is turned off. Meanwhile, the voltage on the energy storage element  $V_{out}$  increases during the boost converter's operation as energy is transferred. The control circuit is powered by the energy stored in the output storage element, which can be a capacitor or a rechargeable battery. As the WPH receiver captures RF energy, charge on the storage element is replenished. If capacitors were to be used as storage element, it should be charged prior to its insertion into the circuit in order to provide the initial energy for the control circuit's operation.

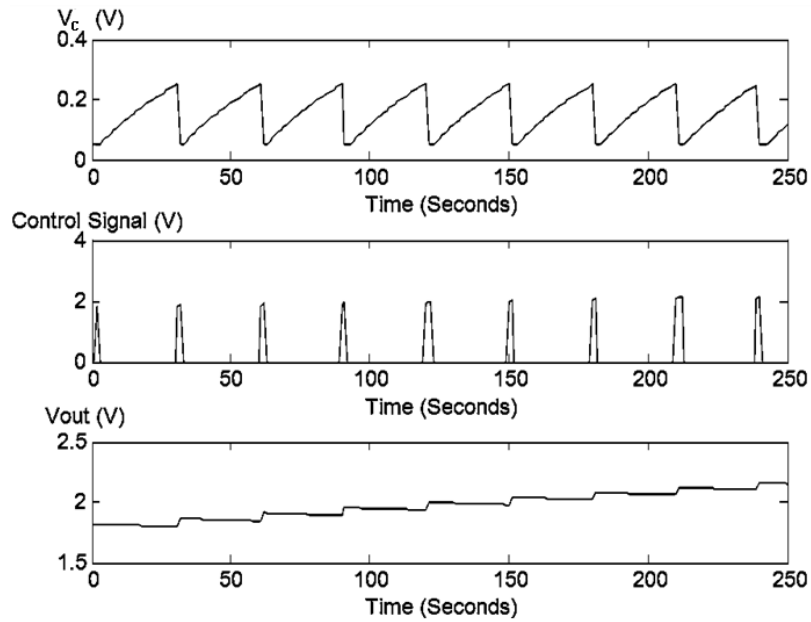


Figure 3.13. Waveform of  $V_c$  and  $V_{out}$  of the boost converter and the control signal given by the Schmitt trigger circuit. The reference voltages of the Schmitt trigger circuit,  $V_{high}$  and  $V_{low}$ , were set to 0.2 V and 0.08 V respectively.

The overall efficiency of the WPH receiver, taking into account all the losses such as the RF-DC rectification loss, the DC-DC conversion loss, the power consumed by the control circuit and the leakage of the energy storage capacitors, has been measured at different input RF input power levels. The results are shown in Figure 3.14. As can be seen, at very low input levels ( $< 2 \mu\text{W}$ ), the overall efficiency is almost zero. This is because the power captured by the WPH receiver is so small that the voltage change on the output capacitor is below the sensitivity of the measurement equipment, thus can hardly be observed. As the input power is increased, the overall efficiency rapidly increases to 28% at  $23 \mu\text{W}$  input power.

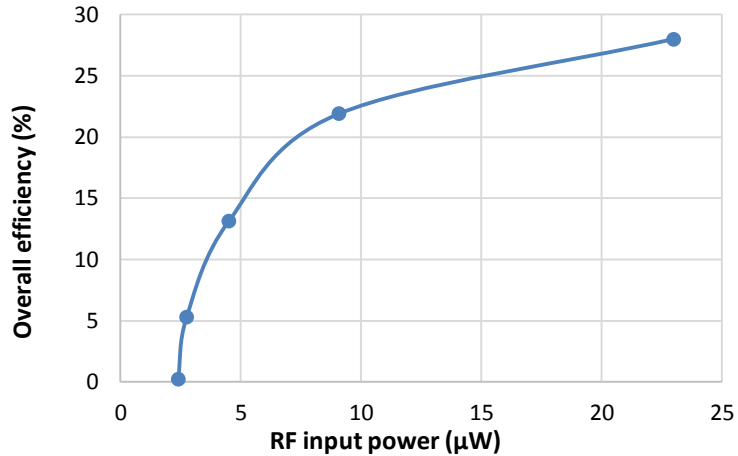


Figure 3.14. The overall RF-DC efficiency vs. RF input power levels of the WPH receiver

The WPH receiver was tested around a 50 kW, 1.27 MHz AM station (WXYT) located near Detroit, Michigan, USA. The harvester was sealed in a waterproof box and installed on the side of a highway bridge (Telegraph Bridge). Figure 3.15 is a picture of the harvester during field test, showing the position where it is installed. Figure 3.16 shows the scavenged power level versus the distance from the transmitter antenna. More than 0.5  $\mu\text{W}$  average DC power can be generated within 3 km from the station. Due to the directional properties of the ferrite rod antenna, some alignment is needed in order for the maximum power harvesting. However, because of the low directivity of such antennas, the alignment is a relatively easy task by changing the direction of the rod while monitoring the RF voltage generated from the antenna.



Figure 3.15. The harvester being tested on a highway bridge in Detroit, Michigan

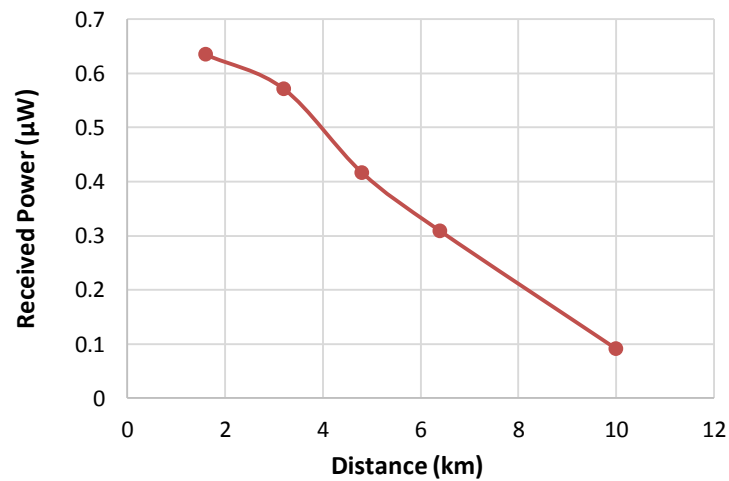


Figure 3.16. Received power versus distance to a local AM broadcasting station (WXYT)

It also worth mentioning that the scavenged power does not strictly follow a  $1/R^2$  relationship with distance which would be predicted by electromagnetic field theory. The major reason for this phenomenon is that the impedance matching condition between the antenna and the rectifier depends on the incident power level. Thus, the required matching

condition changes with input power level. In this work, to achieve the best sensitivity, the impedance matching was optimized at very low power levels

### **3.7 WPH System Design Based on Duffing Resonator for Improving the Tolerance to Frequency Misalignment**

The Duffing resonator circuit introduced in Chapter 2 is applied to the design of WPH systems for improving their tolerance to frequency misalignment which is usually caused by component aging, coupling to surrounding objects, environmental factor change such as humidity and temperature, and etc.

#### **3.7.1 Circuit Design**

The Duffing resonator circuit is used in the WPH receiver to replace the linear resonator circuit described in Section 3.3. The schematic for the circuit is shown in Figure 3.17. The circuit uses the same antenna and rectifier design; however, the capacitance is provided by four pairs of anti-series connected varactor diodes (SMV1249 from Skyworks, the parameters of which is given in Table 2.2 in Section 2.4) in shunt with a small trimmer capacitor. A small trimmer capacitor  $C_{var}$  is connected in parallel with the varactor diodes for fine tuning of the circuit.  $C_{var}$  is small as compared to the varactor capacitance, and therefore has minimal influence of the circuit operation. Similar to the circuit shown in Figure 3.3, the impedance matching is achieved by changing the position of the center tap of the antenna winding. The specifications of the circuit is given in Table 3.2. The circuit is fabricated. A picture of the circuit is shown in Figure 3.18.

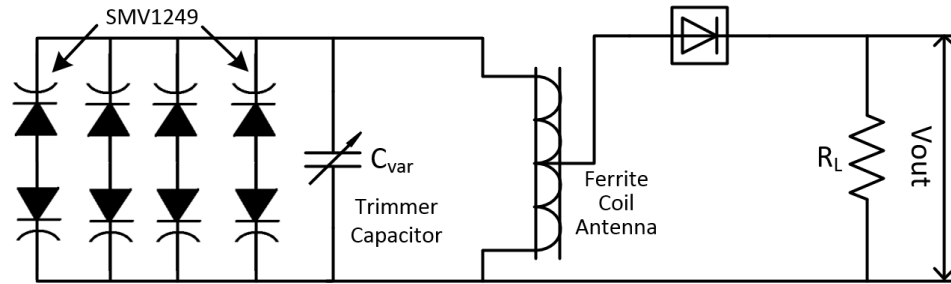


Figure 3.17. Circuit of the 1 MHz WPH receiver employing a Duffing resonator



Figure 3.18. Photograph of the 1 MHz WPH circuit (excluding boost converter and control circuit) employing a Duffing resonator

Table 3.2. Component specifications for the WPH system design

Component	Specification
<b>Ferrite Coil Antenna</b>	
Coil material	M400HH (3 coils)
Coil cross section	2.7 cm <sup>2</sup>
Coil length	15 cm
Number of Windings	60 turns
<b>Nonlinear capacitor</b>	4 pairs of anti-series varactor diodes (SMV1249)
<b>Rectifier</b>	1N34A

### 3.7.2 Simulation and Measurement Results

The circuit is studied through both simulation and experiment. The measurement setup is shown in Figure 3.19. In the lab measurement, a 30-cm-diameter 5-turn coil antenna connected to a signal generator (Agilent 33220A) is used to generate the ambient EM field. The harvester is positioned at 1 m away from the antenna. For comparison, a harvester using a linear resonator with the same quality factor is also tested under the same conditions.

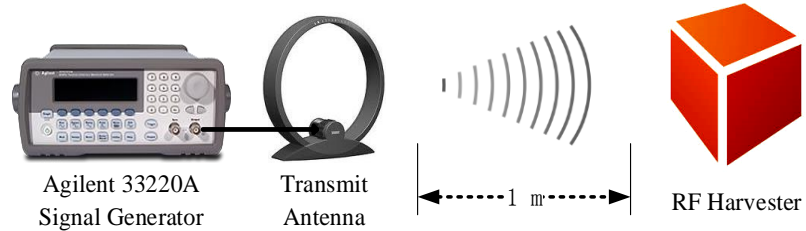


Figure 3.19. Measurement Setup

The frequency response of the nonlinear resonance circuit described above is measured to evaluate its bandwidth enhancement capability. First the frequency response of the nonlinear resonator was measured. The available power level at the ferrite rod antenna port is  $P_{av} = 0.7 \mu\text{W} = -31.5 \text{ dBm}$ . Figure 3.20 (a) shows the simulated and measured amplitude resonance as a function of frequency for the Duffing resonator when it is not connected to a load, and Figure 3.20 (b) shows the resonator's response when it is connected to a matched load ( $R_L = R_S = 33 \Omega$ ). A harvester employing a linear resonance circuit with the same  $Q$  is also tested under the same condition. The measurement results are also shown in Figure 3.20 (a) for comparison.

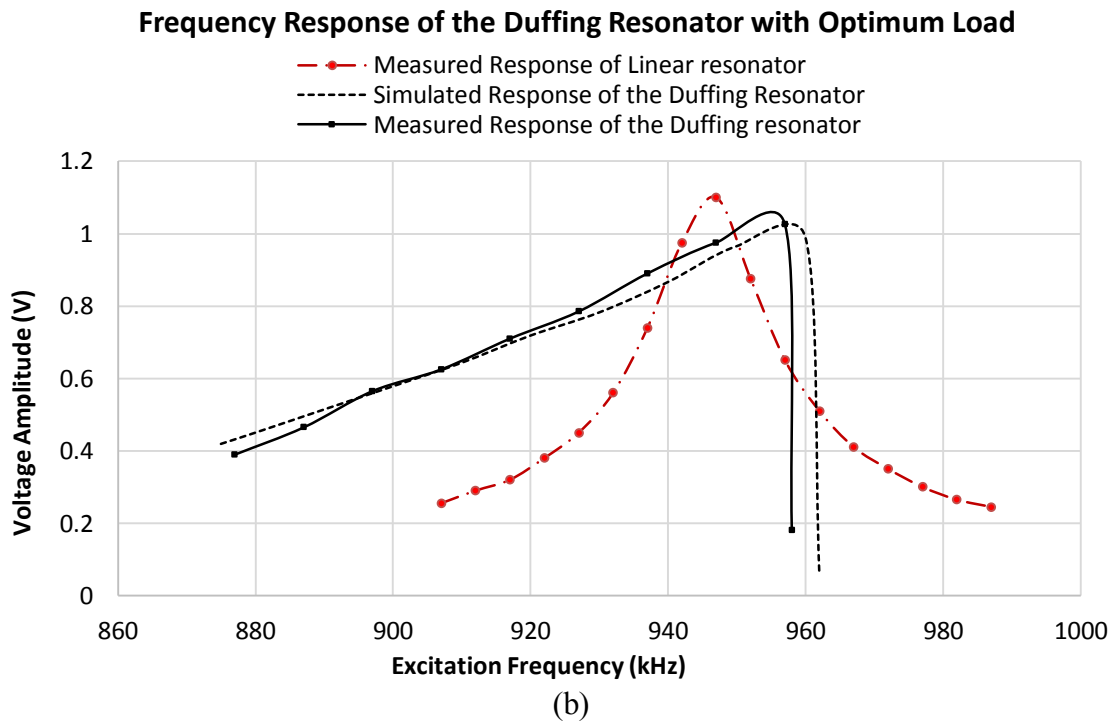
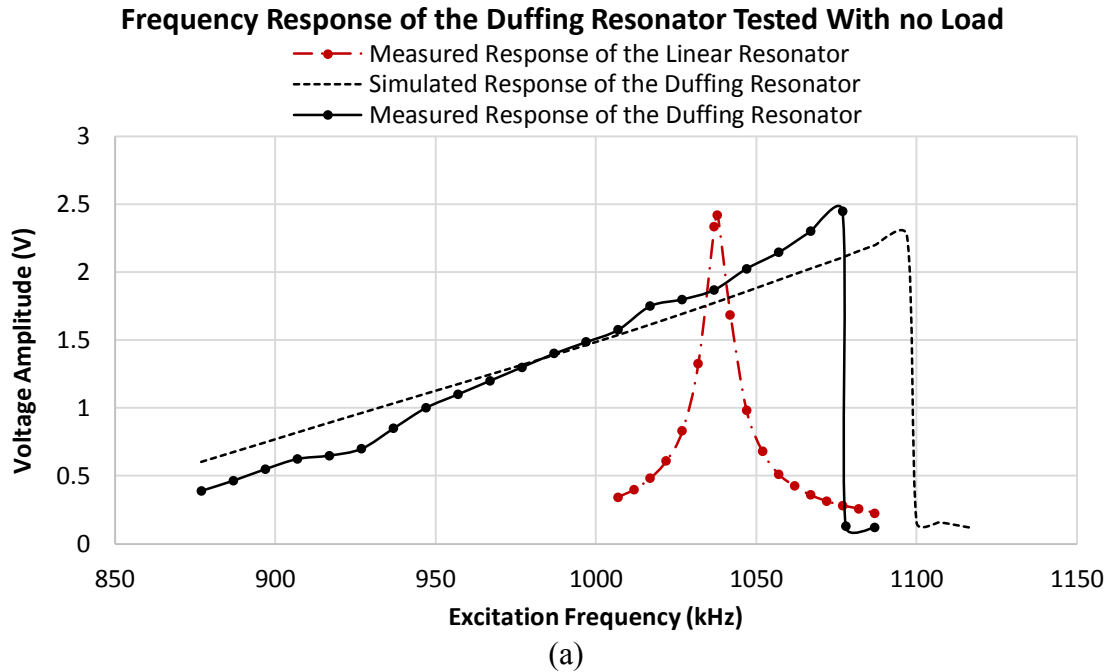


Figure 3.20. Comparison between the voltage amplitude response of a Duffing resonator based EM harvester and a linear resonator based EM harvester. (a) The simulation and measurement results for the Duffing resonator in comparison with the linear resonator without a load, and (b) the simulation and measurement results for the Duffing resonator in comparison with the linear resonator, when both circuits are connected to matched loads ( $R_L = R_S = 33 \Omega$ ).

It can be observed that the Duffing resonator circuit achieves a significant bandwidth enhancement as compared to the linear resonator. When the circuit is connected to a matched load (Fig. 3.20 (b)), the jump down point shifts to lower frequencies since the circuit Q decreases (the influence of circuit Q on the Duffing resonator's voltage amplitude response will be further discussed in Part D). In this case the three-root region is smaller as compared to the unloaded circuit (Fig. 3.20 (a)). However, as shown in Fig. 3.20 (b), still a substantial bandwidth enhancement can be achieved. At the same time, the Duffing resonator can provide a similar peak power level. There is a slight difference in the slope of the curves and the jump down frequencies between the simulation and measurement results. This is mainly attributed to the fact that the nonlinear C-V response of the varactors is approximated by a 3<sup>rd</sup>-order polynomial (Eq. 2.5), and the fact that circuit component values are not exact.

Figure 3.21 shows the output power of the Duffing circuit as function of frequency, in comparison with the output power of a linear resonator. Both circuits are connected to optimum loads. The bandwidth here is defined as the frequency range where the output power is half of its maximum value. It can be seen that the bandwidth of the Duffing resonator is larger by a factor of 2.7 (915-962 kHz) as compared to the linear resonator's bandwidth (938-955 kHz). Consequently, the Duffing resonator is much less sensitive to frequency misalignment as compared to a linear resonator. Therefore, the effect of frequency detuning due to component aging, environmental variations and coupling to surrounding objects on power transfer efficiency is reduced. It should be noted that the maximum output power for the linear and the Duffing resonator circuits are similar and are

close to the maximum available source power. This is due to the fact that varactor loss is negligible as compared to other losses in the circuit.

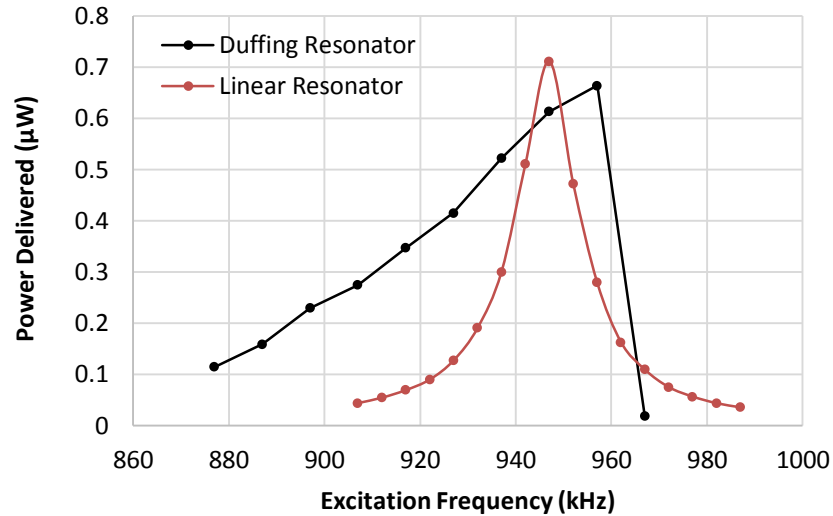


Figure 3.21. Measured output power of a Duffing resonator in comparison with a linear LC resonator. Both circuits are optimally loaded (equivalent load resistance matches to  $R_S$ ). Power available from the source is  $0.7 \mu\text{W}$  for both cases.

### 3.7.3 Discussion on the Circuit's Operation

As mentioned before, since the Duffing resonator-based WPH receivers have much wider bandwidth as compared to conventional WPH receivers, their performance is not strongly dependent on frequency misalignment. This section provides discussions on a few practical issues of such WPH systems that need to be noted.

The peak of voltage amplitude response for the nonlinear resonator occurs at the jump down frequency (Fig. 3.20). Therefore, in order to deliver the maximum power, the circuit should be designed such that the jump down frequency is as close to the source frequency as possible. However, according to the available data, when selecting the operation point,

a safety margin is needed in order to ensure that the operation point is not too close to the jump down point. As is illustrated in Section 2.4.4 and Section 2.4.5, the available input power variation shifts the jump down frequency. Therefore, the operation frequency of the nonlinear resonance circuit should be selected away from the jump down point.

Secondly, a start-up circuit would be necessary to ensure the circuit converges to the upper equilibrium points. As mentioned before, there are two stable solutions for a Duffing resonator circuit. It is desirable to operate on the upper equilibrium points. A start-up circuit can be designed to provide a strong initial excitation signal to the Duffing resonator to force the circuit to converge to the upper solution. The start-up circuit can be designed to operate in a sleep and wake up mode to reduce its power consumption.

### **3.8 Conclusion**

In this chapter, a wireless power harvester working at AM frequency band for autonomous structural health monitoring sensors is demonstrated. The antenna and rectifier are designed based on theoretical analysis and experimental optimization. A Schmitt-trigger-based control circuit with low power consumption is designed to improve circuit's efficiency and sensitivity. In the field test, the wireless power harvester has demonstrated the capability of providing net power at a distance of 10 km away from a 50 kW AM broadcasting station.

Table 3.3 lists the performance comparison of the described WPH receiver with a few existing publications.

Table 3.3. Comparison of RF Energy Harvesters

<b>Project &amp; published year</b>	<b>Energy Source</b>	<b>Scavenging distance</b>	<b>Load</b>	<b>Process</b>
Hargerty [8], 2004	2-18 GHz; single-tone and multi-tone	50 m	NA	PCB
Intel Research Seattle [9], 2009	960 kW TV station @ 674-680 MHz	4.1 km	Temp Sensor	PCB
Dolgov [10], 2010	Cellular tower; 1.96 GHz	50 m	Battery	PCB
Parkers [11], 2013	1 MW TV station @ 539 MHz; Cellular tower @ 738 MHz	10.4 km from the TV station or 200 m from the cellular tower	Capacitor	PCB
Vyas [7], 2013	48 kW Digital TV station @ 512-566 MHz	6.3 km	16-bit PIC MCU	PCB
This work	50 kW AM station @ 1.27 MHz	10 km	Capacitor	PCB

# **Chapter 4**

## **A Wide Dynamic Range Rectifier Network with Adaptive Power Distribution Method for WPT and WPH Applications**

### **4.1 Introduction**

This chapter describes the design of a wide dynamic range rectifier circuit based on an adaptive power distribution method. The rectifier is intended for WPT and WPH applications where the RF power level is subject to fluctuation. The rectifier network consists of several rectifier cells optimized at different power levels, as well as a passive power distribution network consisting of inductors, capacitors and transmission lines. The power distribution network is able to distribute RF power among several rectifier cells according to their relative impedance values at various input power levels. As a result, at lower RF power levels, a major portion of the RF power is directed to the rectifier optimized for low power operation; while at higher RF power levels, a large portion of the RF power is directed to the rectifier optimized for high power operation.

Consequently, the RF power is always rectified by the most suitable rectifier regardless of the fluctuation of input power level. Such a technique provides two benefits. First, a high rectification efficiency is maintained over a wide range of input power levels. Second, the impedance variation of the entire rectifier circuit as a function of RF power level is reduced, such that the reflection coefficient is minimized regardless of the large variation in individual rectifier impedances. Following this approach, the dynamic range of the rectifier circuit is significantly enhanced. The described method is implemented with passive components with a relatively simple circuit topology. Furthermore, this approach can benefit a wider range of applications that needs rectification of fluctuating input power, such as power sensing and measurement devices.

## 4.2 Operation Theory and Design Methodology for a Wide Dynamic Range Rectifier Network

### 4.2.1 Diode Properties

As mentioned before in Chapter 1, the conversion efficiency of rectifiers is defined as the DC output power over the available RF power, and is influenced by both the device rectification efficiency ( $\eta_{rect}$ ), as well as the rectifier impedance matching, as described in equation (4.1).

$$\eta_{RF-DC} \triangleq \frac{P_{dc}}{P_{av}} = (1 - |\Gamma|^2)\eta_{rect} \quad (4.1)$$

where  $\Gamma$  is the rectifier circuit's input reflection coefficient.

The performance of conventional rectifier circuits are usually highly dependent on power since both  $\eta_{rect}$  and  $\Gamma$  are power dependent. Figure 4.1 shows the typical  $\eta_{rect}$  of a diode rectifier versus input power [57]. The rectification efficiency increases with the input power level until the saturation point where the diode breakdown effects become dominant. At the same time, as shown in Figure 4.2, rectifiers typically demonstrate increasing input conductance with input power, due to their conduction angle increase (the influence of parasitic reactive elements can usually be cancelled with the impedance transformation network). The power-dependent input impedance of diodes makes it difficult to minimize the reflection coefficient  $\Gamma$  in a wide range of input power levels. Therefore, in conventional rectifier designs,  $\eta_{RF-DC}$  is usually optimized at a specific power level, and would experience significant degradation as the power level changes [57].

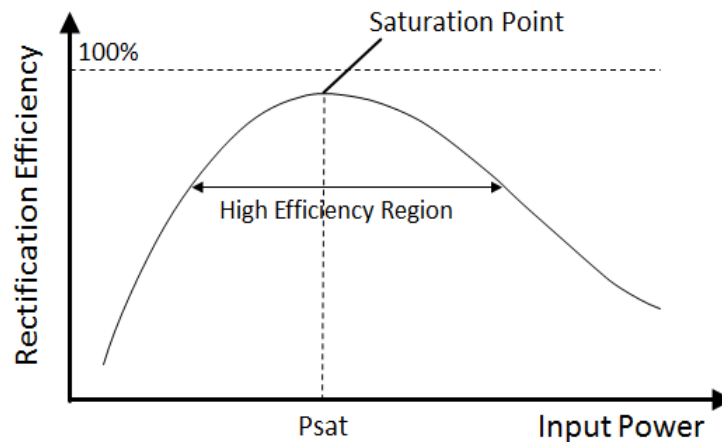


Figure 4.1. Typical rectification efficiency vs. input power of a P/N diode

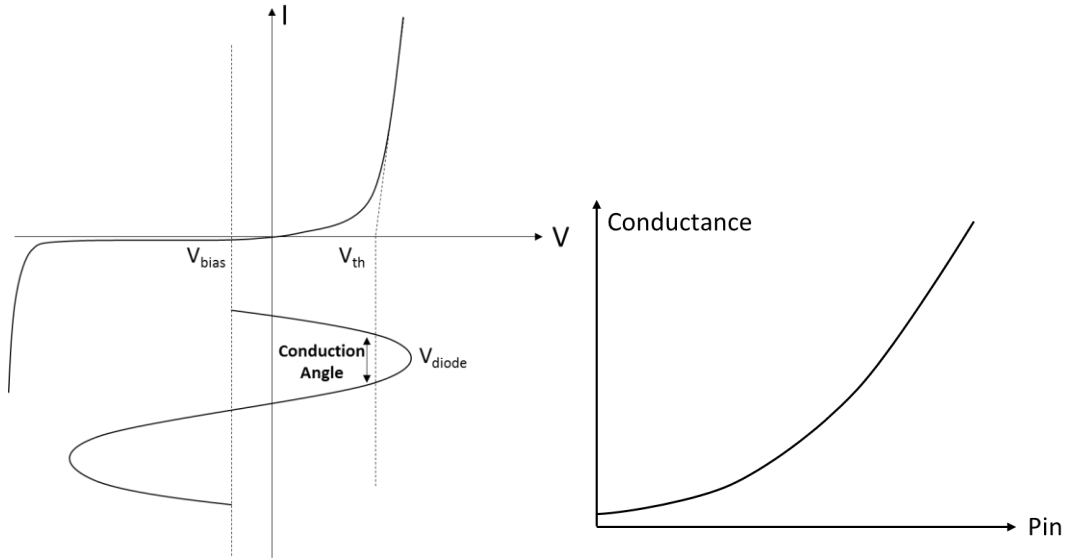


Figure 4.2. Conduction angle of diode and conductance vs. input power level (parasitic reactive components are cancelled with impedance transformation network)

#### 4.2.2 Operation Principle of the Multi-way Rectifier Array

The multi-way rectifier network exploit the rectifiers' power dependent nonlinear behavior to achieve adaptive power distribution among the rectifier devices as input power level changes. A two-way rectifier array is used to explain the operation principles. The basic circuit diagram in Figure 4.3. The final DC output power is the combination of output power from both rectifiers.

The real power delivered to the individual rectifiers are denoted as  $P_1$  and  $P_2$ . The power split ratio between the rectifiers,  $P_1/P_2$ , is equal to the conductance ratio between the rectifiers, shown in equation (4.2):

$$\frac{P_1}{P_2} = \frac{G_1(P_{in})}{G_2(P_{in})} \quad (4.2)$$

where  $G_1$  and  $G_2$  represent the conductance of the rectifier 1 and 2, and both are functions of input power.

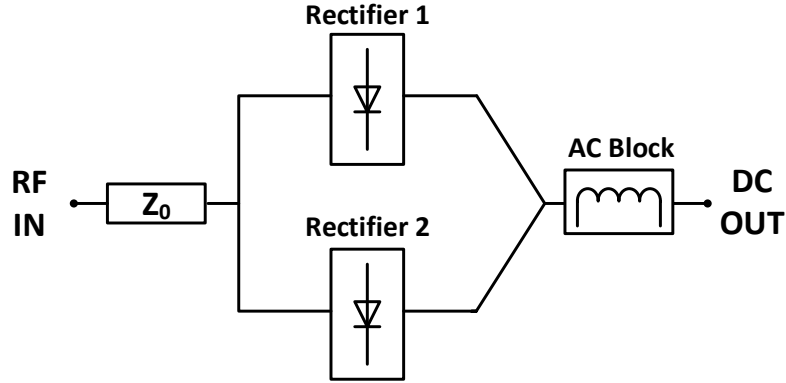


Figure 4.3. A basic block diagram intended to describe the operating principles of the adaptive power distribution rectifier array. The block diagram uses two individual rectifiers.

As mentioned before, diodes typically demonstrate an increasing input conductance when input power increases as shown in Figure 4.2. This trend can be inverted with an impedance transformation network (for example, a quarter-wave transmission line). Therefore, it can be designed such that  $G_1(P_{in})$  is a decreasing function of power,  $G_2(P_{in})$  is an increasing function of power. The power distribution ratio  $P_1/P_2$  as a function of power can therefore be adjusted by changing  $G_1(P_{in})$  and  $G_2(P_{in})$ .

The ideal trend of  $G_1, G_2$  and  $G = G_1 + G_2$ , are demonstrated in Figure 4.4.  $G_0$  represents the source conductance. Each rectifier has its maximum operating power (beyond these points, the diodes reach their breakdown region and their efficiencies quickly degrade), namely  $P_{1sat}$  and  $P_{2sat}$ . The rectifier network has three operation regions:  $P_{in} \leq P_{1sat}$ ;  $P_{1sat} < P_{in} \leq (P_{1sat} + P_{2sat})$ ; and  $P_{in} > (P_{1sat} + P_{2sat})$ . For convenience, the three regions are referred to as single device operation region, transition region and saturation region. The conductance ratio  $G_1/G_2$  (and therefore the corresponding  $P_1/P_2$ ) should be designed to be much higher than 1 in the single device region; gradually decreasing with power in the transition region; and stable in the saturation region. This will allow most RF

power to be distributed to Rectifier 1 in the single device operation region, and Rectifier 2 receives increasing amount of power as  $P_{in}$  increases in the transition region, until both devices saturates, as shown in Figure 4.5. The total conductance  $G = G_1 + G_2$  is always equal to  $G_0$  to minimize power loss due to impedance mismatch. The detailed behavior is analyzed as following.

In the single device operation region, the input power is below the point where Rectifier 1 reaches its maximum efficiency. In this case, the power distribution network distributes most of the input RF power into Rectifier 1. In the ideal case,  $P_1 = P_{in}$  and  $P_2 = 0$ . Since the rectification efficiency increases with input power level (as can be seen in Figure 4.1), such an approach will maximize the efficiency under the low-power condition.

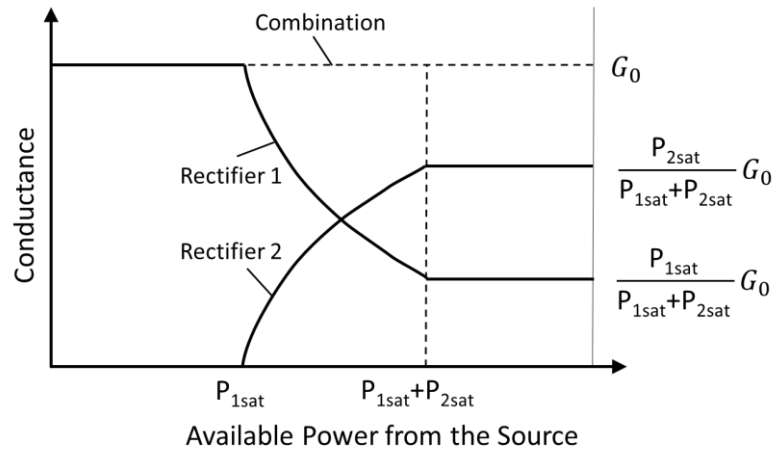


Figure 4.4. The ideal conductance variation curves of Rectifier 1, Rectifier 2, and their combination.

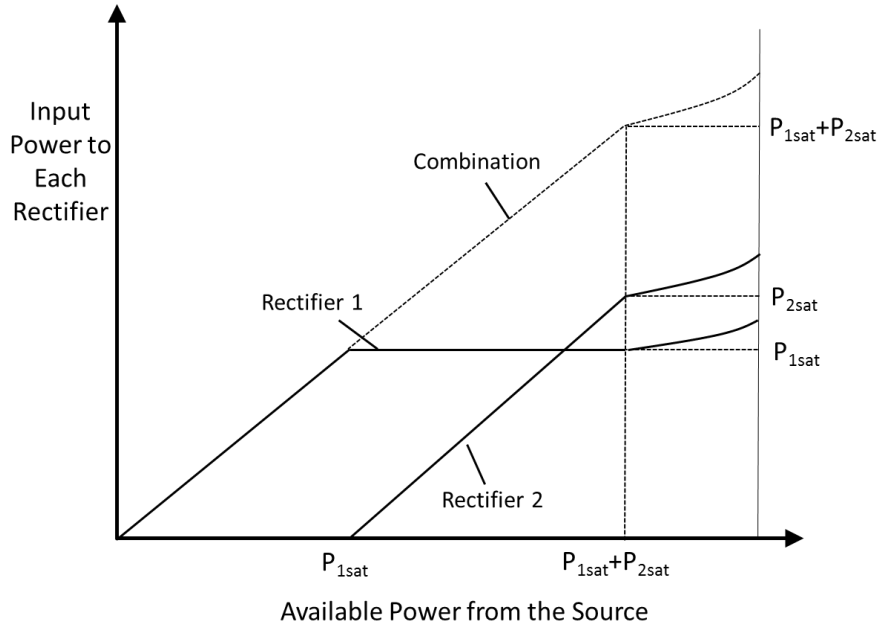


Figure 4.5. Ideal input power to Rectifier 1, Rectifier 2, and their combination, as functions of available power level.

In the transition region, both rectifiers receive RF power and contribute to the output power. However, as input power increases, the power distribution is gradually shifted from  $P_1 = P_{1sat}$  and  $P_2 = 0$  at  $P_{in} = P_{1sat}$ , to  $P_1 = P_{1sat}$  and  $P_2 = P_{2sat}$  at  $P_{in} = (P_{1sat} + P_{2sat})$ . During this transition,  $P_1$  remains the same, i.e.  $P_1 = P_{1sat}$ , and  $P_2$  will be  $P_2 = P_{in} - P_{1sat}$ . In this way, Rectifier 1 always operates at its maximum-efficiency, while the efficiency of Rectifier 2 gradually increases with power level, until it reaches its peak efficiency at  $P_{in} = (P_{1sat} + P_{2sat})$ . In order to achieve  $P_1 = P_{1sat}$ , and  $P_2 = P_{in} - P_{1sat}$ , the conductance ratio should satisfy (4.3):

$$\frac{G_1(P_{in})}{G_2(P_{in})} = \frac{P_{1sat}}{P_{in} - P_{1sat}} \quad (4.3)$$

The total conductance  $G = G_1 + G_2$  should be equal to  $G_0$  to minimize power mismatch loss as input power changes. Therefore,  $G_1$  and  $G_2$  can be derived from (4.3) as equation (4.4):

$$\begin{aligned} G_1(P_{in}) &= \frac{P_{1sat}}{P_{in}} \cdot G_0 \\ G_2(P_{in}) &= \frac{P_{in} - P_{1sat}}{P_{in}} \cdot G_0 \end{aligned} \quad (4.4)$$

where  $G_0$  is the source conductance which is equal to the real part of  $1/Z_0$ .

In the saturation region, the power level distributed to each device receive is beyond its saturation point. In this region, the power split ratio  $P_1/P_2 = P_{1max}/P_{2max}$  is maintained such that the rectification efficiency for the two devices decay at the same rate.

A comparison among the rectification efficiency of a single rectifier, simple shunt connection of two rectifiers, and wide dynamic range rectifier network described in this chapter (ideal case) are shown in Figure 4.6. In single device operation region, since all the power is distributed to Rectifier 1, the efficiency of the rectifier network is equal to the efficiency of a single rectifier circuit. In saturation region, since both devices reach their breakdown region and decay at the same rate, the efficiency of the rectifier network is equal to the shunt of two rectifiers. In the transition region, Rectifier 1 maintains maximum efficiency. The efficiency of Rectifier 2 gradually increases with power and only reaches maximum efficiency at  $P_{in} = P_{1max} + P_{2max}$ ; however, when  $P_{in} < P_{1max} + P_{2max}$ , although the efficiency of Rectifier 2 is not maximized and degrades the overall efficiency, due to the RF power distributed to Rectifier 2 is small, the degradation of the overall efficiency is small. Therefore, the efficiency of the wide dynamic range rectifier network can approach the outline in Figure 4.6.

The circuit described here not only allows the best rectification efficiency to be achieved, but also minimizes the RF power reflection due to impedance mismatch. As the conductances of Rectifier 1 and Rectifier 2 exhibit opposite trends of variation with power (refer to Figure 4.4), the total conductance of the entire rectifier circuit remains stable when input power changes. Therefore, the reflection coefficient ( $\Gamma$ ) can be minimized regardless of the fluctuation of input power levels.

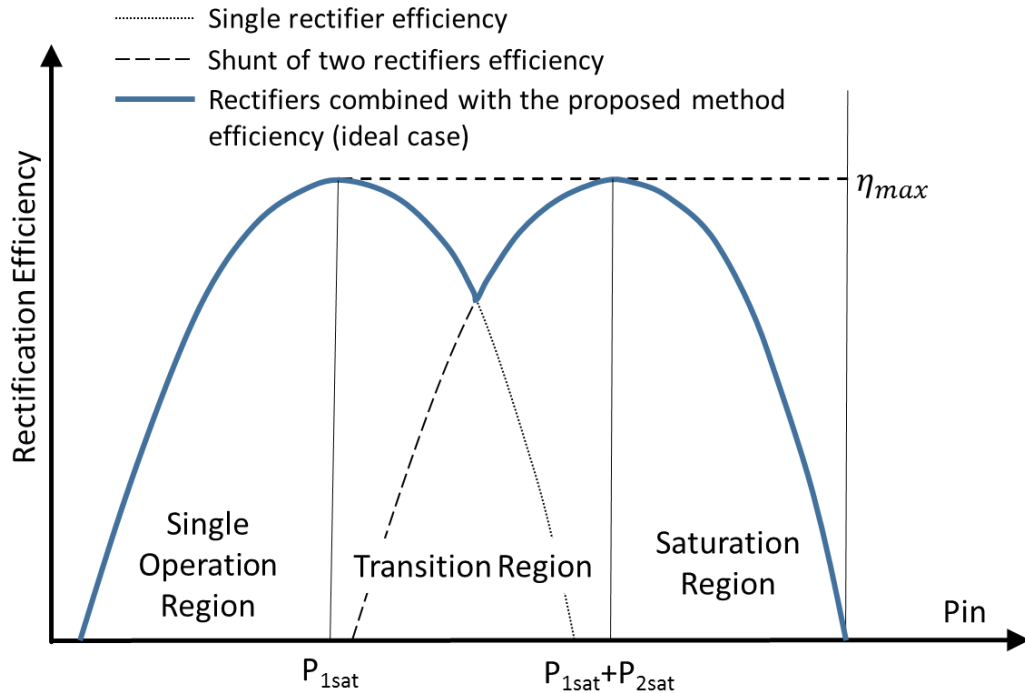


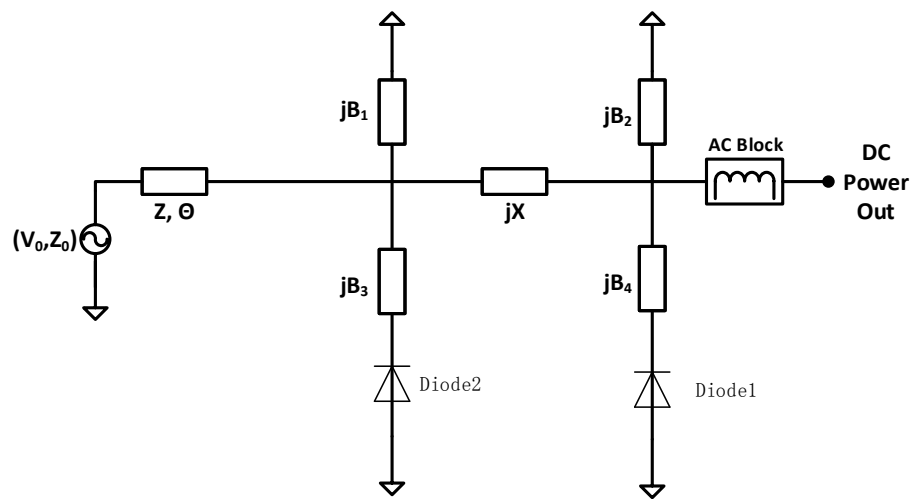
Figure 4.6. The comparison of rectification efficiencies: one single rectifiers; simple shunt of two rectifiers; and adaptive power distribution rectifier array circuit described in this dissertation.

### 4.2.3 Circuit Design Approach

When designing such a rectifier array, different impedance transformation networks should be designed for each of the individual diodes to approach the conductance ratio

shown in Figure 4.4. Figure 4.7 (a)-(b) shows an example of realization of the proposed circuit scheme. Figure 4.7 (a) shows a lumped element configuration (the reactance  $jB_1 \sim jB_4$  and  $jX$  are provided by inductors or capacitors), and is rearranged into the form given by Figure 4.7 (b) to explain its operation principle. Note that the actual configuration of the circuit can be either lumped element based, or transmission line based, or combination of the two.

The passive component values are chosen such that the diodes' nonlinear impedances are transformed to provide the conductance curves as functions of input power shown in Figure 4.7 (b). The power dividing ratio  $P_1/P_2 = G_1/G_2$  is therefore much greater than 1 in the single device operation region, decreases with input power in the transition, and reaches a relatively stable point in the saturation region, allowing the proposed adaptive power distribution scheme (shown in Figure 4.5) to be achieved. The network is then matched to the source with conventional impedance matching techniques. In this case, a quarter wave transmission line is shown as an example.



(a)

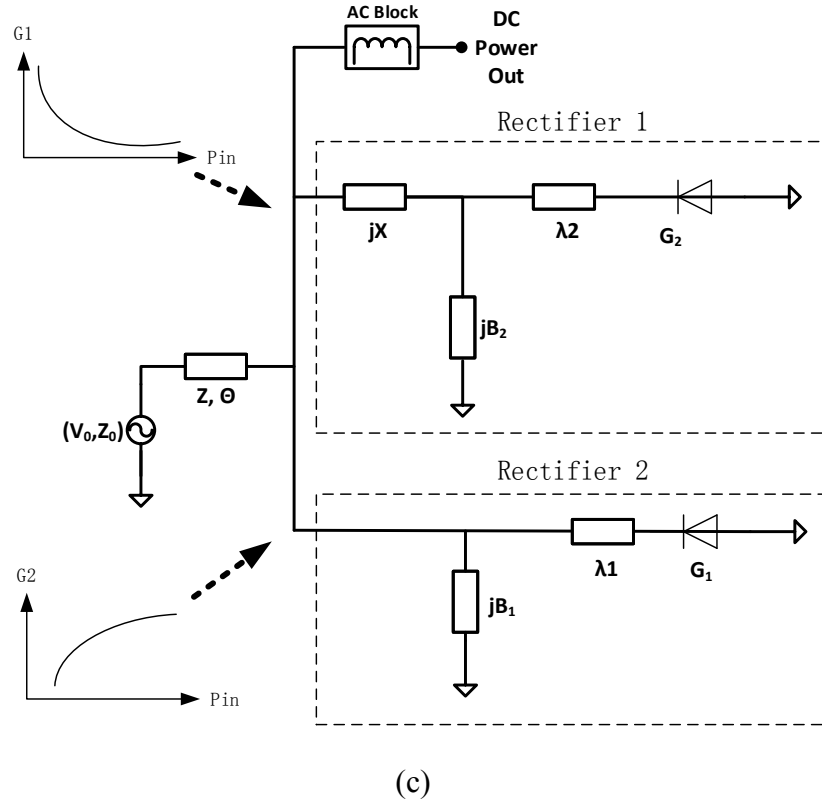


Figure 4.7. An example realization of the proposed adaptive power distribution rectifier circuit scheme: (a) lumped-element based design; (b) the rearranged form of the circuit and the input conductance versus power for each branch.

#### 4.2.4 Uneven Power Division and Multi-Device Power Division

In order to further expand the dynamic range of the rectifier circuit, the transition region can be extended by using devices with greater differences in power handling capabilities, i.e.  $P_{1sat}$  and  $P_{2sat}$ , such that the two peaks in Figure 4.6 are further apart. However, this will cause more efficiency degradation within the transition region. As another approach, the circuit topology can be extended to a multi-device network to include a larger number of diode rectifiers ( $\geq 3$ ). An example of a lumped-elements-based multi-device network is shown in Figure 4.8. The circuit configuration will appear to be multiple rectifier cells

connected in shunt with the correct phase correlations and conductance variation trends. Expected behavior of with such a configuration is shown in Figure 4.9 (shown with an example of a three-device rectifier array). With three devices, the dynamic range is further expanded compared to the two-device rectifier array, without sacrificing the efficiency in the transition region.

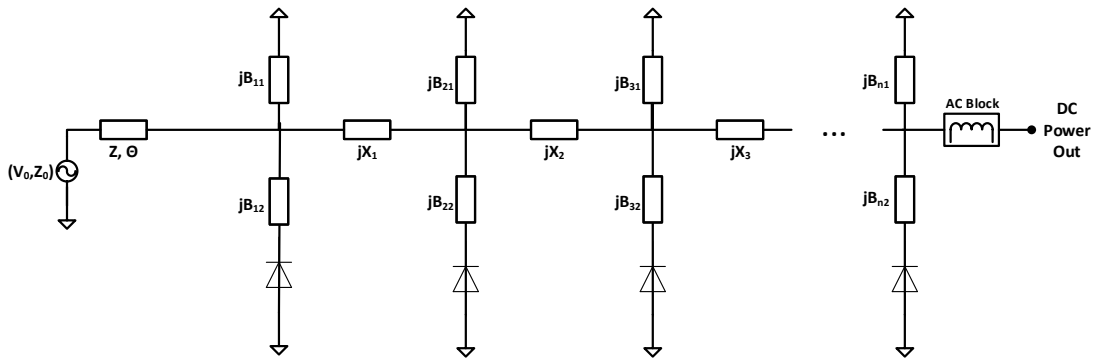


Figure 4.8. An example realization of the multi-way power distribution rectifier circuit scheme (based on lumped-elements).

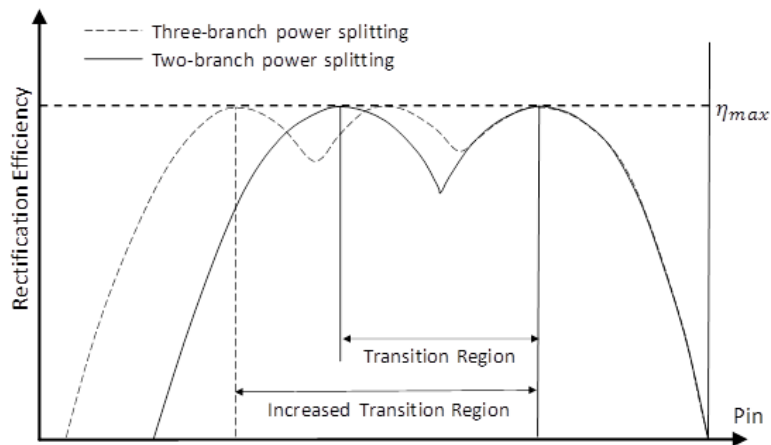


Figure 4.9. Multi-device (shown with the example of three-way rectifier array) power split efficiency, in comparison with a two-device rectifier array.

### 4.2.5 Circuit Operation Based on Impedance Modulation Theory

The operation of the described rectifier array can be explained by the impedance modulation theory [130] and can be better understood by comparing it with a Doherty amplifier structure.

The core idea of the impedance modulation theory is that the resistance or reactance of a passive RF device can be modified by applying current from a second, phase-coherent source. As a simple explanation, consider the circuit shown in Figure 4.10. Suppose  $I_1$  and  $I_2$  are two sources, then the impedance “seen” by  $I_1$  is (4.5)

$$R_1 = R \left( 1 + \frac{I_2}{I_1} \right) \quad (4.5)$$

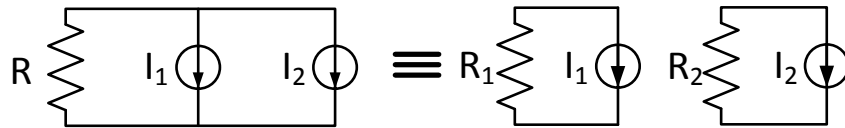


Figure 4.10. Equivalent circuits for explanation of the impedance modulation theory

Equation (4.5) indicates that the impedance “seen” by  $I_1$  is modulated by the current provided from  $I_2$ . For example,  $R_1$  can be transferred to higher resistive values if  $I_2$  is in phase with  $I_1$ , and to smaller resistive values if  $I_2$  is in antiphase with  $I_1$ .

In the case of Doherty amplifiers, the effective load resistance for the main amplifier is modulated by the auxiliary amplifier [131]. It allows the main amplifier to maintain peak efficiency in the back-off region (usually 6 dB for conventional two-way even power split Doherty amplifiers). The amplifier can therefore achieve good power added efficiency (PAE) while reaching good linearity.

In contrast to the Doherty amplifier which applies **load modulation**, the described rectifier array applies **source modulation** to achieve high rectification efficiency within a wide range of input power levels. In the described rectifier network, Rectifier 2 modulates the effective source impedance for Rectifier 1. Therefore, Rectifier 1 which operates under all power levels is referred to as the main rectifier here, while Rectifier 2 which operates only when  $P_{in} > P_{1sat}$  is referred to as the auxiliary rectifier.

Figure 4.11 shows the described rectifier network with a proper source modulation scheme. Ignoring the parasitic reactive inductance/capacitances which can be cancelled with matching circuit, the rectifiers have a decreased input resistance ( $R_1$  and  $R_2$  in Figure 4.11) as input power level increases because of the increased conduction angle. This trend is flipped by an impedance inverter (such as a quarter-wave transmission line) for the main rectifier ( $R'_1$  in Figure 4.11), which therefore exhibits increased input resistance with power.

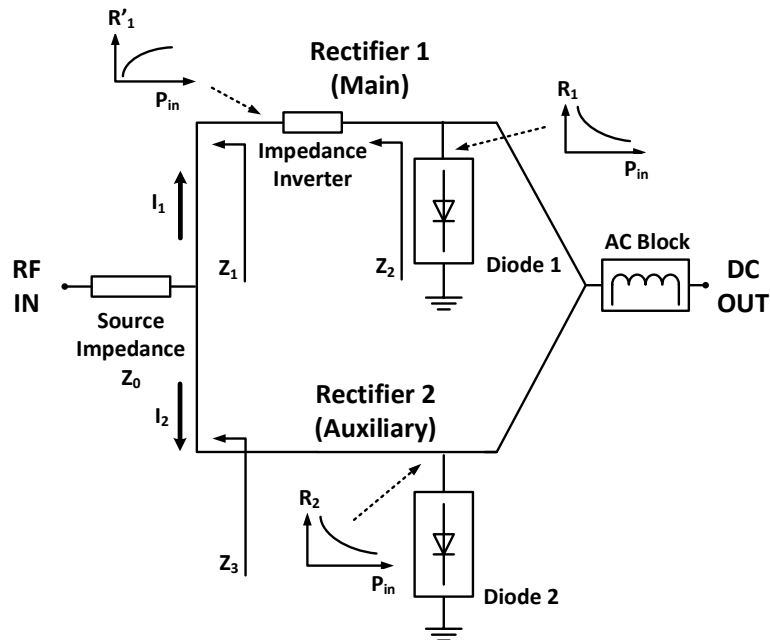


Figure 4.11. Operation principle of the adaptive power distribution rectifier array: source impedance modulation perspective.

The behavior of the proposed rectifier array in the transition region is analyzed as following. The main rectifier reaches its peak efficiency at  $P_{in} = P_{1sat}$ . As input power increases ( $P_{in} > P_{1sat}$ ), the auxiliary rectifier starts to operate, and a portion of current from the source is directed into the auxiliary rectifier. Therefore, according to equation (4.5), the modulation effect provided by the auxiliary rectifier makes the effective source resistance  $Z_1$  “seen” by the main rectifier to increase ( $Z_1 = Z_0 (1 + I_2/I_1)$ , assuming  $Z_0$  only has the real part). Since  $R'_1$  also exhibits increased input resistance as power level increases, the impedance matching condition is maintained. On the other hand, the effective source resistance  $Z_3$  “seen” by the auxiliary amplifier decreases with power since  $Z_3 = Z_0 (1 + I_1/I_2)$ . It also matches the decreasing trend of  $R_2$  as power level increases. Furthermore, as  $Z_1$  increases, Diode 1 sees an impedance  $Z_2$  that decreases with power because  $Z_1$  is inverted by the impedance inverter. Therefore, as  $P_1$  increases, the RF voltage ( $V_{RF}$ ) across Diode 1 is stabilized (since  $V_{RF} = \sqrt{P_1 Z_2}$  and  $Z_2$  reduce with power); in the ideal case,  $V_{RF}$  is kept to be constant. Because the rectification efficiency is directly determined by the voltage across the diode, a constant  $V_{RF}$  will allow the main rectifier to operate at its peak efficiency regardless of the variation of  $P_{in}$  in the transition region. Figure 4.12 shows the input voltage and current of the two rectifiers as available power level changes with an example of even power distribution where the power rating of the two rectifiers are the same, i.e.  $P_{1sat} = P_{2sat}$ . Figure 4.13 shows the output power of the two rectifiers, and their combination, as available power level changes. In the ideal case, the source modulation scheme of the rectifier network circuit will provide a 3 dB backoff region where the efficiency of the main rectifier is kept near-constant, which is similar to the 6-dB backoff region in Doherty amplifiers.

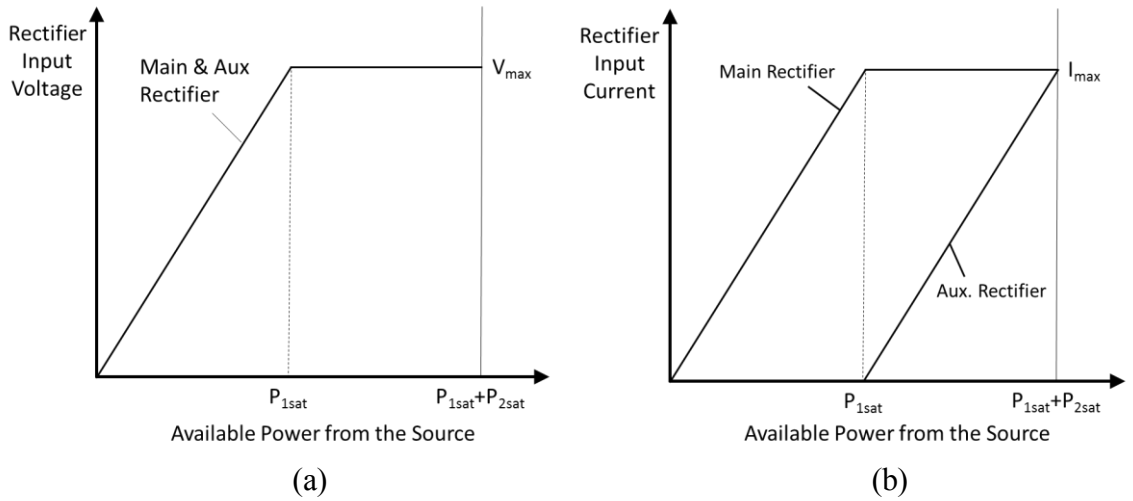


Figure 4.12. Adaptive power distribution rectifier array operation principles: (a) device voltages; and (b) device currents at different available power levels. Pictures show the case of even power splitting with ideal devices.

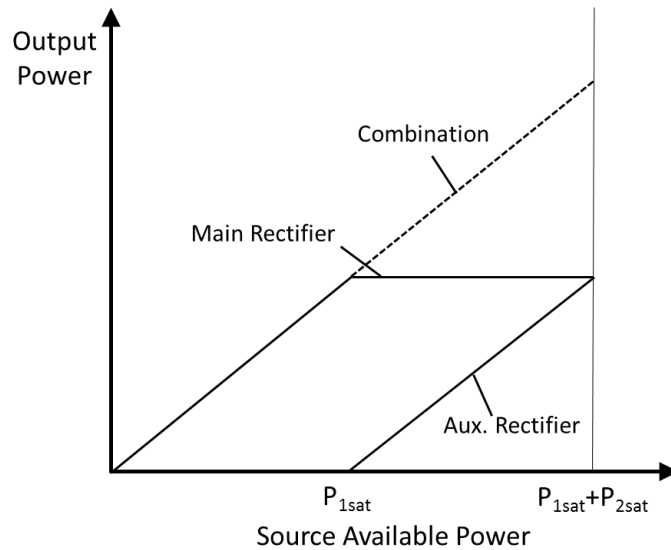


Figure 4.13. Adaptive power distribution rectifier array operation principles: output power at different available power levels. Pictures show the case of even power splitting with ideal devices.

## 4.3 Adaptive Power Distribution Rectifier Network

### Implementation and Measurement

#### 4.3.1 Circuit Design and Simulation

A 900 MHz two-way rectifier array is designed, fabricated and tested. Two high sensitivity rectifier diodes (HSMS2852) are used to implement the high dynamic range rectifier. The circuit is designed with microstrip line impedance matching networks on Rogers RO4003C laminates. A 1.2 V rechargeable battery is used as the load. For comparison, a single diode rectifier is designed with the same device and optimized to achieve maximum efficiency at the same frequency. The schematic of the circuit is shown in Figure 4.14. The specifications of the circuit is summarized in Table 4.1.

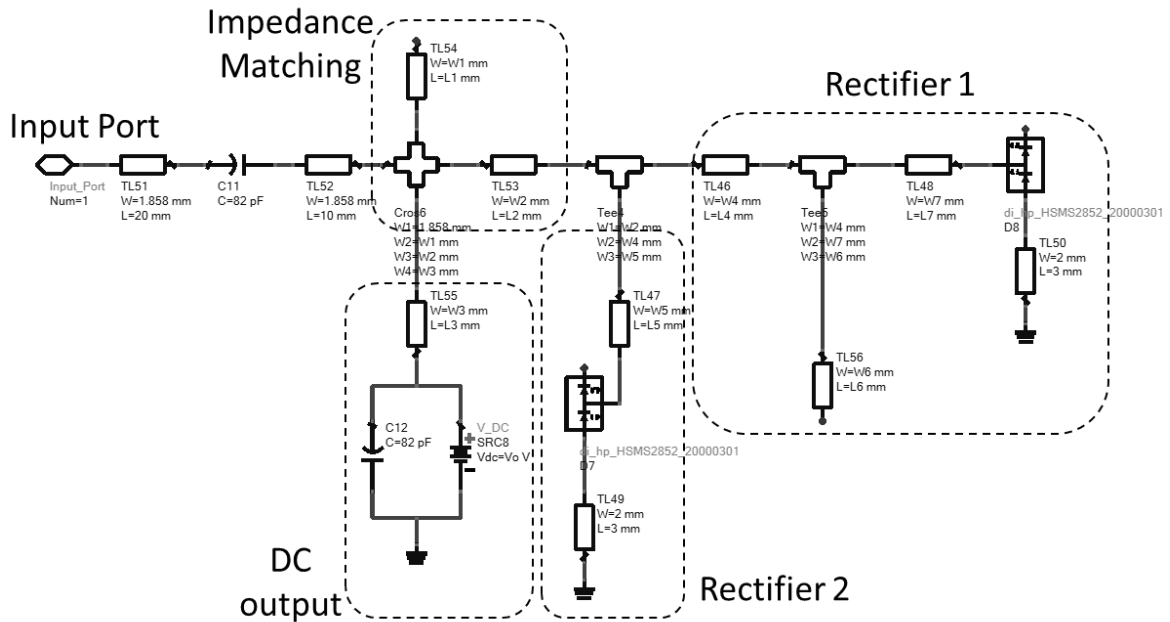


Figure 4.14. Circuit diagram of the adaptive power distribution rectifier array.

Table 4.1. Specifications for the adaptive power distribution rectifier array

<b>Component</b>	<b>Specification</b>
<b>Frequency</b>	900 MHz
<b>Substrate</b>	Rogers RO 4003C
<b>Diodes</b>	Avago HSMS2852
<b>Load</b>	1.2 V rechargeable battery
<b>Transmission Line Parameters</b>	
L1, W1	11 mm, 5 mm
L2, W2	36 mm, 5.4 mm
L3, W3	54.5 mm, 0.5 mm
L4, W4	7.5 mm, 2.75 mm
L5, W5	44.5 mm, 1.25 mm
L6, W6	75 mm, 5 mm
L7, W7	45.1 mm, 1 mm

Firstly, the input impedance matching circuit for Diode 2 is designed to cancel the effect of its parasitic reactive elements and exhibit a conductance increasing with power. Then, the input impedance matching circuit for Diode 1 is designed such that it exhibits a conductivity decreasing with power, while reaches the same conductance as rectifier 1 at their saturation points. After that, the two rectifier devices are shunt connected and impedance matched to the 50 Ohm input impedance. The impedance transform network is adjusted such that the conductivity ratio  $G_1/G_2$  is much greater than 1 in the single diode operation region, decreases with the input power in the transition region, and reaches a relatively stable point in the saturation region, allowing the aforementioned adaptive power distribution to be achieved. The power distributed to each rectifier device, as a function of input power level, is shown in Figure 4.15. It can be seen that the power distributed to

Rectifier 1 is much higher than Rectifier 2 below  $P_{av}$  of 1 dBm (the single device operation region). Within the  $P_{av}$  ranging from 1 dBm to 5 dBm, the power distributed to Rectifier 2 increases as power increase, until reaching equal power distribution at 5 dBm. This is the transition region of the rectifier circuit. Afterwards, the power distribution ratio remains stable between both rectifiers (the saturation region).

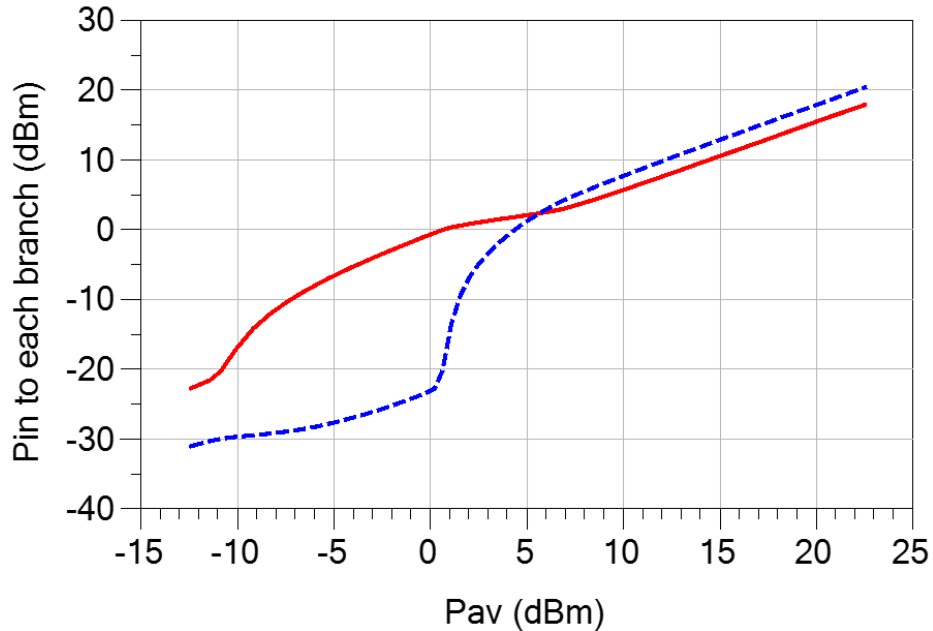


Figure 4.15. Simulated RF power distributed to each rectifier device as functions of available power level from the source. Red solid curve shows the RF power distributed to Rectifier 1, while the blue dashed curve shows the RF power distributed to Rectifier 2.

The input conductances of the entire rectifier network is stable over a wide range of input power levels so that return loss is minimized when input power level changes. The return loss as a function of available power from the source is shown in Figure 4.16. It can be seen that good impedance matching (return loss  $< -10$  dB) is achieved within a wide range of available power levels from -5 to 15 dBm, which is much better than the single

rectifier circuit which only achieves return loss  $< -10$  dB within the range of available power levels from 4 to 12 dBm.

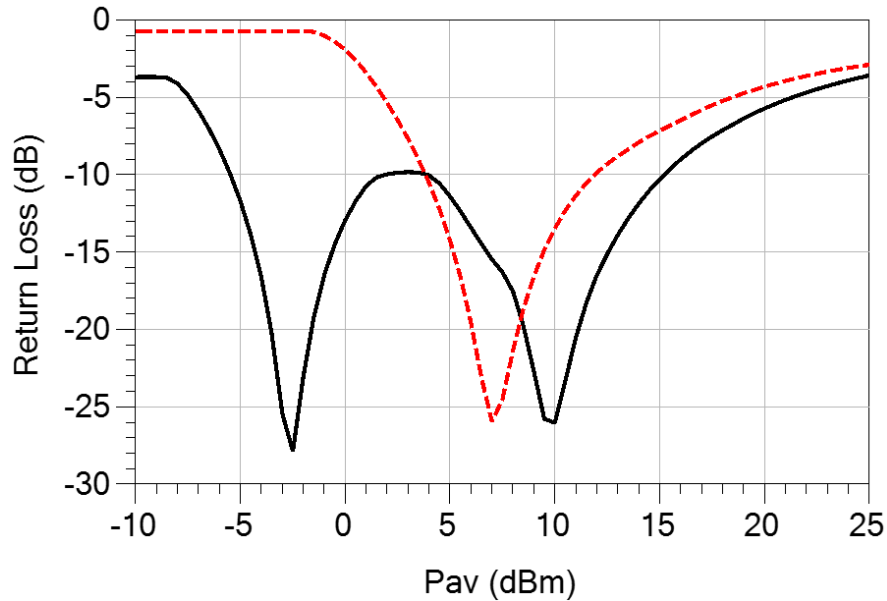


Figure 4.16. Simulated return loss for the adaptive power distribution circuit, in comparison with the return loss for a single diode rectifier circuit designed with the same device and optimized at the same frequency. Black solid curve shows the return loss of the adaptive power distribution circuit, while the red dashed curve shows the return loss of the single diode rectifier circuit.

The overall efficiency, defined by equation (4.1), is shown in Figure 4.17 as a function of source available power levels. It can be seen that the overall efficiency of higher than 60% is achieved within the 16 dB range of available power level (from -3 to 13 dBm) with the adaptive power distribution rectifier, which is much wider than what is achieved by the single diode rectifier circuit (6 dB range of  $P_{av}$ , from 3 dBm to 9 dBm). The maximum efficiency achieved by both circuits are at a very similar level (70.2% for the adaptive power distribution circuit and 69.7% for the single diode rectifier circuit).

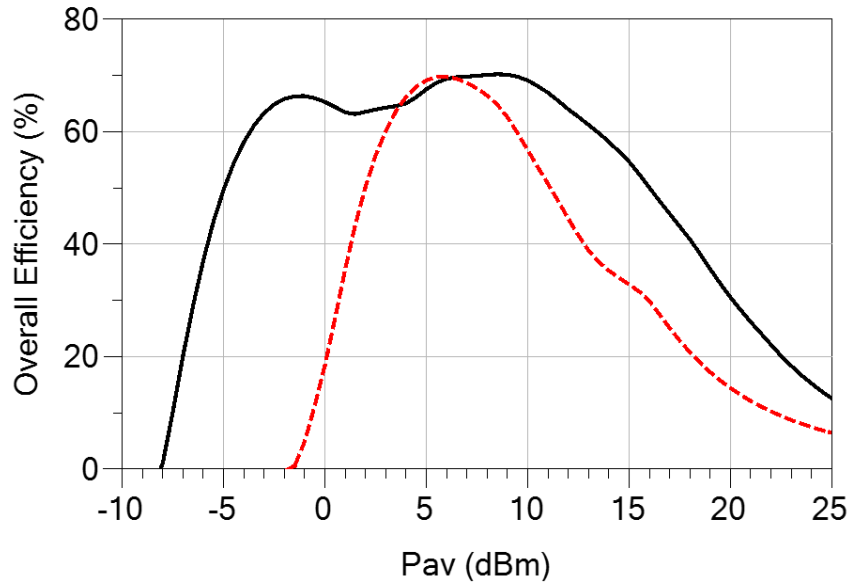


Figure 4.17. Simulated overall efficiency for the adaptive power distribution circuit, in comparison with the return loss for a single diode rectifier circuit designed with the same device and optimized at the same frequency. Black solid curve shows the overall efficiency of the adaptive power distribution circuit, while the red dashed curve shows the overall efficiency of the single diode rectifier circuit.

### 4.3.2 Circuit Fabrication and Measurement Setup

The circuit is fabricated and measured in laboratory. A photograph of the rectifier network circuit is shown in Figure 4.18. In lab measurement, the RF signal is generated by an Anritsu MG3681A RF signal generator. The RF signal is then fed through a HP 778D dual directional coupler to the rectifier circuit. The reflected RF power is monitored by an Agilent E4419B EPM series power meter paired with an 8485A power sensor, which allows the return loss to be calculated. The output voltage and current are measured with a Fluke 867B graphical multimeter and an Agilent 34405A digital multimeter. The measurement setup is shown in Figure 4.19.

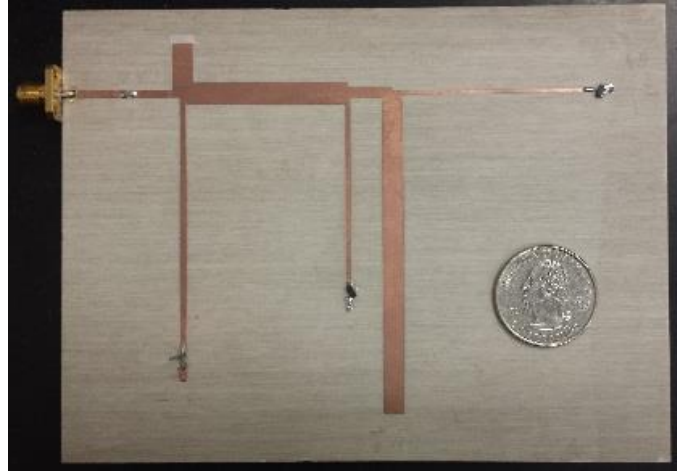


Figure 4.18. A photograph of the two-way wide dynamic range rectifier array.

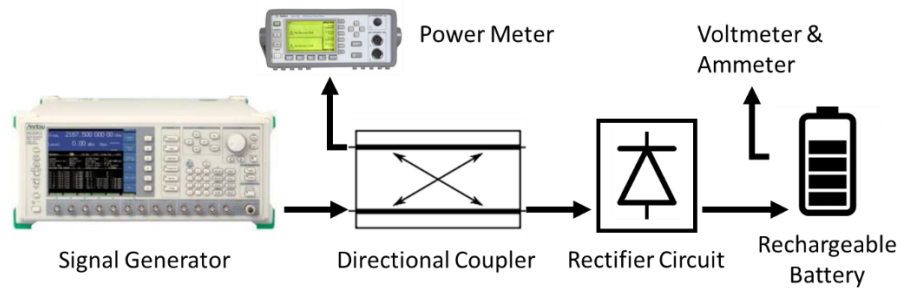


Figure 4.19. Measurement setup.

### 4.3.3 Measurement Results

The measured reflection coefficient is shown in Figure 4.20. As can be seen, the rectifier array circuit allows minimal reflection within the whole range of interest (smaller than -10 dB in the range of available power levels from 0 to 13 dBm), exhibiting significant advantage over the single diode rectifier circuit. The measured overall efficiency is shown in Figure 4.21. It can be seen that the rectifier array circuit demonstrates  $> 50\%$  overall efficiency over 17 dB variation of input power levels (from -1 dBm to 16 dBm), which is 10 dB wider than the dynamic range of the single diode rectifier (from 3 dBm to 10 dBm).

The dynamic range enhancement at low power levels ( $< 5$  dBm) is attributed to the improved impedance matching condition. The dynamic range enhancement at high power levels ( $> 6$  dBm) is attributed to the improved rectification efficiency due to the combination of the two devices as discussed in Section 4.2.1. Moreover, the rectifier array circuit allows for a better control of the harmonic frequencies and therefore is capable of achieving better overall efficiency than a single rectifier circuit. As can be seen from Figure 4.21, the rectifier array demonstrates a peak efficiency of 66%, which is 5% higher than that of the single diode rectifier (61 %). The measurement results are in good agreement with the simulation results.

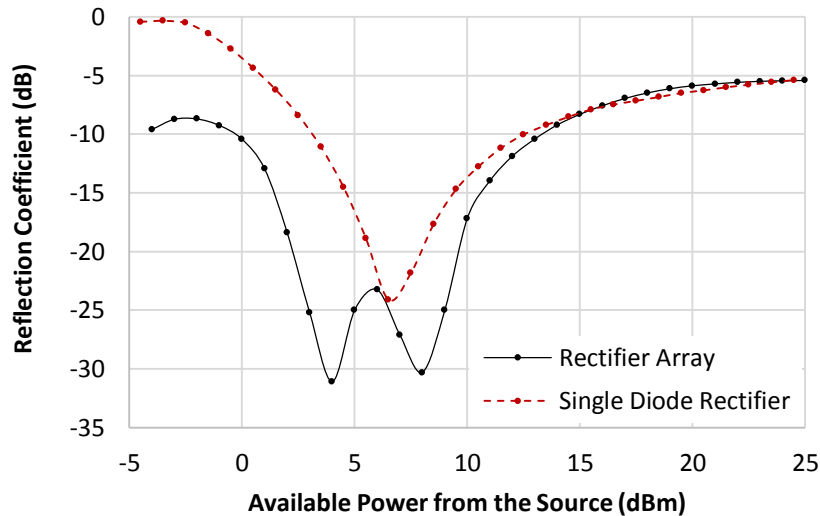


Figure 4.20. The measured reflection coefficient for the wide dynamic range rectifier array, in comparison to a single diode rectifier circuit optimized at the same frequency.

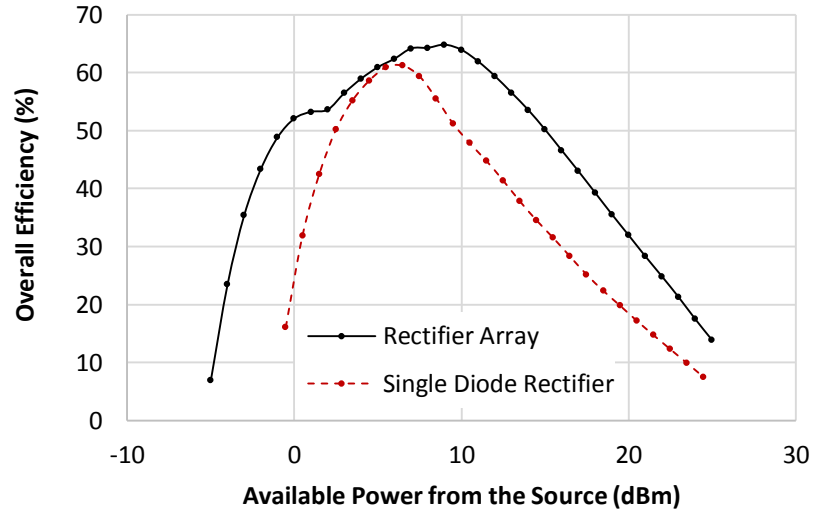


Figure 4.21. The measured overall efficiency (considering both the rectification loss and impedance mismatch reflection) for the wide dynamic range rectifier array, in comparison to a single diode rectifier circuit optimized for the highest efficiency.

## 4.4 Conclusion

This chapter presents a novel adaptive power distribution rectifier array for wide dynamic range RF-DC conversion. Such a rectifier array consists of multiple rectifier devices. An adaptive power distribution network divides the RF power dynamically among the devices according to the input power level. The adaptive power distribution scheme can be achieved with a simple passive circuitry by taking advantage of the nonlinear input impedances of the rectifier devices. Such a rectifier array improves both the rectification efficiency and the impedance matching condition, and therefore, results in a significant enhancement of the dynamic range. The proposed method is verified with simulation and experiments. A 900 MHz two-way rectifier array is designed and tested showing  $> 50\%$  overall efficiency over 17 dB dynamic range (from -1 dBm to 16 dBm) which is enhanced

by 10 dB, and has a peak efficiency of 66%, being 5% higher than a conventional rectifier designed with the same rectifying device.

Table 4.2 lists the comparison of the performance of the described dynamic power distribution rectifier array with a few existing publications.

Table 4.2. Comparison of Wide Dynamic Range Rectifier Circuits

<b>Author &amp; published year</b>	<b>Method</b>	<b>Frequency</b>	<b>Dynamic range when RF-to-DC efficiency higher than 50%</b>	<b>Peak efficiency</b>	<b>Process</b>
Scorcioni [131], 2012	Dickson charge pump with adaptive voltage regulator	2.45 GHz	NA (peak efficiency <50%) Efficiency > 30% from -12 dBm to 1 dBm	45%	130 nm CMOS
Satoshi [132], 2013	Three-stage rectifier with CPU-based selector	2.4 GHz	NA (peak efficiency <50%) Efficiency > 25% from 15 dBm to 40 dBm	40%	PCB
Taylor [53], 2014	Resistance compression network	868 MHz	10.1 dB (20 dBm to 30.1 dBm)	70%	PCB
This work	Adaptive power distribution network	900 MHz	17 dB (-1 dBm to 16 dBm)	66%	PCB

# Chapter 5

## Conclusions and Future Directions

### 5.1 Summary

In this dissertation, a few approaches are described in order to improve the efficiency, and sensitivity of wireless power transfer and wireless power harvest systems, as well as to enhance their performance in fluctuating and unpredictable environments. A Duffing nonlinear resonator is developed which achieves significantly wider bandwidth than a linear resonator with the same quality factor, while reaching a similar level of resonant voltage amplitude. The Duffing resonator is used in WPT systems to improve their tolerance to coupling factor variation, and in WPH systems to improve their tolerance to frequency misalignment. A high sensitivity wireless power harvester which collects RF energy from AM broadcast stations is designed for powering the wireless sensors in structural health monitoring systems. The harvester successfully collects RF power from a distance of 6 miles away from a local 50 kW AM station. Last but not least, a wide dynamic range rectifier array is designed with the adaptive power distribution method. The rectifier array achieves high RF-to-DC efficiency within a wide range of input power levels, and is useful in WPT and WPH applications where the RF power collected by the receiver is subject to fluctuation.

## **5.2 Future Work**

### **5.2.1 Duffing resonator circuit for High Power WPT systems**

Currently, the Duffing resonator circuit used for design and test are designed at relatively low power levels ( $< 1$  Watts). As a next step of research, a Duffing resonator-based WPT system can be designed and tested at moderate (tens of Watts) to high (hundreds of Watts) power levels to understand their performance and properties under strong excitation. For moderate power level operation, the BST varactors which exhibits strong nonlinearity with tens to hundreds of Volts voltage swing can be used to form the Duffing resonator. For high power operation, the ceramic varactors which shows strong nonlinearity with thousands of Volts voltage swing can be used to form the Duffing resonator.

### **5.2.2 Duffing resonator circuit for WPH systems to collect RF energy from multiple stations simultaneously**

Duffing resonator circuits provides a much wider bandwidth as compared to conventional linear resonator circuits, and therefore, enables the possibility of simultaneously collecting RF energy from multiple broadcast stations. Firstly, the Duffing resonator-based WPH receiver introduced in Section 3.7 will be tested in field environment. Subsequently, theoretical and experimental investigation will be conducted to understand the Duffing resonator's behavior under multiple uncorrelated excitation frequencies. After that, a Duffing-based WPH receiver, which is simultaneously capable of collecting RF energy from multiple broadcast stations, will be designed and tested. Some other practical

issues with the Duffing-based WPH receiver, for example, stability issues and start-up issues, will be further investigated and solved.

### **5.2.3 Multi-device adaptive power distribution rectifier circuit design and test**

The multi-device adaptive power distribution rectifier circuit is described in Section 4.2.4. As future research, the circuit will be simulated, fabricated and measured to show the benefit of using multiple devices for better dynamic range. Then, the rectifier circuit will be integrated into WPT and WPH systems in order to improve their performance when the input RF power level varies.

## **Appendices**

# Appendices

## Appendix A

### Matlab Codes For Computing the Amplitude-Frequency Response of the Duffing resonator circuit

#### Appendix A-1

```
% This program is for computing the Duffing resonance response of
% nonlinear resonance circuit with nonlinear C. Multiple variables,
% including excitation amplitude, nonlinear character of the varactor,
% loss in the circuit, can be swept.
```

```
% The computation is based on the general solution of the Duffing
equation.
% Only the 1st and 3rd nonlinear coefficient of the Duffing equation
will be
% taken into consideration. This is also the limit of this computation
method.
% Therefore, there may be inaccuracy if the Duffing equation have
strong
% higher-than-3rd nonlinearity.
```

```
close all; clear all; clc
```

```
%Pm=zeros(1,1+fmax-fmin);
%QQ=logspace(0,2.5,350);
```

```
%Parameter Characterization
L=900*1e-6; %inductance in H
r=50; %resistance in Ohm
Cmax=100*1e-12; %2nd order of capacitance in F
V2=1; %Unit: V
Vs=0.1; %Excitation Amplitude in V
```

```
%Calculation
figure('Position',[800-100 600-100 600 400])
```

```
Vsmax=0.12;
Vsmin=0.06; % Voltage range
Steps=5; % Number of steps
```

```
fmin=1*1e3;
fmax=2000*1e3; %Frequency Range
num=100; %number of steps
```

```
DU=zeros(Steps+1, num+1);
```

```

DD=DU;
D=zeros(Steps+1, num+1,3);

i=1;
j=1;

for Vs=Vsmin:(Vsmax-Vsmin)/Steps:Vsmax
    for f=fmin:(fmax-fmin)/num:fmax
        w=2*pi*f;

        %a1=1/Cmax;
        %a2=-21*(1-w^2*L*p)*(w^2*L*k)+1.5*r^2*w^2*k*p;
        %a3=16/(9*V2^2*Cmax^3);
        %R=roots([a1,a2,a3, -A^2]); %Roots of Nonlinear Equations

        A6=16/(9*Cmax^6*L^2*V2^4);
        A4=(8*(- w^2 + 1/(Cmax*L)))/(3*Cmax^3*L*V2^2);
        A2=(- w^2 + 1/(Cmax*L))^2 + (r^2*w^2)/L^2;
        A0=-Vs^2/L^2;
        R=roots([A6, A4, A2, A0]);

        R=R.^5.*(imag(R)==0);
        D(i,j,:)=R(:);
        DU(i,j)=max(R);
        DD(i,j)=min(R(find(R)));
        j=j+1;
    end
    i=i+1;
    j=1;
end

% Graphical Plotting
figure (1)
hold on
MAX=max(max(DU));
for i=1:Steps
    plot(fmin:(fmax-fmin)/num:fmax, DU(i,:)/MAX, 'b-',fmin:(fmax-
fmin)/num:fmax,DD(i,:)/MAX,'r-');
end
xlabel('Frequency');
ylabel('Amplitude (Normalized)');

```

## Appendix A-2

```

% This program code computes Duffing
% resonance response for an anti-series connected varactor diode pair,
% considering only the 1st and 3rd order terms in the Duffing equation.
The
% solution method is based on the general solution of Duffing equation.

```

```

close all; clear all; clc
fmin=707*1e3;
fmax=1107*1e3; %Frequency Range
num=401; %number of steps
Pm=zeros(1,1+fmax-fmin);
QQ=logspace(0,2.5,350);

%Parameter Characterization
%inductor parameters
L=900*1e-6; %inductance in H
Rs=33; %this is the source internal resistance in Ohm
r=Rs; %resistance in Ohm; this is the TOTAL resistance in the circuit,
including load
%Varactor diode parameters. Default values here are for SMV1705
Cjo=36.4*2*1e-12; %2nd order of capacitance in F
Vj=80; %Unit: V
n=70; %Grading coefficient
%Excitation
Pav=-32; % source available power in dBm
Pin=10^(Pav/10)*1e-3; %source available power in Watt
Vs=sqrt(8*Pin*Rs); %Excitation Amplitude in V

%Calculation Preparation
C1=Cjo/2;
C3=((3*Vj^2)/(n*(2*n-1)))*Cjo^3;

%Calculation
figure('Position',[800-100 600-100 600 400])
for A=0.1
for j=1:size(QQ,2)
Qe=QQ(j);
D=[]; F=[]; DU=[]; DD=[];
for f=fmin:(fmax-fmin)/num:fmax
w=2*pi*f;
%a1=1/Cmax;
%a2=-21*(1-w^2*L*p)*(w^2*L*k)+1.5*r^2*w^2*k*p;
%a3=16/(9*V2^2*Cmax^3);
%R=roots([a1,a2,a3,-A^2]); %Roots of Nonlinear Equations
A6=9/16*(1/(L*C3))^2;
A4=1.5*(1/(L*C3))*(1/(L*C1)-w^2);
A2=(1/(L*C1))^2-(2/(L*C1))*w^2+w^4+r^2/L^2*w^2;
A0=-Vs^2/L^2;
R=roots([A6, A4, A2, A0]);

F=[F [f;f;f]];
R=R.^5.*(imag(R)==0);
D=[D R];
DU=[DU max(R)];
DD=[DD min(R(find(R)))];
end
ii=find(D);
%P=0.5*ce*DU.^2.*[fmin:fmax].^2*(2*pi)^2*1e6; Pm=max(Pm,P); %maximum
power
end

%The DU and DD are peak CHARGE values on the capacitor, or max Q.

```

```

%Calculation of V
VU=DU/C1+DU.^3/C3;
VD=DD/C1+DD.^3/C3;

hold on
figure(1)
% plot(fmin:(fmax-fmin)/num:fmax, D(1,:));
% plot(fmin:(fmax-fmin)/num:fmax, D(2,:));
% plot(fmin:(fmax-fmin)/num:fmax, D(3,:));
plot(fmin:(fmax-fmin)/num:fmax, VU, 'b-',fmin:(fmax-
fmin)/num:fmax,VD,'r-');
plot(f,A);
plot(f(4:22),A2,'r*');
xlabel('Frequency');
ylabel('Amplitude (normalized)');
end

```

## Appendix A-3

```

% This program is coded for solving the Duffing function and draw the
% solutions, for a given C-V curve. This is the main function which
uses
% Runge-Kutta method to solve the differential equation. In order to
make
% it functional, some secondary .m functions are needed including
% Duffing_diff_equ.m (defines differential equation);
% BST_CV_Curve.m (defines C-V curve of variable capacitor);
% BST_diff_CV_Curve.m (differential of the above C-V curve);
% F.m (intermediate function)
% dF.m (differential of the above intermediate function)

clear all; close all; clc

f=1e3; %Frequency in kHz
%n=0;

% Solve the differential equation using Runge-Kutta Method
for f=510.7:5:520.7 %f=50:50:1500%1.5e3
    ts=[0,1e-4];
    X0=[0,0];
    [t,x]=ode15s(@Duffing_diff_equ,ts,X0,[],f);
    figure;
    plot(t,x(:,1));
    print -deps2 '.\Double Mutant';
end

function dX=Duffing_diff_equ(t,X,f) %let X(1) to be Vc, X(2) to be
V(c) '
% The C-V curve of the given variable capacitor
%syms Vc V2 Cmax Cf
V2=1; %V2 in Volt

```

```

Cmax=20*1e-12; %Cmax in F
Cf=0.1*1e-12; %Cf in F
w=2*pi*f*1e3; %frequency
Vs=0.1; %excitation in V
L=500*1e-6; %inductance in H
R=100; %resistance in Ohm

%Nonlinear Capacitor C-V curve
syms Vc;
k=20*1e-12;
p=160*1e-12;
C=-k*Vc^2+p;
%C= (Cmax-Cf) / (2*cosh(2/3*asinh(2*Vc/V2))-1)+Cf;

%Differential of C
dC=diff(C, 'Vc');

%function F
Fc=C+dC*Vc;
%Fc=F(Cmax, Cf, V2);

%Function dF
dFc=diff(Fc, 'Vc');
%dFc=dF(Cmax, Cf, V2);

V=X(1);
T=X(2);
FVc=subs(Fc, Vc, V);
dFVc=subs(dFc, Vc, V);
M=L*FVc;
N=Vs*sin(w*t)-V-R*T*FVc-L*T^2*dFVc;
dX=[T;
    N/M];
end

function C=BST_CV_Curve(Cmax,Cf,V2) %C-V curve; return a function
expression of Vc
k=20*1e-12;
p=160*1e-12;
syms Vc;
%C= (Cmax-Cf) / (2*cosh(2/3*asinh(2*Vc/V2))-1)+Cf;
C=-k*V2^2+p;
end

function dC=BST_diff_CV_Curve(Cmax,Cf,V2)
%differential of C-V curve in regarding to Vc; returns a function
expression of Vc
C=BST_CV_Curve(Cmax,Cf,V2);
dC=diff(C, 'Vc');
end

function F=F(Cmax,Cf,V2)

```

```
syms Vc
C=BST_CV_Curve(Cmax,Cf,V2);
dC=BST_diff_CV_Curve(Cmax,Cf,V2);
F=C+dC*Vc;
end
```

```
function dF=dF(Cmax,Cf,V2)
Fc=F(Cmax,Cf,V2);
dF=diff(Fc,'Vc');
end
```

## Appendix B

### Matlab Codes for Computing the Rectification Efficiency and Diode Input Impedance based on the Ritz-Galerkin Method

#### Appendix B-1

```
% This function is written for computing the rectification efficiency
and
% diode input impedance based on a nonlinear linear model (my
approach).
% The purpose for doing this is to compare my nonlinear model with Kai
Chang's
% piecewise linear model for accuracy.
% The calculation is based on a shunt rectifying diode.
% function calculates rectification efficiency and diode input
impedance
% for a given Rl at a given Vo (sounds strange, but Kai Chang's paper
does this).

clear all; close all; clc
format long

% Define diode parameters
Vt=0.026;
Is=3e-6;
Cj=0.18e-12;
Rs=25; % here Rs is the series Ohm resistance of the diode; not the
signal source
% Specify excitation source information
V=1.85;
w=2*pi*1e9;
% Specify load information
Rl=15e3;

% Firstly, assume a V, calculate the voltage on the junction Vd.
% Vd is assumed to be  $V_d = -V_i0 + V_i1 \cos(\omega t)$ , no sin part.
% consequently, V may have a sin part (but I don't care).
% Solve for Vd
syms Vi0 Vi1
vd=[Vi0,Vi1];
%options = optimset('Algorithm','Levenberg-Marquardt','TolX',1e-10);
vd = fsolve(@(vd)
solve_shuntdiode_vi(vd,V,Vt,Is,Cj,Rs,Rl,w),[1.61933,V]);
Vi0=vd(1);
Vi1=vd(2);
Vd=[-Vi0,Vi1,0];

% Current flowing through Rj
% Fourier coefficients
a0_rj = 2*besseli(0,Vi1/Vt);
```

```

a1_rj = 1/pi*(quad(@(x) Integrate_a1_rj(x,Vil,Vt),0,2*pi));
b1_rj = 0;
% Current: DC; AC_real; AC_imag
Idc_rj = Is*(exp(-Vi0/Vt)*(a0_rj/2)-1);
I1r_rj = Is*exp(-Vi0/Vt)*a1_rj;
I1i_rj = Is*exp(-Vi0/Vt)*b1_rj;

% Current flowing through Cj
% Fourier coefficients
a0_cj = 0;
a1_cj = 0;
b1_cj = -w/pi*(quad(@(x) Integrate_b1_cj(x,0,Vil,Vi0,Cj),0,2*pi));
% Current: DC; AC_real; AC_imag
Idc_cj = a0_cj/2;
I1r_cj = a1_cj;
I1i_cj = b1_cj;
% Total current
Idc = Idc_rj+Idc_cj;
I1r = I1r_rj+I1r_cj;
I1i = I1i_rj+I1i_cj;
I = [Idc, I1r, I1i];

% From the current, calculate the voltage across the whole diode
(consider
% the series resistance of the diode; Rs)
Vs = I*Rs;
V = Vs+Vd;

% From V, calculate Pdc, Pin, Eff
Pdc=V(1)^2/Rl;
Pdc_dBm=10*log10(Pdc/1e-3)
P_loss=V(1)*I(1)+0.5*(V(2)*I(2)+V(3)*I(3));
Pin=P_loss+Pdc;
Pin_dBm=10*log10(Pin/1e-3)
Eff=Pdc/Pin

```

## Appendix B-2

```

% This function is used for solving the following problem:
% Given Pav, Xs, Ro, solve for Pdc, Pac.
% The calculation in this file has taken into account the dc voltage
drop
% on Rs. This is to say, Vi is not pure ac, instead, it is
Vi0+Vil*sin(wt)

```

```

syms Vd Ij Cj
syms Vi0 Vil Vo x eval
format long

```

```

% Define the frequency, Pav
Freq = 1e9;
w = 2*pi*Freq;
Pav_dBm = -35;

```

```

Pav = 0.001*10^(Pav_dBm/10);
Rs = 111;
Xs = 994;
%Vo = 0.3;
Ro=15e3;

% Define the models of Ij and Cj as a function of Vd
% Based on the nonlinear model: Ij = Is*(exp(Vd/Vt)-1);
% Cj = Cjo/((1-Vd/Vbi)^r);
Vt = 0.026*1.06;
Is = 3e-6;
Cj = 0.18e-12;

% Given Ro, solve for Vi and Vo
v = [Vi0,Vi1,Vo];
%options = optimset('maxIter',1e5,'maxFunEvals',1e5,'TolFun',1e-
8,'TolX',1e-8);
[V,eval] = fsolve(@v) Solve_4_Vi_Vo(v,Ro,Pav,Rs,Xs,Cj,Vt,Is,w),[-
0.3,0.5,0.3]);
Vi0 = V(1);
Vi1 = V(2);
Vo = V(3);

% % Given Pav, Vo(or Ro), solve for optimum Xs and maximum Pdc
% % Given Ro, solve for Vi and Vo
% v = [Vi,Vo];
% V = fminsearch(@v) Solve_for_Vi_and_Vo(v,Ro,Pav,Is,Vt), [0.3,0.1]);
% Vi = V(1);
% Vo = V(2);

% Current flowing through Rj
% Fourier coefficients
a0_rj = 2*besseli(0,Vi1/Vt);
a1_rj = 1/pi*(quad(@x) Integrate_a1_rj(x,Vi1,Vt),0,2*pi));
b1_rj = 0;
% Current: DC; AC_real; AC_imag
Idc_rj = Is*(exp(-(Vo-Vi0)/Vt)*(a0_rj/2)-1);
Ilr_rj = Is*exp(-(Vo-Vi0)/Vt)*a1_rj;
Ili_rj = Is*exp(-(Vo-Vi0)/Vt)*b1_rj;

% Current flowing through Cj
% Fourier coefficients
a0_cj = 0;
a1_cj = 0;
b1_cj = -w/pi*(quad(@x) Integrate_b1_cj(x,Vi0,Vi1,Vo,Cj),0,2*pi));
% Current: DC; AC_real; AC_imag
Idc_cj = a0_cj/2;
Ilr_cj = a1_cj;
Ili_cj = b1_cj;
% Total current
Idc = Idc_rj+Idc_cj;
Ilr = Ilr_rj+Ilr_cj;
Ili = Ili_rj+Ili_cj;

```

```

I = [Idc, I1r, -I1i];
% DC power and Rectification efficiency
Pdc = Idc*Vo;
Pac = Vi1*I1r/2;
Eff = Pdc/Pac;
% input impedances
Yin = [I1r/Vi1, I1i/Vi1];
Y1r = Yin(1);
Y1i = Yin(2);
Zin = [Y1r/(Y1r^2+Y1i^2), -Y1i/(Y1r^2+Y1i^2)];
Ro = Vo/Idc;

function y = Solve_4_Vi_Vo(v,Ro,Pav,Rs,Xs,Cj,Vt,Is,w)
Vi0 = v(1);
Vi1 = v(2);
Vo = v(3);
% Fourier coefficients
a1_rj = 1/pi*(quad(@(x) Integrate_a1_rj(x,Vi1,Vt),0,2*pi));
b1_rj = 0;
% Current: AC_real; AC_imag
I1r_rj = Is*exp(-(Vo-Vi0)/Vt)*a1_rj;
I1i_rj = Is*exp(-(Vo-Vi0)/Vt)*b1_rj;
% Current flowing through Cj
% Fourier coefficients
a1_cj = 0;
b1_cj = -w/pi*(quad(@(x) Integrate_b1_cj(x,Vi0,Vi1,Vo,Cj),0,2*pi));
% Current: DC; AC_real; AC_imag
a0_rj = 2*besseli(0,Vi1/Vt);
Idc = Is*(exp(-(Vo-Vi0)/Vt)*(a0_rj/2)-1);
I1r_cj = a1_cj;
I1i_cj = b1_cj;
I1r = I1r_rj+I1r_cj;
I1i = I1i_rj+I1i_cj;
y1 = sqrt(8*Pav*Rs)-abs(Vi1+(Rs+1i*Xs)*(I1r-1i*I1i));% (Vi1+Rs*I1r+Xs*I1i)^2-(Xs*I1r-Rs*I1i)^2;
y2 = (I1r*Rs+Vi0);
y3 = Vo-Idc*Ro;
y = [y1,y2,y3];%y1^2+y2^2+y3^2;
end

function y = Integrate_a0_rj(x, Vi,Vo,Is,Vt)
y=Is*( (exp((Vi*cos(x)-Vo)/Vt))-1);
end

function y = Integrate_a1_rj(x, Vi1, Vt)
y = exp(Vi1.*cos(x)/Vt).*cos(x);
end

function y = Integrate_b1_cj(x,Vi0,Vi1,Vo,Cj)
y = Cj*(Vi1*cos(x)-(Vo-Vi0)).*cos(x);
end

```

## Appendix B-3

```
% This function is used for solving the
% Given Pav, Ro, solve for optimum Xs and maximum Pdc

clear all; close all; clc

syms Vd Ij Cj
syms Vi Vo x
format longG

% Define the frequency, Pav
Freq = 0.9e9;
w = 2*pi*Freq;
Pav_dBm = -20;

% Temp codes for debugging, assigning Vi Vo and Vd
%Vi=0.8;
%Vo=0.1;
Ro=3e3;
%Vd=Vi*cos(x)-Vo;

% Define the models of Ij and Cj as a function of Vd
% Based on the nonlinear model: Ij = Is*(exp(Vd/Vt)-1);
Vbi=0.35;
r=0.5;
Fc=0.5;
Cj = 0.18e-12;
%Cj = Cjo/((1-Vd/Vbi)^r);
Vt = 0.026*1.06;
Is = 3e-6;
%Cj = 0;
Rs=25;

Ans=zeros(1,13);
n=0;
Start_V=1;

for Pav_dBm=0:5:20

Pav = 0.001*10^(Pav_dBm/10);

% %Given Vo, solve for Vi
% Vi=fzero(@(Vi) Solve_for_Vi(Vi,Vo,Pav,Is,Vt),0.335);

% Given Pav, Vo(or Ro), solve for optimum Xs and maximum Pdc
% Given Ro, solve for Vi and Vo
v = [Vi,Vo];
V = fsolve(@(v)
Solve_for_Vi_and_Vo(v,Ro,Rs,Pav,Is,Vt,Cj,w), [Start_V*1.1,Start_V]);
%V = fsolve(@(v)
Solve_shuntdiode_vi_and_vo(v,Pav,Vt,Is,Cj,Rs,Ro,w), [2,2.2]);
Vi1 = V(1);
```

```

Vi0 = V(2);

% Current flowing through Rj
% Fourier coefficients
a0_rj = 2*besseli(0,Vi1/Vt);
%a1_rj = 1/pi*(quadl(@(x) Integrate_a1_rj(x,Vi1,Vt),0,2*pi));
b1_rj = 0;
% Current: DC; AC_real; AC_imag
Idc_rj = Is*(exp(-Vi0/Vt)*(a0_rj/2)-1);
%I1r_rj = Is*exp(-Vi0/Vt)*a1_rj;
I1r_rj = 1/pi*(quadl(@(x) test_script2_integrateI1r(x, Vi1,
Vt,Is,Vi0),0,2*pi));
I1i_rj = Is*exp(-Vi0/Vt)*b1_rj;

% Current flowing through Cj
% Fourier coefficients
a0_cj = 0;
a1_cj = 0;
b1_cj = -w/pi*(quad(@(x)
Integrate_b1_cj_4_temp6(x,Vi1,Vi0,Cj,Vbi,r),0,2*pi)); %Integrate_b1_cj(
x,0,Vi1,Vi0,Cj),0,2*pi));
%Current: DC; AC_real; AC_imag
Idc_cj = a0_cj/2;
I1r_cj = a1_cj;
I1i_cj = b1_cj;
% Total current
Idc = Idc_rj+Idc_cj;
I1r = I1r_rj+I1r_cj;
I1i = I1i_rj+I1i_cj;
I = [Idc, I1r, I1i];

% From the current, calculate the voltage across the whole diode
(consider
% the series resistance of the diode; Rs)
Vs = I*Rs+[Vi0,Vi1,0];

% DC power and Rectification efficiency
Pdc = Idc^2*Ro;
Pac = (Vs(2)*I1r+Vs(3)*I1i)/2;
Eff = Pdc/Pav
% input impedances
Yin = [I1r/Vi + 1i*I1i/Vi];
%Y1r = Yin(1);
%Y1i = Yin(2);
Zin = 1/Yin+25; %[Y1r/(Y1r^2+Y1i^2),-Y1i/(Y1r^2+Y1i^2)]
Pdc_dBm=10*log10(Pdc*1000)
%Ro = Vo/Idc;
Loss_Rb_dc=Idc^2*Rs;
Loss_Rb_I1r=0.5*I1r^2*Rs;
Loss_Rb_I1i=0.5*I1i^2*Rs;
Loss_Rb=Loss_Rb_dc+Loss_Rb_I1r+Loss_Rb_I1i;
Loss_junction=0.5*Vi1*I1r-Pdc;
Eff2=Pdc/(Pdc+Loss_Rb+Loss_junction);

n=n+1;
Ans(n)=Eff;

```

```
Start_V=Start_V+0.7;
```

```
end
```

```
function y = Integrate_b1_cj_4_temp6(x,Vi,Vo,Cjo,Vbi,r)
```

```
syms t Vj Cj  
Vj=Vi*cos(t)-Vo;  
%Cj=Cjo;  
Cj=Cjo/((1-Vj/Vbi)^r);%-0.0015e-12;  
k=diff(Cj*Vj,t)*sin(t);  
y =subs(k,t,x);  
end
```

```
function y = Integrate_b1_cj_4_temp6_2(x,Vi,Vo,Cjo,Vbi,r,Fc)
```

```
syms t Vj Cj  
Vj=Vi*cos(t)-Vo;  
%Cj=Cjo/(1-Fc)^r*(1+(r/(Vbi*(1-Fc)))*(Vj-Fc*Vbi));  
Cj=-1.051e-8*Vj^4+3.912e-9*Vj^3-3.155e-10*Vj^2+9.498e-12*Vj+1.082e-13;  
k=diff(Cj*Vj,t)*sin(t);  
y =subs(k,t,x);  
end
```

## **Bibliography**

## Bibliography

- [1] Ke Wu, Debabani Choudhury, and Hiroshi Matsumoto. "Wireless power transmission, technology, and applications." *Proceedings of the IEEE*, 6.101 (2013): 1271-1275.
- [2] Shu Yuen Ron Hui, Wenxing Zhong, and Chi Kwan Lee. "A critical review of recent progress in mid-range wireless power transfer." *IEEE Transactions on Power Electronics*, 29.9 (2014): 4500-4511.
- [3] Xuezhe Wei, Zhenshi Wang, and Haifeng Dai. "A critical review of wireless power transfer via strongly coupled magnetic resonances." *Energies*, 7.7 (2014): 4316-4341.
- [4] Daniel J. Yeager, Pauline S. Powledge, Richa Prasad, David Wetherall, and Joshua R. Smith. "Wirelessly-charged UHF tags for sensor data collection." *2008 IEEE International Conference on RFID*, IEEE, 2008.
- [5] Kiani, M., & Ghovanloo, M. (2010). An RFID-based closed-loop wireless power transmission system for biomedical applications. *IEEE Transactions on Circuits and Systems II: Express Briefs*, 57(4), 260-264.
- [6] Jiang, Hao, et al. "A high-power versatile wireless power transfer for biomedical implants." *Engineering in Medicine and Biology Society (EMBC), 2010 Annual International Conference of the IEEE*. IEEE, 2010.
- [7] Pengfei Li, and Rizwan Bashirullah. "A wireless power interface for rechargeable battery operated medical implants." *IEEE Transactions on Circuits and Systems II: Express Briefs*, 54.10 (2007): 912-916.
- [8] <http://www.witricity.com/assets/highly-resonant-power-transfer-kesler-witricity-2013.pdf>
- [9] Hamid Jabbar, Young S. Song, and Taikyeong Ted Jeong. "RF energy harvesting system and circuits for charging of mobile devices." *IEEE Transactions on Consumer Electronics*, 56.1 (2010): 247-253.
- [10] Siqi Li, and Chunting Chris Mi. "Wireless power transfer for electric vehicle applications." *IEEE Journal of Emerging and Selected Topics in Power Electronics*, 3.1 (2015): 4-17.
- [11] <http://readwrite.com/2014/02/11/wireless-charging-standards-agreement>
- [12] <http://www.forbes.com/sites/williampentland/2015/03/02/wireless-power-tech-moves-into-mainstream/#6f449d264617>

- [13] <http://www.wirelesspowerconsortium.com/>
- [14] <http://www.rezence.com/alliance/about-a4wp>
- [15] <http://www.qiwireless.com/>
- [16] <http://www.verizonwireless.com/wcms/consumer/wireless-charging.html>
- [17] <http://www.rrc-wireless-power.com/>
- [18] [http://www.nav200.delphi.com/news/pressReleases/pressReleases\\_2010/pr\\_2010\\_09\\_29\\_001/](http://www.nav200.delphi.com/news/pressReleases/pressReleases_2010/pr_2010_09_29_001/)
- [19] <http://www.technologyreview.com/news/521761/someday-your-ev-charger-may-be-the-roadway-itself/>
- [20] <http://industryarc.com/Report/7384/wireless-charging-market-report.html>
- [21] <http://www.army.mil/article/79454/>
- [22] <http://www.witricity.com/assets/highly-resonant-power-transfer-kesler-witricity-2013.pdf>
- [23] Jenn, David. "Short Range Wireless Power Transfer (WPT) for UAV/UAS Battery Charging-Phase 1". No. NPS-EC-14-004. *Naval Postgraduate School Monterey CA Dept of Electrical and Computer Engineering*, 2014.
- [24] Lu, Xiao, Ping Wang, Dusit Niyato, Dong In Kim, and Zhu Han. "Wireless networks with RF energy harvesting: A contemporary survey." *IEEE Communications Surveys & Tutorials*, 17, no. 2 (2015): 757-789.
- [25] Park G, Rosing T, Todd MD, Farrar CR, Hodgkiss W. Energy harvesting for structural health monitoring sensor networks. *Journal of Infrastructure Systems*. 2008 Mar; 14(1): 64-79.
- [26] Gungor VC, Hancke GP. Industrial wireless sensor networks: Challenges, design principles, and technical approaches. *IEEE Transactions on Industrial Electronics*, 2009 Oct; 56(10):4258-65.
- [27] Kim S, Vyas R, Bito J, Niotaki K, Collado A, Georgiadis A, Tentzeris MM. Ambient RF energy-harvesting technologies for self-sustainable standalone wireless sensor platforms. *Proceedings of the IEEE*. 2014 Nov;102(11):1649-66.
- [28] X. Wang, A. Mortazawi, "A Self-Sensing AM Frequency Electromagnetic Energy Scavenger", *2013 IEEE MTT-S International Microwave Symposium Digest (IMS)*. IEEE, 2013.
- [29] [http://www.darnell.com/market/index.php?cPath=2\\_24\\_35](http://www.darnell.com/market/index.php?cPath=2_24_35)
- [30] Das R, Yoo H. Wireless power transfer and biotelemetry in a leadless pacemaker. In *2015 International Workshop on Antenna Technology (iWAT)*, 2015 Mar 4 (pp. 350-352). IEEE.
- [31] N. Tesla, "Method of Regulating Apparatus For Producing Currents of High Frequency," *U.S. Patent 568,178*, September 1896.

- [32] N. Tesla, "Apparatus for Transmitting Electrical Energy," *U.S. Patent 1,119,732*, December 1914.
- [33] N. Tesla, "The True Wireless," *Electrical Experimenter* 7, No. 1, 23 (May 1919).
- [34] Brown WC. The history of power transmission by radio waves. *IEEE Transactions on Microwave Theory and Techniques*. 1984 Sep;32(9):1230-42.
- [35] Brown WC. Experiments involving a microwave beam to power and position a helicopter. *IEEE Transactions on Aerospace and Electronic Systems*, 1969 Sep(5):692-702.
- [36] Tomar A, Gupta S. Wireless power transmission: Applications and components. In *International Journal of Engineering Research and Technology* 2012 Nov 8 (Vol. 1, No. 5 (July-2012)). ESRSA Publications.
- [37] Xie L, Shi Y, Hou YT, Lou A. Wireless power transfer and applications to sensor networks. *IEEE Wireless Communications*, 2013 Aug;20(4):140-5.
- [38] Kurs, A., Karalis, A., Moffatt, R., Joannopoulos, J. D., Fisher, P., & Soljačić, M. (2007). Wireless power transfer via strongly coupled magnetic resonances. *Science*, 317(5834), 83-86.
- [39] <http://www.geeky-gadgets.com/intel-demonstrates-new-wireless-power-technology/>
- [40] Lee, Seung-Hwan, and Robert D. Lorenz. "Development and validation of model for 95%-efficiency 220-W wireless power transfer over a 30-cm air gap." *IEEE Transactions on Industry Applications*, 47, no. 6 (2011): 2495-2504.
- [41] <http://primove.bombardier.com/>
- [42] Cannon, Benjamin L., et al. "Magnetic resonant coupling as a potential means for wireless power transfer to multiple small receivers." *IEEE Transactions on Power Electronics*, 24.7 (2009): 1819-1825.
- [43] Ahn, Dukju, and Songcheol Hong. "A study on magnetic field repeater in wireless power transfer." *IEEE Transactions on Industrial Electronics*, 60.1 (2013): 360-371.
- [44] Hui SY, Zhong W, Lee CK. A critical review of recent progress in mid-range wireless power transfer. *IEEE Transactions on Power Electronics*. 2014 Sep;29(9):4500-11.
- [45] McSpadden JO, Mankins JC. Space solar power programs and microwave wireless power transmission technology. *Microwave Magazine, IEEE*. 2002 Dec;3(4):46-57.
- [46] Runhong Huang, Bo Zhang, Dongyuan Qiu, and Yuqiu Zhang. "Frequency Splitting Phenomena of Magnetic Resonant Coupling Wireless Power Transfer." *IEEE Transactions on Magnetics*, 50, no. 11 (2014): 1-4.
- [47] Sample AP, Meyer DA, Smith JR. Analysis, experimental results, and range adaptation of magnetically coupled resonators for wireless power transfer. *IEEE Transactions on Industrial Electronics*, 2011 Feb;58(2):544-54.

- [48] Park, Jongmin, et al. "Investigation of adaptive matching methods for near-field wireless power transfer." *IEEE Transactions on Antennas and Propagation*, 59.5 (2011): 1769-1773.
- [49] <http://www.cse.wustl.edu/~jain/cse574-14/ftp/power/#sec4>
- [50] Beh, Teck Chuan, Masaaki Kato, Takehiro Imura, Sehoon Oh, and Yoichi Hori. "Automated impedance matching system for robust wireless power transfer via magnetic resonance coupling." *Industrial Electronics, IEEE Transactions on* 60, no. 9 (2013): 3689-3698.
- [51] Cha, Hyouk-Kyu, Woo-Tae Park, and Minkyu Je. "A CMOS rectifier with a cross-coupled latched comparator for wireless power transfer in biomedical applications." *Circuits and Systems II: Express Briefs, IEEE Transactions on* 59, no. 7 (2012): 409-413.
- [52] Zhou, Xun, Rui Zhang, and Chin Keong Ho. "Wireless information and power transfer: Architecture design and rate-energy tradeoff." *Communications, IEEE Transactions on* 61, no. 11 (2013): 4754-4767.
- [53] Barton, Taylor W., Joshua Gordonson, and David J. Perreault. "Transmission line resistance compression networks for microwave rectifiers." In *Microwave Symposium (IMS), 2014 IEEE MTT-S International*, pp. 1-4. IEEE, 2014.
- [54] Barton, Taylor W., Joshua M. Gordonson, and David J. Perreault. "Transmission line resistance compression networks and applications to wireless power transfer." *Emerging and Selected Topics in Power Electronics, IEEE Journal of* 3, no. 1 (2015): 252-260.
- [55] Niotaki, Kyriaki, Anthimos Georgiadis, Ana Collado, and John S. Vardakas. "Dual-Band Resistance Compression Networks for Improved Rectifier Performance." *Microwave Theory and Techniques, IEEE Transactions on* 62, no. 12 (2014): 3512-3521.
- [56] Cha, Hyouk-Kyu. "A 13.56 MHz CMOS Multi-Stage Rectifier for Wireless Power Transfer in Biomedical Applications." *Journal of the Institute of Electronics and Information Engineers* 50, no. 3 (2013): 35-41.
- [57] Yoo TW, Chang K. Theoretical and experimental development of 10 and 35 GHz rectennas. *IEEE Transactions on Microwave Theory and Techniques*, 1992 Jun;40(6):1259-66.
- [58] Lim, Yongseok, Hoyoung Tang, Seungok Lim, and Jongsun Park. "An adaptive impedance-matching network based on a novel capacitor matrix for wireless power transfer." *Power Electronics, IEEE Transactions on* 29, no. 8 (2014): 4403-4413.
- [59] Karalis, Aristeidis, Andre B. Kurs, Robert Moffatt, John D. Joannopoulos, Peter H. Fisher, and Marin Soljacic. "Adaptive wireless power transfer apparatus and method thereof." U.S. Patent Application 13/030,395, filed February 18, 2011.
- [60] Fu, W., Zhang, B., & Qiu, D. (2009, May). Study on frequency-tracking wireless power transfer system by resonant coupling. In *IEEE 6th International Power*

- Electronics and Motion Control Conference, 2009. IPEMC'09.* (pp. 2658-2663). IEEE.
- [61] Sample, Alanson P., David A. Meyer, and Joshua R. Smith. "Analysis, experimental results, and range adaptation of magnetically coupled resonators for wireless power transfer." *IEEE Transactions on Industrial Electronics*, 58.2 (2011): 544-554.
- [62] Jang, Byung-Jun, Seongjoo Lee, and Hyungoo Yoon. "HF-band wireless power transfer system: Concept, issues, and design." *Progress in electromagnetics research* 124 (2012): 211-231.
- [63] Tan, Yen Kheng, and Sanjib Kumar Panda. "Optimized wind energy harvesting system using resistance emulator and active rectifier for wireless sensor nodes." *Power Electronics, IEEE Transactions on* 26, no. 1 (2011): 38-50.
- [64] Falkenstein, Erez, Michael Roberg, and Zoya Popović. "Low-power wireless power delivery." *Microwave Theory and Techniques, IEEE Transactions on* 60, no. 7 (2012): 2277-2286.
- [65] McSpadden, James O., Taewhan Yoo, and Kai Chang. "Theoretical and experimental investigation of a rectenna element for microwave power transmission." *Microwave Theory and Techniques, IEEE Transactions on* 40, no. 12 (1992): 2359-2366.
- [66] Qiu, Yifeng, Chris Van Liempd, Bert Op het Veld, Peter G. Blanken, and Chris Van Hoof. " $5\mu\text{W}$ -to-10mW input power range inductive boost converter for indoor photovoltaic energy harvesting with integrated maximum power point tracking algorithm." In *Solid-State Circuits Conference Digest of Technical Papers (ISSCC), 2011 IEEE International*, pp. 118-120. IEEE, 2011.
- [67] Huwig, Dominik, and Peter Wambsganß. "Digitally Controlled Rectifier for Wireless Power Receivers." [rrc-wireless-power.com](http://rrc-wireless-power.com)
- [68] Sun, H. C., Z. Zhong, and Yong Xin Guo. "Design of rectifier with extended operating input power range." *Electronics Letters* 49, no. 18 (2013): 1175-1176.
- [69] Del Prete, M., Alessandra Costanzo, Diego Masotti, and Aldo Romani. "An alternative rectenna design approach for wirelessly powered energy autonomous systems." In *Microwave Symposium Digest (IMS), 2013 IEEE MTT-S International*, pp. 1-4. IEEE, 2013.
- [70] Hagerty, J. A., Helmbrecht, F. B., McCalpin, W. H., Zane, R., & Popovic, Z. B.. Recycling ambient microwave energy with broad-band rectenna arrays. *Microwave Theory and Techniques, IEEE Transactions on*, 52(3), pp. 1014-1024. Mar. 2004.
- [71] Sample, A., & Smith, J. R. (2009, January). Experimental results with two wireless power transfer systems. In *Radio and Wireless Symposium, 2009. RWS'09. IEEE* (pp. 16-18). IEEE.
- [72] Sample, A., & Smith, J. R. (2009, January). Experimental results with two wireless power transfer systems. In *Radio and Wireless Symposium, 2009. RWS'09. IEEE* (pp. 16-18). IEEE.

- [73] Dolgov, Arseny, Regan Zane, and Zoya Popovic. "Power management system for online low power RF energy harvesting optimization." *Circuits and Systems I: Regular Papers, IEEE Transactions on* 57, no. 7 (2010): 1802-1811.
- [74] R.J.Vyas, B.Cook, Y.Kawahara and M.M.Tentzeris, "E-WEHP: A Batteryless Embedded Sensor Platform Wirelessly Powered from Ambient Digital-TV Signals", *IEEE Transactions on Microwave Theory and Techniques*, Vol.61, No.6, pp.2491-2505.
- [75] <http://www.ti.com/product/BQ25504>
- [76] <https://www.maximintegrated.com/en/products/power/battery-management/MAX17710.html>
- [77] <http://www.powercastco.com/products/powerharvester-receivers/>
- [78] <https://www.silabs.com/products/mcu/lowpower/Pages/efm32gg-stk3700.aspx>
- [79] Kim S, Vyas R, Bito J, Niotaki K, Collado A, Georgiadis A, Tentzeris MM. Ambient RF energy-harvesting technologies for self-sustainable standalone wireless sensor platforms. *Proceedings of the IEEE*. 2014 Nov;102(11):1649-66.
- [80] Priya S, Inman DJ, editors. Energy harvesting technologies. New York: Springer; 2009.
- [81] Gregg BA, Hanna MC. Comparing organic to inorganic photovoltaic cells: Theory, experiment, and simulation. *Journal of Applied Physics*. 2003 Mar 15;93(6):3605-14.
- [82] Piñuela, Manuel, Paul D. Mitcheson, and Stepan Lucyszyn. "Ambient RF energy harvesting in urban and semi-urban environments." *Microwave Theory and Techniques, IEEE Transactions on* 61, no. 7 (2013): 2715-2726.
- [83] Mazda F, editor. Telecommunications engineer's reference book. Butterworth-Heinemann; 2014 Jun 28.
- [84] Halabe, U. B., Maser, K., & Kausel, E. (1989). *Propagation characteristics of electromagnetic waves in concrete*. Massachusetts Inst of Tech Cambridge Dept of Civil Engineering.
- [85] Wang X, Mortazawi A. Medium wave energy scavenging for wireless structural health monitoring sensors. *IEEE Transactions on Microwave Theory and Techniques*, 2014 Apr; 62(4):1067-73.
- [86] Balanis CA. Antenna theory: analysis and design. John Wiley & Sons; 2016 Feb 1.
- [87] McGowan K. Semiconductors: From Book to Breadboard. Cengage Learning; 2011 Aug 17.
- [88] <http://www.eecs.berkeley.edu/Pubs/TechRpts/2011/EECS-2011-94.pdf>
- [89] Jung W, Oh S, Bang S, Lee Y, Foo Z, Kim G, Zhang Y, Sylvester D, Blaauw D. An ultra-low power fully integrated energy harvester based on self-oscillating switched-capacitor voltage doubler. *IEEE Journal of Solid-State Circuits*, 2014 Dec;49(12):2800-11.

- [90] Rashid MH. Power electronics handbook: devices, circuits and applications. Academic press; 2010 Jul 19.
- [91] Grgić, Dario, et al. "Ultra-low input voltage DC-DC converter for micro energy harvesting." (2009): 265-268.
- [92] Torah R, Glynn-Jones P, Tudor M, O'Donnell T, Roy S, Beeby S. Self-powered autonomous wireless sensor node using vibration energy harvesting. *Measurement science and technology*. 2008 Oct 24;19(12):125202.
- [93] Stoopman M, Serdijn WA, Philips K. A robust and large range optimally mismatched RF energy harvester with resonance control loop. In *Circuits and Systems (ISCAS), 2012 IEEE International Symposium on* 2012 May 20 (pp. 476-479). IEEE.
- [94] Paing, T.; Shin, J.; Zane, R.; Popovic, Z., "Resistor Emulation Approach to Low-Power RF Energy Harvesting," *Power Electronics, IEEE Transactions on*, vol.23, no.3, pp.1494-1501, May 2008.
- [95] Duffing, G. (1918). *Erzwungene Schwingungen bei veränderlicher Eigenfrequenz und ihre technische Bedeutung* (No. 41-42). R, Vieweg & Sohn.
- [96] Kovacic, I., & Brennan, M. J. (2011). *The Duffing equation: Nonlinear oscillators and their behavior*. Wiley.com.
- [97] Jordan, Dominic William, and Peter Smith. *Nonlinear Ordinary Differential Equations: Problems and Solutions*. Oxford: Oxford University Press, 2007.
- [98] Chen L, Zhu W. Stochastic jump and bifurcation of Duffing oscillator with fractional derivative damping under combined harmonic and white noise excitations. *International Journal of Non-Linear Mechanics*. 2011 Dec 31;46(10):1324-9.
- [99] Ueda, Yoshisuke. "Steady motions exhibited by Duffing's equation: a picture book of regular and chaotic motions." In *Presented at the Eng. Foundation Conf. on New Approaches to Nonlinear Problems in Dyn., Monterey, Calif., 9-14 Dec. 1979*, vol. 1, pp. 9-14. 1980.
- [100] J. W. Deng, and Z. You. "Semi-softening and hardening mechanical system for smart vibration generators." In *SPIE Smart Structures and Materials+ Nondestructive Evaluation and Health Monitoring*, pp. 79813I-79813I. International Society for Optics and Photonics, 2011.
- [101] G. Wang, and S. He. "A quantitative study on detection and estimation of weak signals by using chaotic Duffing oscillators." *IEEE Transactions on Circuits and Systems I: Fundamental Theory and Applications*, vol. 50, no. 7, pp. 945-953, Jul. 2003
- [102] Clary Jr William, T. "Nonlinear resonant circuit devices." U.S. Patent 2,838,687, June 10, 1958.
- [103] Zhou, Jin, and Tianping Chen. "Synchronization in general complex delayed dynamical networks." *IEEE Transactions on Circuits and Systems I: Regular Papers*, vol. 53, no. 3, pp. 733-744, Mar. 2006

- [104] A. Hajati, and Sang-Gook Kim. "Ultra-wide bandwidth piezoelectric energy harvesting." *Applied Physics Letters* 99(8): 083105, 2011
- [105] A. Hajati. "Ultra-wide-bandwidth micro energy harvester." PhD diss., Massachusetts Institute of Technology, 2011.
- [106] J. Heebl, "Development and Characterization of a Tunable Resonant Shielded Loop Wireless Non-Radiative Power Transfer System", Master's Thesis, University of Dayton, Dayton, OH, May 2011.
- [107] Tombak, A., Maria, J. P., Agyavives, F., Jin, Z., Stauf, G. T., Kingon, A. I., & Mortazawi, A. (2002). Tunable barium strontium titanate thin film capacitors for RF and microwave applications. *Microwave and Wireless Components Letters, IEEE*, 12(1), 3-5.
- [108] Neto, L.P.S.; Rossi, J.O.; Silva, A.R., "Characterization of dielectric properties of commercial ceramic capacitors for pulsed power applications," in *Power Electronics Conference (COBEP), 2011 Brazilian* , vol., no., pp.347-351, 11-15 Sept. 2011.
- [109] <http://www.infineon.com/cms/en/product/rf-and-wireless-control/rf-diode/rf-varactor-diode-and-tuner/channel.html?channel=ff80808112ab681d0112ab6b084b06e2>
- [110] Stauf GT, Ragaglia C, Roeder JF, Vestyck D, Maria JP, Agyavives T, Kingon A, Mortazawi A, Tombak A. Thick electrodes for high frequency high Q tunable ferroelectric thin film varactors. *Integrated Ferroelectrics*. 2001 Jan 1;39(1-4):321-30.
- [111] Chase DR, Chen LY, York RA. Modeling the capacitive nonlinearity in thin-film BST varactors. *IEEE Transactions on Microwave Theory and Techniques*, 2005 Oct;53(10):3215-20.
- [112] Ibuka, S.; Miyazawa, T.; Ishii, A.; Ishii, S., "Fast high voltage pulse generator with nonlinear transmission line for high repetitive operation," in *Pulsed Power Conference, 1995. Digest of Technical Papers., Tenth IEEE International* , vol.2, no., pp.1365-1370 vol.2, 3-6 July 1995
- [113] H. P. Jeon, Y. K. Choi, S. W. Kim, D. K. Choi, "Simulation and Characterization for the Non-Linearity of Multilayer Ceramic Capacitors with New Equivalent Circuits under Ac-Field", *Solid State Phenomena, Vols. 124-126*, pp. 827-830, Jun. 2007
- [114] <http://ksim.kemet.com/Plots/SpicePlots.aspx>
- [115] S. Cheon, et al. "Circuit-model-based analysis of a wireless energy-transfer system via coupled magnetic resonances." *IEEE Transactions on Industrial Electronics*, 58.7 (2011): 2906-2914.
- [116] T. C. Beh, et al. "Automated impedance matching system for robust wireless power transfer via magnetic resonance coupling." *IEEE Transactions on Industrial Electronics*, 60.9 (2013): 3689-3698.

- [117] Del Grosso, Andrea, Daniele Inaudi, and Livia Pardi. "Overview of european activities in the health monitoring of bridges." In *First International conference on Bridge Maintenance, Safety and Management, IABMAS*, vol. 2. 2002.
- [118] Sazonov, E., Janoyan, K., & Jha, R. (2004). Wireless intelligent sensor network for autonomous structural health monitoring. *Smart Structures/NDE 2004*.
- [119] FHWA Bridge Programs, May. 2012. [Online]. Available: <http://www.fhwa.dot.gov/bridge/britab.cfm>
- [120] Sazonov, E., Li, H., Curry, D., & Pillay, P. (2009). Self-powered sensors for monitoring of highway bridges. *Sensors Journal, IEEE*, 9(11), 1422-1429.
- [121] Wang X, Mortazawi A. Medium wave energy scavenging for wireless structural health monitoring sensors. *IEEE Transactions on Microwave Theory and Techniques*, 2014 Apr;62(4):1067-73.
- [122] Suh YH, Chang K. A high-efficiency dual-frequency rectenna for 2.45-and 5.8-GHz wireless power transmission. *IEEE Transactions on Microwave Theory and Techniques*, 2002 Jul;50(7):1784-9.
- [123] Guo J, Zhu X. An improved analytical model for RF-DC conversion efficiency in microwave rectifiers. In *Microwave Symposium Digest (MTT), 2012 IEEE MTT-S International 2012 Jun 17* (pp. 1-3). IEEE.
- [124] Curty JP, Joehl N, Krummenacher F, Dehollain C, Declercq MJ. A model for  $\mu$ -power rectifier analysis and design. *IEEE Transactions on Circuits and Systems I: Regular Papers*, 2005 Dec;52(12):2771-9.
- [125] Cardoso, Adilson J., Lucas G. De Carli, Carlos Galup-Montoro, and Márcio C. Schneider. "Analysis of the rectifier circuit valid down to its low-voltage limit." *Circuits and Systems I: Regular Papers, IEEE Transactions on* 59, no. 1 (2012): 106-112.
- [126] Harrison RG, Le Polozec X. Nonsquarelaw behavior of diode detectors analyzed by the Ritz-Galerkin method. *Microwave Theory and Techniques, IEEE Transactions on*. 1994 May;42(5):840-6.
- [127] Jong, T., P. Patil, C. Yi Hu, Mamad Rajabi, Saeed Farsi, and Dominique Schreurs. "Design of Efficient Rectifier for Low-Power Wireless Energy Harvesting at 2.45 GHz." In *Radio Wireless Symposium (RWS)*, pp. 1-3. 2015.
- [128] Korenev BG. Bessel functions and their applications. CRC Press; 2003 Sep 2.
- [129] Wyatt JL. Nonlinear dynamic maximum power theorem, with numerical method. Massachusetts Inst of Tech Cambridge Dept of Electrical Engineering and Computer Science, 1983 Sep.
- [130] Cripps SC. *RF Power Amplifiers for Wireless Communications*, (Artech House Microwave Library). Artech House. 2006
- [131] Scorcioni S, Bertacchini A, Larcher L, Ricciardi A, Dondi D, Pavan P. RF to DC CMOS rectifier with high efficiency over a wide input power range for RFID

applications. In Microwave Symposium Digest (MTT), 2012 IEEE MTT-S International 2012 Jun 17 (pp. 1-3). IEEE.

- [132] Yoshida S, Fukuda G, Noji T, Tashiro S, Kobayashi Y, Kawasaki S. Wide power range operable 3-stage S-band microwave rectifier with automatic selector based on input power level. In Microwave Symposium Digest (IMS), 2013 IEEE MTT-S International 2013 Jun 2 (pp. 1-4). IEEE.